Title: Meteor over New York City: Brines in a primitive CM asteroid

Authors: Peter Jenniskens[1,2,*], Michael E. Zolensky[3], Austin Gordon[4], Jamie Gordon[4], Mike Hankey[5], Elizabeth A. Silber[6], Miro Ronac Giannone[6], Jangmi Han[7], Le Loan[7], Marc D. Fries[3], Karen Ziegler[8], Queenie H. S. Chan[9], Diptimayee Behera[9], Jonathan S. Watson[10], Mark A. Sephton[10], James Brakeley[9], Bianka Munday[9], Yoko Kebukawa[11], Zack Gainsforth[12], Masanori Suzuki[13], Gregory A. Brennecka[14], Jan H. Render[14], Henner Busemann[15], Daniela Krietsch[15], Colin Maden[15], Kees C. Welten[16], Kunihiko Nishiizumi[16], Marc W. Caffee[17], Takahiro Hiroi[18], Stefan Ruchti[19,20], Philippe Schmitt-Kopplin[19,20,21], Jasmine Hertzog[22], Vincent Carré[22], Daniel P. Glavin[23], Jason P. Dworkin[23], Hannah L. McLain[23,24], Angel Mojarro[25], José Aponte[23], Denise Buckner[23], Nanako O. Ogawa[26], Yoshinori Takano[26], Naohiko Ohkouchi[26], Sonia M. Tikoo[27], Ji-In Jung[27], Eva M. Riveros[28], Jon M. Friedrich[28,29], and Denton S. Ebel[29]

Affiliations:

[1]SETI Institute; Mountain View, CA 94043, USA.
[2]NASA Ames Research Center; Moffett Field, CA 94035, USA.
[3]ARES, NASA Johnson Space Center; Houston, TX 77058, USA.
[4]Hillsborough, NJ , USA.
[5]American Meteor Society and AllSky7 Network; Monkton, MD 21111, USA.
[6]Sandia National Laboratories; Albuquerque, NM 87123, USA.
[7]Amentum, NASA Johnson Space Center, Houston, TX 77058, USA.
[8]University of New Mexico; Albuquerque, NM, USA.
[9]Centre for Dynamic Earth and the Solar System (CeDESS), Department of Earth Sciences, Royal Holloway University of London; Surrey TW20 0EX, UK.
[10]Department of Earth Science and Engineering, Imperial College London; London SW7 2BX, UK.
[11]Earth and Planetary Sciences, Institute of Science Tokyo; Tokyo 152-8551, Japan.
[12]University of California at Berkeley, Space Sciences Laboratory; Berkeley, CA 94720, USA.
[13]Department of Chemistry and Life Science, Yokohama National University; Yokohama 240-8501, Japan.
[14]Lawrence Livermore National Laboratory; Livermore, CA 94550, USA.
[15]Institute of Geochemistry and Petrology, ETH Zürich; 8092 Zürich, Switzerland.
[16]Space Sciences Laboratory, University of California; Berkeley, CA 94720, USA.
[17]Department of Physics and Astronomy, Purdue University; West Lafayette, IN 47907, USA.
[18]Department of Earth, Environmental and Planetary Sciences, Brown University; Providence, RI 02912, USA.

[19]Research Unit Analytical BioGeoChemistry, Helmholtz Munich; 85764 Neuherberg, Germany.
[20]Analytical Food Chemistry, Technical University of Munich; 85354 Freising, Germany.
[21]Center for Astrochemical Studies, Max Planck Institute for Extraterrestrial Physics; 85748 Garching, Germany.
[22]Laboratoire LCP-A2MC, Institut de Chimie Physique et Matériaux (ICPM); 57070 Metz, France.
[23]Solar System Exploration Division, NASA Goddard Space Flight Center; Greenbelt, MD 20771, USA.
[24]Center for Research and Exploration in Space Science and Technology (CRESST) and Department of Physics, The Catholic University of America; Washington, D.C. 20064, USA.
[25]Oak Ridge Associated Universities; Oak Ridge, TN 37830, USA.
[26]Biogeochemistry Research Center (BGC), Japan Agency for Marine-Earth Science and Technology (JAMSTEC); Yokosuka, Kanagawa, 237-0061 Japan.
[27]Department of Geophysics, Stanford University; Palo Alto, CA 94305, USA.
[28]Department of Chemistry and Biochemistry, Fordham University; New York, NY 10458, USA.
[29]Department of Earth and Planetary Sciences, American Museum for Natural History; New York, NY 10024, USA.

*Corresponding author. Email: pjenniskens@seti.org

Abstract: The CI (Ivuna-type) carbonaceous chondrites returned from asteroids Ryugu and Bennu contain mobilized sodium from the evaporation or freezing of liquid water into brines (*1–2*), shedding light on the internal structure of ice-rich CI-type worlds and the formation of prebiotic organic compounds. The formation of brines has not been demonstrated in CM (Mighei-type) carbonaceous chondrites, which also supplied organic matter to the early Earth (*3*). Here, we announce the fall of a primitive meteorite from a daytime fireball over the New York metropolitan area in July 2024. It is a CM2 breccia that contains unique CM1 clasts rich in water and sodium. The meteorite contains abundant amino acids and other products of organic chemistry in brines that reveal subsurface processes on CM-type worlds

Main Text: The large primitive asteroid Ceres has craters with bright white areas that are dominated by sodium carbonates, thought to be evaporation deposits from sublimated briny fluids originating from an icy subsurface layer (*4–7*). Did other, smaller, primitive asteroid parent bodies have similar icy subsurface layers? These brines can enable organic chemistry for the origin of life by allowing phosphate to remain in solution and catalyze chemical reactions between organics and precipitate minerals (*2*).

An evaporite sequence from late-stage brine flowing through primitive asteroids has now been detected in CI-type Ryugu and Bennu samples (*2, 8*). Similar processes are expected to occur in other carbonaceous chondrite types, but terrestrial weathering would obscure evidence of salt precipitation (*1*).

So far, CM-type carbonaceous chondrites are not known to contain indigenous evaporites. They are the most common water-rich primitive meteorites to be recovered on Earth. They also experienced past aqueous alteration that created abundant phyllosilicates (*9*) but to a lesser degree than CI chondrites. Evaporates are most likely in petrographic type CM1 carbonaceous chondrites, which are more heavily aqueously altered than type CM2, but all CM1 meteorites known to date are finds, prone to terrestrial weathering (*9–10*).

Impact and recovery of Hillsborough

On July 16, 2024, at 15:17:27.6 UTC, a daytime fireball with sonic boom was reported to the American Meteor Society by 60 visual observers in the states of New York, New Jersey, Connecticut, Rhode Island and Pennsylvania, confirming media reports of a meteor over the New York metropolitan area. The meteor was filmed by two stations of the Allsky7 camera network (Fig. 1A), operated by M. Kirschner in Northford, CT, and by P. Deterline in Douglassville, PA, as well as by the doorbell camera of J. Stier in Wayne, NJ. Triangulation of those records show that the meteor moved in a 256º direction (East to West) over Staten Island towards New Jersey, from 44.4 to 34.9 km altitude at an angle of 29º to the horizontal (Table Supplementary Materials and Methods S-1). Each flare left a wake of dust. A surviving mass caused a final flare at 28.2 km. From 2 to 16 minutes later, the Newark Airport Doppler weather radar detected falling meteorites of 10 to 0.1 g, respectively (Fig. S-27, S-28), but none of these were found.

The sonic boom was not detected by conventional infrasound arrays, but recorded by doorbell video at locations near the trajectory. Two sharp overpressure maxima were identified as the leading and trailing shock signatures of the N-wave (*11*) with a peak-to-peak spacing less than the full period of the pulse. The dominant acoustic period was 0.5 ± 0.1 s. Using the recently refined empirical bolide energy relation (*12*), the kinetic energy deposited by the fireball was 1.31 ± 0.09 tons TNT equivalent. With the triangulation-derived initial speed of 14.4 ± 0.6 km/s (Table S-1), this implies a pre-atmospheric mass of 53 ± 6 kg.

Shortly thereafter, a large meteorite hit the roof of a house in Hillsborough, NJ (Figs. 1B–C). The owner of the home heard a loud crash at approximately 15:20 UTC and found a hole in the ceiling of the master bedroom accompanied by black matter that covered the bed, carpet, and surrounding areas. The meteorite had broken into many fragments (Fig. 1D), including dust, and a strong sulfur-like odor was present in the air. Immediate care was taken to preserve and document the entire scene using disposable gloves and aluminum foil, with fragments placed in glass jars. The total recovered mass was ~1.35 kg.

Petrography and evidence for brine mobility

Hillsborough is the 22nd observed CM-type meteorite fall, but only the 2nd fall classified as CM1/2, following the fall of Kolang in Indonesia in 2020 (*10*). The stones were extremely friable, and no fluids could be used for cutting or polishing. Scanning Electron Microscopy analysis shows that the meteorite is unusually finely brecciated for a CM (Fig. 2). Some stones consist entirely of finely-comminuted, sub-mm sized fragments (Fig. S-1). Most of these clasts (95–98%) are of CM2 type, the largest continuous clast 5 mm in size.

A notable feature in Figure 2A is the presence of a few small (<0.5 mm), matrix-dominated clasts of C1 material. Figure 2B shows how these clasts stand out in the Na element map, as their bulk matrix contains up to 2 wt% Na_2O, which is significantly enriched over the normal 0.09–0.36 wt% in CM chondrites (*13*).

Scattered within the fine-grained matrix are crystals of dolomite and magnetite (plaquettes and framboids). Even the C1 clast dolomites (labeled "D" in Fig. 3B) have high Na, which is unusual. Transmission Electron Microscopy analysis of a Focused Ion Beam (FIB) section from one of the dolomites found that Na was concentrated within cracks (Figs. 3C–D), as an unidentified amorphous phase inconsistent with contamination from handling or weathering since the recovery.

The bulk of the carbonates in the meteorite is calcite, determined by Raman and Electron Probe Microanalysis (EPMA). Fine-grained pyrrhotite ($Fe_{1-x}S$) is abundant. For the most part matrix serpentine is fully hydrated (based on low EPMA totals). Hillsborough CM2 serpentine compositions span the entire range observed for CM2 chondrites, while C1 serpentine compositions plot outside this range (Fig. S-3).

Further establishing the CM2 chondrite classification, chondrules and chondrule pseudomorphs are abundant. Chondrules range up to 1 mm in diameter, but most are less than 100 μm. Porphyritic types predominate. Most are fragmented and exhibit thick fine-grained rims, frequently multilayered. The chondrules and silicate fragments show a range of alteration to hydrous phases and many completely lack anhydrous silicates. There is excellent pseudomorphism of serpentine, tochilinite and calcite after primary ferromagnesian minerals. Fine-grained clasts are abundant, and appear to be chondrule rim fragments.

X-ray computed tomography (CT) of an 0.9946 g fragment (Fig. S-3) resulted in a density of 1.89 ± 0.01 g/cm^3, at the lower end for CM chondrites (*14*). This density would suggest a pre-atmospheric meteoroid diameter of ~38 cm. Using the above bulk density and an average CM chondrite grain density (*14*) yields a porosity of 35%, which is high for a CM chondrite. This fragment contained ~7% apparently unbrecciated clasts, primarily sub-equant in shape (Figs. S-4,5).

Geochemistry and bulk properties

A number of analyses were performed on bulk material to confirm the CM identification and understand the bulk CM2 host material. The oxygen isotopes of six fragments were analyzed by laser fluorination ICP. Sample weights were between 3.8 and 7.4 mg. The results (Fig. S-12) all lie within the CM carbonaceous chondrite field (*15*). The average values are $\delta^{18}O = 11.27 \pm 1.60$ ‰, $\delta^{17}O = 2.97 \pm 0.98$ ‰, and $\Delta^{17}O = -2.98 \pm 0.19$ ‰ (linearized with Terrestrial Fractionation Line slope = 0.528, with

2σ errors). Titanium isotopic compositions (11.3 mg piece) yielded $\varepsilon^{46}Ti = 0.59 \pm 0.04$, $\varepsilon^{48}Ti = -0.02 \pm 0.04$, and $\varepsilon^{50}Ti = 3.33 \pm 0.08$ (normalized to $^{49}Ti/^{47}Ti = 0.749766$, where ε represents parts per 10,000 deviation from a terrestrial standard, with 2σ errors), plotting among other CM chondrites (Figs. S-15, *16*).

The optical, near-IR, and mid-IR reflectance spectra were measured in the range 0.3 to 40 micron (Figs. S-6, S-10) and show the typical bands of CM2 chondrites (*17*). There is a strong OH band at 2.7–3.5 micron with a sharp low-wavelength band edge and a weak 0.7 micron band from charge transfer by iron in phyllosilicates. Unusual are the weak 0.43 and 1.9 micron bands, which may be due to iron hydroxides and hydroxyl.

The low ^{10}Be and ^{26}Al contents of ~2.6 and ~8.5 dpm/kg in Hillsborough measured by Accelerator Mass Spectrometry (Table S-5) suggest a cosmic ray exposure (CRE) age of ~0.2 Ma, overlapping with one of the main CM-chondrite peaks (*18,19*).

Hillsborough is a regolith breccia that likely experienced a comparatively long exposure to solar wind (SW) at its parent body's surface: The concentrations of trapped ^{4}He and, particularly, ^{20}Ne (Table S-6) are among the highest observed in CM chondrites (*19, and references therein*). The $^{3}He/^{4}He$ and $^{20}Ne/^{22}Ne$ ratios (Table S-6a) almost reach the ratios measured in pure SW returned by the Genesis mission (*20*).

The nominal ^{21}Ne-derived CRE age is 2.2–5.7 Ma, longer than the CRE age derived from ^{10}Be and ^{26}Al. Hillsborough's exposure as a 53 kg object in the past ~0.2 Ma ago was preceded by exposure within the regolith of a larger object. The regolith residence time, where Hillsborough was exposed to galactic cosmic rays (active within the first few m) and perhaps solar cosmic rays (active within the upper few cm of a rock) cannot be determined without additional information regarding its shielding.

A meteorite fragment protected from magnets showed a low natural remanent magnetization of 1.27×10^{-5} Am^2/kg (Fig. S-9). Hillsborough may have experienced aqueous alteration and formation of secondary magnetic minerals, such as magnetite and pyrrhotite, in a weak paleofield with an intensity <~400 nT, or it experienced a loss of primary magnetic mineral orientations during brecciation (*21*).

Organic matter and prebiotic compounds

Bulk Hillsborough contains organic matter with a total carbon weight percentage of 1.76 ± 0.05 wt%, nitrogen 0.074 ± 0.003 wt%, and sulfur 6.13 ± 0.22 wt%, respectively (Table S-3B). The carbon and nitrogen contents are only slightly lower than the typical CM values of 2.2 wt% and 0.10 wt%, respectively (*19*), and sulfur is in line with other CM (Fig. S-14). The isotopic signatures are $\delta^{13}C$ (‰ vs VPDB) = -0.2 ± 0.4, $\delta^{15}N$ (‰ vs Air) = +28.5 ±1.1, and $\delta^{34}S$ (‰ vs VCDT) = -1.0 ±0.6, respectively. Those values, too, fall among other fresh CM chondrites (*22*).

The FTIR analyzed transmission spectra on individual grains (Fig. S-6) look like those of typical CM carbonaceous chondrites. The aliphatic C-H bands at 2960 and 2930 cm^{-1} are weak. The aromatic versus aliphatic nature of the macromolecular

organic material, some found in nanoglobules (Fig. S-8), is revealed by carbon X-ray Absorption Near-Edge Structure (C-XANES) and N-XANES (Fig. S-7). The results fall in line with other CMs (*23*).

Laser desorption ionization FT-ICR mass spectrometry (*24*) of fresh surface (Fig. 4A-C) presented oxygenated compounds (CHO, CHNO, CHOS) that were more abundant than non-oxygenated heterocyclic aromatic compounds (HACs) comprised of nitrogen containing CHN or sulfur containing CHS as well as alkylated polyaromatic hydrocarbons (PAHs; CH). The ratio of these oxygenated to non-oxygenated HACs and PAHs is reduced significantly from 5.8 to 2.4 and 1.4 for Murchison, Hillsborough, and Kolang, respectively (Fig. S-17B).

PAHs and HACs in carbonaceous chondrites may either derive from the interstellar medium and/or result from secondary parent body processes, reflecting conditions of aqueous alteration (25). Our data support the second hypothesis (*26*) and suggest the formation of reduced carbon as PAHs and HACs through molecular deoxygenation in a coevolution of mineral oxidation in brines (Fig. 4D). In addition, the data show a decrease in the number of compounds containing multiple nitrogen (Fig. 4E). These profiles reflect a higher water alteration of Kolang relative to Hillsborough, with the least pronounced alteration in Murchison.

The analysis of methanol soluble extracts in electrospray ionization (ESI) negative mode FT-ICR mass spectrometry shows the same trend of deoxygenation during aqueous alteration with a subsequent loss in oxidized aromatic compounds (Fig. S-16). The latter decrease in abundance from Murchison to Kolang and finally Hillsborough (Fig. S-18).

Hillsborough shows a lower water alteration than Kolang, which is consistent with its higher abundance and intensity of organomagnesium molecules (Fig. S-17A). These are markers of high-temperature processes as well as local proximity to magnesium silicates such as pyroxenes or olivines and can rapidly hydrolyze in water environments (27). In carbonaceous chondrites, their abundance may be determined, instead, by how much of these compounds remain after aqueous alteration.

Analysis of hot water extracts of the Hillsborough meteorite (samples H02 and H03) using LC- and GC-MS revealed a complex mixture of C2 up to C11 unfunctionalized aliphatic primary-amine amino acids ($H_2N(CH_2)_nCOOH$), with an overall distribution similar to that observed in Murchison analyzed in parallel (Fig. S-23) but unlike the much lower abundance of C>5 observed in highly aqueously altered CI and CM1 meteorites (*28*). The C6 and higher amino acids are not well separated because of numerous overlapping isomers. The total abundance of identified C2 to C5 amino acids spans a wide range (~44–625 nmol/g), in contrast to Murchison (~121–167 nmol/g, Tables S-8, S-14), reflecting a larger range of alteration among clasts in the Hillsborough breccia.

The terrestrially rare non-protein amino acids including α-aminoisobutyric acid (AIB) and racemic isovaline (D/L ~ 1, Tables S-8–S-10, S-14, S-15) in the Hillsborough meteorite water extract are likely extraterrestrial in origin. The higher relative abundance of glycine and other alpha-amino acids compared to beta-, gamma-, and delta-amino acid isomers suggests a formation by HCN polymerization

and/or Strecker-cyanohydrin synthesis (*29*) inside Hillsborough's parent body during an early aqueous alteration phase at moderate temperatures. The dominance of α-amino acids is in contrast to their comparatively low abundance in highly aqueously altered CI1 and CM1 meteorites (*30*).

The Hillsborough meteorite did not escape some contamination from the fall and subsequent handling, resulting in high ε-amino-*n*-caproic acid abundances from contamination with Nylon-6 (commonly found in carpet and building materials) and biologically common protein amino acids with an L-enantiomeric excess (D/L ~0.05–0.32, Tables S-9, S-15). Accounting for these terrestrial contaminants, the total abundance of likely extraterrestrial amino acids in fragments H02 and H03 was 0.56 and 3.75 times that of the CM2 Murchison, respectively. This large difference may reflect different levels of amino acid decomposition by aqueous alteration in distinct lithologies.

Carboxylic acids in Hillsborough H03 are predominantly ^{13}C enhanced and thus likely extraterrestrial in origin (Table S-12). Acetic acid is ^{13}C depleted in both Hillsborough and Murchison, which could point to terrestrial contamination. Oxalic acid in Hillsborough is less abundant and has lower ^{13}C compared to Murchison, potentially reflecting differences in isotopic carbon reservoirs (29).

Pyrolysis GCMS analysis of Hillsborough also reveals a rich and complex mixture of hydrocarbons (Figs. S-22–25). Aside from siloxanes (Fig. S-22) that are likely contaminants due to the meteorite falling through a fiberglass isolated roof, the distribution of thiophenes and polycyclic aromatic hydrocarbons (PAHs) released from Hillsborough is similar to that of Murchison (*30*).

The complex distribution of amino acids observed in Hillsborough, similar to Murchison and other moderately altered CM2 chondrites, demonstrates that these prebiotic organic molecules were formed inside the Hillsborough parent body, likely assisted by brine fluid chemistry. The exogenous delivery of amino acids, carboxylic acids, and other soluble organic molecules by CM-type bodies and their fragments could have been an important source of the prebiotic organic inventory that led to the emergence of life on Earth.

CM parent body and origin of CM chondrites

We have previously observed Na-enrichments associated with dolomite in a xenolithic C1 clast in the Zag ordinary chondrite (*31*), a material associated with halite and sylvite that formed on a separate parent body (*32*). However, in the case of Hillsborough it appears likely that its C1 clast is indigenous to the CM parent body, and should be classified as CM1. This is a logical proposal as exogenous C1 material is rare or absent from other CM chondrites, whereas CM1 material is frequently present (*33*).

Since the Na is most concentrated in fractures in dolomite in the Hillsborough CM1 lithology, we speculate that the enrichment is due to the passage of Na-rich, late stage brines though the CM parent body. This is evidence of significant water mobility in CM chondrites otherwise having fairly homogeneous elemental compositions (*9*).

Previously, veins of phases in CM chondrites pointed to flowing water at the cm scale at least, while rims showed that S, Ca and organics were transported from adjacent matrix (*34*). In the case of the Zag C1 clast (*31*), oxygen isotope geothermometry yielded a co-crystallization temperature of less than -15 ºC, assuming equilibrium between magnetite grains intergrown within and around a dolomite, and hence the late-stage fluid was an icy brine (*35*). Rather than elevated temperature (>120ºC) or a higher water/rock ratio (*9)*, a prolonged exposure to liquid water following impacts may be responsible for the higher aqueous alteration of the CM1 clasts, as in other CM1s (*33*). If so, Hillsborough preserved clasts from the subsurface of its parent body.

After formation, that parent body built up a layer of regolith at the surface, then experienced an exceptionally large collision event that created a family of asteroids. About 0.2 Myr ago, one of those asteroids had already evolved from the asteroid belt into a Near-Earth Asteroid (NEA) orbit before it lost a ~53-kg meteoroid (*36*). We identified as many as 27 known NEA with orbits similar to Hillsborough, but with no spectral information.

Asteroid families composed of CM-type materials with the characteristic 0.7-micron band are found both in the inner and outer parts of the asteroid belt (*36*). Hillsborough's approach orbit had an inclination of $i = 4.2 \pm 2.1^{o}$ and semi-major axis $a = 2.13 \pm 0.33$ AU (Table S-1), suggesting that the parent NEA had dynamically evolved via the $\boldsymbol{\nu}_6$ resonance on the near side of the belt ($a \sim 2.1$ AU). It is possible that this NEA originated from the Erigone family in the inner main belt ($i = 4.7^{o}$), a collisional family from ~73km-sized asteroid 163 Erigone, some of which have the 0.7-micron band (*37*). This family includes NASA's Lucy mission target asteroid 52246 Donaldjohanson (*37*).

However, the observations do not exclude that the Hillsborough NEA arrived via the 3:1 resonance ($a = 2.50$ AU). All four documented CM2 falls arrived along this route from a low inclined ($i < 3^{o}$) source in the outer main belt (*36*). That source remains unidentified. If so, Hillsborough confirms that the proposed Veritas asteroid family (*38*) is too inclined to be the source ($i = 9.1^{o}$). A locally higher level of aqueous alteration in the subsurface of CM worlds would make it more likely that a collisional family associated with ~200 km asteroid 24 Themis is the source (*36*). This family is located at a low $i = 1.1^{o}$ in the outer asteroid belt. In particular the Beagle cluster in the Themis family, debris from a <10 Ma old collision, is a candidate source region. Only a fraction of the Themis family asteroids have the 0.7-micron band (*39–40*). Some family members have hydroxyl-bearing minerals (*41*), some show cometary activity (*40*), and Themis itself has water ice at the surface (*42*). Via the 2:1 resonance, Themis family asteroids can evolve into the population of Jupiter family comets (*43*), a source of CM-type micrometeorites (*44*).

References and Notes

1. T. Matsumoto, T. Noguchi, A. Miyzek, Y. Igami, M. Matsumoto, T. Yada, M. Uesugi, M. Yasutake, K. Uesugi, A. Takeuchi, H. Yuzawa, T. Ohigashi, T. Araki, Sodium carbonates on Ryugu as evidence of highly saline water in the outer Solar System. *Nature Astronomy* **8**, 1536–1543 (2024). Doi: 10.1038/s41550-024-02418-1

2. T. J. McCoy, S. S. Russell, T.J. Zega, K. L. Thomas-Keprta, S. A. Singerling, F. E. Brenker, N. E. Timms, W. D. A. Rickard, J. J. Barnes, G. Libourel, S. Ray, C. M. Corrigan, P. Haenecour, Z. Gainsforth, G. Dominguez, A. J. King, L. P. Keller, M. S. Thompson, S. A. Sandford, R. H. Jones, An evaporite sequence from ancient brine recorded in Bennu samples. *Nature* **637**, 1072–1077 (2025). Doi: 10.1038/s41586-024-08495-6

3. C.M.O'D. Alexander, R. Bowden, M. Fogel, K. Howard, C. Herd, L. Nittler, The provenances of asteroids, and their contributions to the volatile inventories of the terrestrial planets. *Science* **337**, 721–723 (2012). Doi: 10.1126/science.1223474

4. S. De Angelis, C. Carli, F. Tosi, P. Beck, O. Brissaud, B. Schmitt, S. Potin, M. C. De Sanctis, F. Capaccioni, G. Piccioni, NIR reflectance spectroscopy of hydrated and anhydrous sodium carbonates at different temperatures. *Icarus* **317**, 388–411 (2019). Doi: 10.1016/j.icarus.2018.08.012

5. N. Stein, B. L. Ehlmann, D. J. Stevenson, J. Castillo-Rogez, C. A. Raymond, Bright Na-carbonate exposures reveal recent, widespread mobilization of material in Ceres' shallow subsurface. *J. Geophysical Research* **128**, id.e2023JE007868 (2023). Doi: 10.1029/2023JE007868

6. M. J. Poston, S. R. Baker, J. E. C. Scully, E. M. Carey, L. E. Mc Keown, J. C. Castillo-Rogez, C. A. Raymond, Experimental examination of brine and water lifetimes after impact on airless worlds. *The Planetary Science Journal* **5**, id.233, 40 pp (2024). Doi: 10.3847/PSJ/ad696a

7. I. F. Pamerleau, M. M. Sori, J. E. C. Scully, An ancient and impure frozen ocean on Ceres implied by its ice-rich crust. *Nature Astronomy* **8**, 1373–1379 (2024). Doi: 10.1038/s41550-024-02350-4

8. R. C. Greenwood, I. A. Franchi, R. Findlay, J. A. Malley, M. Ito, A. Yamaguchi, M. Kimura, N. Tomioka, M. Uesugi, N. Imae, N. Shirai, T. Ohigashi, M. C. Liu, K. A. McCain, N. Matsuda, K. D. McKeegan, K. Uesugi, A. Nakato, K. Yogata, H. Yuzawa, Y. Kodama, A. Tsuchiyama, M. Yasutake, K. Hirahara, A. Tekeuchi, S. Sekimoto, I. Sakurai, I. Okada, Y. Karouji, S. Nakazawa, T. Okada, T. Saiki, S. Tanaka, F. Terui, M. Yoshikawa, A. Miyazaki, M. Nishimura, T. Yada, M. Abe, T. Usui, S. Watanabe, Y. Tsuda, Oxygen isotope evidence from Ryugu samples for early water delivery to Earth by CI chondrites. *Nature Astronomy* **7**, 29–38 (2023). Doi: 10.1038/s41550-022-01824-7

9. A. J. King, P. F. Schofield, S. S. Russell, Type 1 aqueous alteration in CM carbonaceous chondrites: Implications for the evolution of water-rich asteroids. *Meteoritics and Planetary Science* **52**, 1197–1215 (2017). Doi: 10.1111/maps.12872

10. Meteoritical Bulletin. Website: https://www.lpi.usra.edu/meteor/ (last accessed June 9, 2025).

11. E. A. Silber, D. C. Bowman, C. G. Carr, D. P. Eisenberg, et al. (82 authors), Geophysical observations of the 2023 September 24 OSIRIS-REx sample return capsule reentry. *The Planetary Science Journal* **5**, id.213, 47pp (2024). Doi: 10.3847/PSJ/ad5b5e

12. E. A. Silber, J. Trigo-Rodriguez, I. Oseghae, E. Peña Asensio, M. B. Boslough, R. Whitaker, C. Pilger, P. Lubin, V. Sawal, C. Hetzer, R. Longenbaugh, P. Jenniskens, B. Bailey, E. Mas Sanz, P. Hupe, A. N. Cohen, T. R. Edwards, S. Egan, R. E. Silber, S. Czarnowski, M. Ronac Giannone, M., Multi-parameter constraints on empirical infrasound period–yield relations for bolides and implications for planetary defense. *The Astronomical Journal*, in press (2025). Doi:10.48550/arXiv.2505.03040

13. N. Braukmüller, F. Wombacher, D. C. Hezel, R. Escoube, C. Münker, The chemical composition of carbonaceous chondrites: Implications for volatile element depletion, complementarity and alteration. *Geochimica et Cosmochimica Acta* **239,** 17–48 (2018). Doi: 10.1016/j.gca.2018.07.023

14. R. J. Macke, G. J. Consolmagno, Density, porosity, and magnetic susceptibility of carbonaceous chondrites. *Meteoritics & Planetary Science* **46**, 1842–1862 (2011). Doi: 10.1111/j.1945-5100.2011.01298.x

15. M. D. Suttle, A. J. King, P. F. Schofield, H. Bates, S. S. Russell, The aqueous alteration of CM chondrites, a review. *Geochimica et Cosmochimica Acta* **299,** 219–256 (2021). Doi: 10.1016/j.gca.2021.01.014

16. M. Rüfenacht, P. Morino, Y.-J. Lai, M. A. Fehr, M. K. Haba, M. Schönbächler, Genetic relationships of solar system bodies based on their nucleosynthetic Ti isotope compositions and sub-structures of the solar protoplanetary disk. *Geochimica et Cosmochimica Acta* **355**, 110–125 (2023). Doi: 10.1016/j.gca.2023.06.005

17. T. Hiroi, H. Kaiden, N. Imae, K. Misawa, H. Kojima, S. Sasaki, M. Matsuoka, T. Nakamura, D. L. Bish, K. Ohtsuka, K. T. Howard, K. R. Robertson, R. E. Milliken, UV-visible-infrared spectral survey of Antarctic carbonaceous chondrite chips. *Polar Science* **29,** 100723 (2021). Doi: 10.1016/j.polar.2021.100723

18. M. E. Zolensky, A. Takenouchi, T. Mikouchi, T. Gregory, K. Nishiizumi, M. W. Caffee, M. A. Velbel, D. K. Ross, A. Zolensky, L. Le, N. Imae, A. Yamaguchi A., The nature of the CM parent asteroid regolith based on cosmic ray exposure ages. *Meteoritics & Planetary Science* **56**, 49–55 (2021). Doi: 10.1111/maps.13561

19. D. Krietsch, H. Busemann, M. E. I. Riebe, A. J. King, C. M. O'D. Alexander, C. Maden, Noble gases in CM carbonaceous chondrites: Effect of parent body aqueous and thermal alteration and cosmic ray exposure ages.

Geochimica et Cosmochimica Acta **310**, 240–280 (2021). Doi: 10.1016/j.gca.2021.05.050

20. V. S. Heber, R. Wieler, H. Baur, C. Olinger, T. A. Friedmann, D. S. Burnett, Noble gas composition of the solar wind as collected by the Genesis mission. *Geochimica & Cosmochimica Acta* **73**, 7414–7432 (2009). Doi: 10.1016/j.gca.2009.09.013

21. B. P. Weiss, X.-N. Bai, R. R. F, History of the solar nebula from meteorite paleomagnetism. *Science Advances* **7**, aba5967 (2021). Doi: 10.1126/sciadv.aba596

22. V. K. Pearson, M. A. Sephton, I. A. Franchi, J. M. Gibson, I. Gilmour, Carbon and nitrogen in carbonaceous chondrites: Elemental abundances and stable isotopic compositions. *Meteoritics & Planetary Science* **41,** 1899–1918 (2006). Doi: 10.1111/j.1945-5100.2006.tb00459.x

23. Y. Kebukawa, K. Okudaira, H. Yabuta, S. Hasegawa, M. Tabata, Y. Furukawa, M. Ito, A. Nakato, A. L. D. Kilcoyne, K. Kobayashi, S.-I. Yokobori, E. Imai, Y. Kawaguchi, H. Yano, A. Yamagishi, STXM-XANES analyses of Murchison meteorite samples captured by aerogel after hypervelocity impacts: A potential implication of organic matter degradation for micrometeoroid collection experiments. *Geochemical Journal* **53,** 53–67 (2019). Doi: 10.2343/geochemj.2.0549

24. G. Danger, A. Ruf, J. Maillard, J. Hertzog, V. Vinogradoff, Ph. Schmitt-Kopplin, C. Afonso, N. Carrasco, I. Schmitz-Afonso, L. Le Sergeant d'Hendecourt, L. Remusat, Unprecedented molecular diversity revealed in meteoritic insoluble organic matter: the Paris Meteorite's case. *Planetary Science Journal* **1**, 55, 18 pp. (2020). Doi: 10.3847/PSJ/abb60f

25. M. Lecasble, L. Remusat, J.-C. Viennet, B. Laurent, S. Bernard, Polycyclic aromatic hydrocarbons in carbonaceous chondrites can be used as tracers of both pre-accretion and secondary processes. *Geochimica et Cosmochimica Acta* **335**, 2432–255 (2022). Doi: 10.1016/j.gca.2022.08.039

26. K. Slavicinska, D. Duca, D. Egorov, T. Mitra, Y. Carpentier, C. Focsa, C. J. Bennett, C. Pirim, Link between polycyclic aromatic hydrocarbon size and aqueous alteration in carbonaceous chondrites revealed by laser mass spectrometry. *ACS Earth and Space Chemistry* **6**, 1413−1428 (2022). Doi: 10.1021/acsearthspacechem.2c00022

27. P. Schmitt-Kopplin, N. Hertkorn, M. Harir, F. Moritz, M. Lucio, L. Bonal, E. Quirico, Y. Takano, J. P. Dworkin, H. Naraoka, S. Tachibana, T. Nakamura, T. Noguchi, R. Okazaki, H. Yabuta, H. Yurimoto, K. Sakamoto, T. Yada, M. Nishimura, A. Nakato, et al., Soluble organic matter molecular atlas of Ryugu reveals cold hydrothermalism on C-type asteroid parent body. *Nature Communications* **14**, id.6525 (2023). Doi: 10.1038/s41467-023-42075-y

28. D. P. Glavin, M. P. Callahan, J. P. Dworkin, J. E. Elsila, The effects of parent body processes on amino acids in carbonaceous chondrites. *Meteoritics*

and Planetary Science **45**, 1948–1972 (2010). Doi: 10.1111/j.1945-5100.2010.01132.x

29. D. P. Glavin, J. E. Elsila, H. L. McLain, J. C. Aponte, E. T. Parker, J. P. Dworkin, D. H. Hill, H. C. Connolly, D. S. Lauretta, Extraterrestrial amino acids and L enantiomeric excesses in the CM2 carbonaceous chondrite Aguas Zarcas and Murchison. *Meteoritics & Planetary Science* **56,** 148–173 (2021). Doi: 10.1111/maps.13451

30. G. D. Cody, C. M. O. Alexander, D. I. Foustoukos, H. Busemann, S. Eckley, A. S. Burton, E. L. Berger, M. Nuevo, S. A. Sandford, D. P. Glavin, J. P. Dworkin, H. C. Connolly, D. S. Lauretta, D. S., The nature of insoluble organic matter in Sutter's Mill and Murchison carbonaceous chondrites: Testing the effect of X-ray computed tomography and exploring parent body organic molecular evolution. *Meteoritics and Planetary Science* **59**, 3–22 (2024). Doi: 10.1111/maps.14096

31. M. E. Zolensky, R. N. Clayton, T. Mayeda, J. Chokai, O. R. Norton, Carbonaceous chondrite clasts in the halite-bearing H5 chondrite Zag. *Meteoritics and Planetary Science* **38**, abstract 5216 (2023).

32. Y. Kebukawa, M. Ito, M. E. Zolensky, R. C. Greenwood, Z. Rahman, H. Suga, A. Nakato, Q. H. S. Chan, M. Fries, Y. Takeichi, Y. Takahashi, K. Mase, K. Kobayashi, A novel organic-rich meteoritic clast from the outer solar system. *Nature Scientific Reports* **9**, id.3169 (2019). Doi: 10.1038/s41598-019-39357-1

33. M. E. Zolensky, D. W. Mittlefehldt, M. E. Lipschutz, M.-S. Wang, R. N. Clayton, T. Mayeda, M. M. Grady, C. Pillinger, D. Barber, CM chondrites exhibit the complete petrologic range from type 2 to 1. *Geochimica et Cosmochimica Acta* **61**, 5099–5115 (1997). Doi: 10.1016/S0016-7037(97)00357-8

34. L. Browning, H. Y. McSween, M. E. Zolensky, On the origin of rim textures surrounding anhydrous silicate grains in CM carbonaceous chondrites. *Meteoritics and Planetary Science* **35,** 1015–1023 (2000). Doi: 10.1111/j.1945-5100.2000.tb01489.x

35. D. R. Frank, G. R. Huss, K. Nagashima, M. E. Zolensky, Sub-zero alteration in an isotopically heavy brine preserved in a pristine H chondrite xenolith. *51st Lunar and Planetary Science Conference*, Abstract id.2911 (2020).

36. P. Jenniskens, H. A. R. Devillepoix, Review of asteroid-meteor-meteorite type links. *Meteoritics & Planetary Science* **60**, 928–973 (2025). Doi: 10.1111/maps.14321

37. B. Harvison, M. de Prá, N. Pinilla-Alonso, V. Lorenzi, J. de León, D. Morate, J. Licandro, A. Arredondo, H. Campins. PRIMASS Near-Infrared Study of the Erigone collisional family. Astronomy & Astrophysics *Icarus* **412**, id.115973 (2024). Doi: 10.1016/j.icarus.2024.115973

38. M. Brož, P. Vernazza, M. Marsset, R. P. Binzel, F. DeMeo, M. Birlan, F. Colas, S. Anghel, S. Bouley, C. Blanpain, J. Gattacceca, S. Jeanne, L. Jorda, J.

Lecubin, A. Malgoyre, A. Steinhausser, J. Vaubaillon, B. Zanda, Source regions of carbonaceous meteorites and near-Earth objects. *Astronomy & Astrophysics* **689**, A183, 24 pp. (2024). Doi: 10.1051/0004-6361/202450532

39. S. Fornasier, C. Lantz, D. Perna, H. Campins, M. A. Barucci, D. Nesvorný, Spectral variability on primitive asteroids of the Themis and Beagle families: Space weathering effects or parent body heterogeneity? *Icarus* **269,** 1–14 (2016). Doi: 10.1016/j.icarus.2016.01.002

40. M. Marsset, P. Vernazza, M. Birlan, F. DeMeo, R. P. Binzel, C. Dumas, J. Milli, M. Popescu, Compositional characterisation of the Themis family. *Astronomy & Astrophysics* **586**, A15, 9pp (2016). Doi: 10.1051/0004-6361/201526962

41. D. Takir, J. P. Emery, Outer Main Belt asteroids: Identification and distribution of our 3-mm spectral groups. *Icarus* **219**, 641–654 (2012). Doi: 10.1016/j.icarus.2012.02.022

42. H. Campins, K. Hargrove, N. Pinilla-Alonso, E. S. Howell, M. S. Kelley, J. Licandro, T. Mothé-Diniz, Y. Fernández., J. Ziffer, Water ice and organics on the surface of the asteroid 24 Themis. *Nature* **464**, 1320–1321 (2010). Doi: 10.1038/nature09029

43. H. H. Hsieh, B. Novaković, K. J. Walsh, Schörghofer N. Potential Themis-family asteroid contribution to the Jupiter-family comet population. *The Astronomical Journal* **159**, id.179, 10pp (2020). Doi: 10.3847/1538-3881/ab7899

44. D. Nesvorny, P. Jenniskens, H. F. Levison, W. F. Bottke, D. Vokrouhlicky, M. Gounelle, Carbonaceous micrometeorites. Implications for hot debris disks. *The Astrophysical Journal* **713**, 816–836 (2010). Doi: 10.1088/0004-637X/713/2/816

References in Supplemental Materials and Methods document:

45. M. Hankey, V. Perlerin, D. Meisel, The All-Sky-6 and the video meteor archive system of the AMS ltd. *Planetary and Space Science* **190**, id.105005 (2020). Doi: 10.1016/j.pss.2020.105005

46. P. Jenniskens, M. D. Fries, Q.-Z. Yin, et al. (70 authors), Radar–enabled recovery of the Sutter's Mill meteorite, a carbonaceous chondrite regolith breccia. *Science* **338**, 1583–1587 (2012). Doi: 10.1126/science.12271

47. J. Borovička, O. Popova, P. Spurný, The Maribo CM2 meteorite fall – Survival of weak material at high entry speed. *Meteoritics & Planetary Science* **54**, 1024–1041 (2019). Doi: 10.1111/maps.13259

48. A. J. King, L. Daly, J. Row, K. Joy et al. (122 co-authors), The Winchcombe meteorite, a unique and pristine witness from the outer solar system. *Science Advances* **8**, eabq3925 (2022). Doi:10.1126/sciadv.abc3925.

49. R. A. Ketcham, Computational methods for quantitative analysis of three-dimensional features in geological specimens. *Geosphere* **1**, 32–41 (2005). Doi: 10.1130/GES00001.136

549 50. R. J. Macke, G. J. Consolmagno, D. T. Britt, Density, porosity and
550 magnetic susceptibility of carbonaceous chondrites. *Meteoritics & Planetary*
551 *Science* **46**, 1842–1862 (2011). Doi: 10.1111/j.1945-5100.2011.01298.x

552 51. A. Cardona, S. Saalfeld, J. Schindelin, I. Arganda-Carreras, S. Preibisch, M.
553 Longair, P. Tomancak, V. Hartenstein, R. J. Douglas, TrakEM2 software for
554 neural circuit reconstruction. *PLoS One* **7**, e38011 (2012). Doi:
555 10.1371/journal.pone.0038011

556 52. J. M. Friedrich, M. M. Chen, S. A. Giordano, O. K. Matalka, J. W.
557 Strasser, K. A. Tamucci, M. L. Rivers, D. S. Ebel, Size-frequency distributions
558 and physical properties of chondrules from x-ray computed microtomography
559 and digital data extraction. *Microscopy Research and Technique* **85**, 1814–1824
560 (2022). Doi: 10.1002/jemt.24043

561 53. T. Zingg, Beitrag zur Schotteranalyse: Die Schotteranalyse und ihre
562 Anwendung auf die Glattalschotter. *Schweizerische Mineralogische Und*
563 *Petrographische Mitteilungen* **15**, 39–140. 41 (1935).

564 54. S. J. Blott, K. Pye, Particle Shape: A review and new methods of
565 characterization and classification. *Sedimentology* **55**, 31–63 (2008). Doi:
566 10.1111/j.1365-3091.2007.00892.x

567 55. J. M. Friedrich, E. M. Riveros, R. J. Macke, S. J. Jaret, M. L. Rivers, D.
568 S. Ebel, Physical properties, internal structure, and the three-dimensional
569 petrography of CI chondrites. *Meteoritics and Planetary Science* **60**, 632–645
570 (2025). Doi: 10.1111/maps.14320

571 56. Y. Kebukawa, E. Quirico, E. Dartois, (55 authors), Infrared absorption spectra
572 from organic matter in the asteroid Ryugu samples: Some unique properties
573 compared to unheated carbonaceous chondrites. *Meteoritics & Planetary Science*
574 **59**, 1845–1858 (2024). Doi: doi.org/10.1111/maps.14064

575 57. Y. Takeichi, N. Inami, H. Suga, C. Miyamoto, T. Ueno, K. Mase, Y.
576 Takahashi, K. Ono, Design and performance of a compact scanning transmission
577 X-ray microscope at the Photon Factory. *Review of Scientific Instruments* **87**,
578 id.013704 (2016). Doi: 10.1063/1.4940409

579 58. Y. Kebukawa, J. Mathurin, E. Dartois, A. Dazzi, A. Deniset-Besseau, J.
580 Duprat, L. Rémusat, T. Noguchi, A. Miyake, Y. Igami, M. Verdier Paoletti, M.
581 E. Zolensky, C. Engrand, C. Sandt, F. Borondics, S. Yamashita, D. Wakabayashi,
582 Y. Takeichi, Y. Takahashi, Complex mixture of organic matter in a xenolithic
583 clast from the Zag meteorite revealed by coordinated analyses using AFM-IR,
584 NanoSIMS and STXM/XANES. *Icarus* **400**, 115582 (2023). Doi:
585 10.1016/j.icarus.2023.115582

586 59. Z. Gainsforth, G. Dominguez, K. Amano, et al. (32 authors), Coevolution
587 of phyllosilicate, carbon, sulfide, and apatite in Ryugu's parent body. *Meteoritics*
588 *& Planetary Science* **59**, 2073–2096 (2024). Doi: 10.1111/maps.14161

589 60. J. L. Kirschvink, R. E. Kopp, T. D. Raub, C. T. Baumgartner, J. W. Holt,
590 Rapid, precise, and high-sensitivity acquisition of paleomagnetic and rock-

591 magnetic data: Development of a low-noise automatic sample changing system
592 for superconducting rock magnetometers. *Geochemistry, Geophysics,*
593 *Geosystems* **9**, 1–18 (2008). Doi: 10.1029/2007GC001856

594 61. R. E. Kopp, B. P. Weiss, A. C. Maloof, H. Vali, C. Z. Nash, J. L.
595 Kirschvink, Chains, clumps, and strings: Magnetofossil taphonomy with
596 ferromagnetic resonance spectroscopy, *Earth Planet. Sci. Lett.* **247**, 10–25
597 (2006). Doi: 10.1016/j.epsl.2006.05.001

598 62. C. Maurel, J. Gattacceca, Estimating paleointensities from chemical
599 remanent magnetizations of magnetite using non-heating methods. *J.*
600 *Geophysical Research Planets* **128**, e2023JE007779 (2023). Doi:
601 10.1029/2023JE007779

602 63. T. Hiroi, K. Ohtsuka, M. E. Zolensky, M. J. Rutherford, R. E. Milliken, Tagish
603 Lake is still the only possible meteorite sample from D-type asteroids. 53th *Lunar*
604 *Planetary Science Conference*, Held 16-20 March 2020 at The Woodlands,
605 Texas, LPI Contribution No. 2326, id.1149 (2022).

606 64. N. O. Ogawa, Y. Kebukawa, M. Zolensky, Y. Takano, N. Ohkouchi,
607 Isotopic measurements of <100 ng carbon and nitrogen through EA/IRMS and its
608 application to extraterrestrial materials. *82nd Annual Meeting of the Meteoritical*
609 *Society*, held 7-12 July 2019 in Sapporo, Japan. LPI Contribution No. 2157, id.
610 6208 (2019).

611 65. N. O. Ogawa, T. Nagata, H. Kitazato, N. Ohkouchi, Ultra-sensitive
612 elemental analyzer/isotope ratio mass spectrometer for stable nitrogen and carbon
613 isotope analyses. In: *Earth, Life, and Isotopes* (Eds.: N. Ohkouchi, I. Tayasu, and
614 K. Koba), Kyoto University Press, pp.339–353 (2010).

615 66. Y. Isaji, N. O. Ogawa, C. J. Boreham, Y. Kashiyama, N. Ohkouchi,
616 Evaluation of $\delta^{13}C$ and $\delta^{15}N$ uncertainties associated with the compound-specific
617 isotope analysis of geoporphyrins. *Analytical Chemistry* **92**, 3152–3160 (2020).
618 Doi: 10.1021/acs.analchem.9b04843

619 67. I. Tayasu, R. Hirasawa, N. O. Ogawa, N. Ohkouchi, K. Yamada, New
620 organic reference materials for carbon- and nitrogen-stable isotope ratio
621 measurements provided by Center for Ecological Research, Kyoto University,
622 and Institute of Biogeosciences, Japan Agency for Marine-Earth Science and
623 Technology. *Limnology* **12**, 261–266 (2011). Doi:10.1007/s10201-011-0345-5

624 68. M. A. Sephton, A. B. Verchovsky, P. A. Bland, I. Gilmour, M. M. Grady,
625 I. P. Wright, Investigating the variations in carbon and nitrogen isotopes in
626 carbonaceous chondrites. *Geochimica et Cosmochimica Acta* **67**, 2093–2108
627 (2003). Doi: 10.1016/S0016-7037(02)01320-0

628 69. K. Nishiizumi, M. W. Caffee, Y. Hamajima, R. C. Reedy, K. C. Welten,
629 Exposure history of the Sutter's Mill carbonaceous chondrite. *Meteoritics*
630 *Planetary Science* **49**, 2056–2063 (2014). Doi: 10.1111/maps.12297

631 70. P. Sharma, M. Bourgeois, D. Elmore, D. Granger, M. E. Lipschutz, X.
632 Ma, T. Miller, K. Mueller, F. Rickey, P. Simms, S. Vogt, PRIME lab AMS

performance, upgrades and research applications. *Nuclear Instruments and Methods in Physics Research* **B172**, 112–123 (2000). Doi: 10.1016/S0168-583X(00)00132-4

71. H. Busemann, H. Baur, R. Wieler, Primordial noble gases in "Phase Q" in carbonaceous and ordinary chondrites studied by closed system stepped etching. *Meteoritics & Planetary Science* **35**, 949–973 (2000). Doi: 10.1111/j.1945-5100.2000.tb01485.x

72. M. E. I. Riebe, K. C. Welten, M. M. M. Meier, R. Wieler, M. I. F. Barth, D. Ward, A. Bischoff, M. W. Caffee, K. Nishiizumi, H. Busemann, Cosmic-ray exposure ages of six chondritic Almahata Sitta fragments, *Meteoritics & Planetary Science* **52**, 2353–2374 (2017). Doi: 10.1111/maps.12936

73. D. L. Schrader, Z. A. Torrano, D. I. Foustoukos, C. M. O'D. Alexander., J. Render, G. A. Brennecka, Reassessing the proposed "CY chondrites": Evidence for multiple meteorite types and parent bodies from Cr-Ti-H-C-N isotopes and bulk elemental compositions. *Geochimica et Cosmochimica Acta* **390**, 24–37 2025). Doi: 10.1016/j.gca.2024.12.021

74. C. M. O'D. Alexander, Quantitative models for the elemental and isotopic fractionations in chondrites: The carbonaceous chondrites. *Geochimica et Cosmochimica Acta* **254**, 277-309 (2019). Doi: 10.1016/j.gca.2019.02.008

75. I. Leya, J. Masarik, Cosmogenic nuclides in stony meteorites revisited, *Meteoritics & Planetary Science* **44**, 1061-1086 (2009). Doi: 10.1111/j.1945-5100.2009.tb00788.x

76. A. Ruf, B. Kanawati, N. Hertkorn, Q.-Z. Yin, F. Moritz, M. Harir, M. Lucio, B. Michalke, J. Wimpenny, S. Shilobreeva, B. Bronsky, V. Saraykin, Z. Gabelica, R. D. Gougeon, E. Quirico, S. Ralew, T. Jakubowski, H. Haack, M. Gonsior, P. Jenniskens, N. W. Hinman, P. Schmitt-Kopplin, Previously unknown class of metalorganic compounds revealed in meteorites. *PNAS* **114**, id.2819-2824 (2017). Doi: 10.1073/pnas.1616019114

77. P. Schmitt-Kopplin, Z. Gabelica, R. D. Gougeon, A. Fekete, B. Kanawati, M. Harir, I. Gebefuegi, G. Eckel, N. Hertkorn, High molecular diversity of extraterrestrial organic matter in Murchison meteorite revealed 40 years after its fall. *Proceedings of the National Academy of Sciences* **107**, 2763–2768 (2010). Doi: 10.1073/pnas.091215710

78. J. C. Aponte, H. L. McLain, D. N. Simkus, J. E. Elsila, D. P. Glavin, E. T. Parker, J. P. Dworkin, D. H. Hill, H. C. Connolly Jr., D. S. Lauretta, Extraterrestrial organic compounds and cyanide in the CM2 carbonaceous chondrites Aguas Zarcas and Murchison. *Meteoritics & Planetary Science* **55**, 1509–1524 (2020). Doi: 10.1111/maps.13531

79. J. C. Aponte, R. Tarozo, M. R. Alexandre, C. M. D. Alexander, S. B. Charnley, C. Hallmann, R. E. Summons, Y. Huang, Chirality of meteoritic free and IOM-derived monocarboxylic acids and implications for prebiotic organic

synthesis. *Geochimica et Cosmochimica Acta* **131**, 1–12 (2014). Doi: 10.1016/j.gca.2014.01.035

80. J. C. Aponte, H. K. Woodward, N. M. Abreu, J. E. Elsila, J. P. Dworkin, Molecular distribution, ^{13}C-isotope, and enantiomeric compositions of carbonaceous chondrite monocarboxylic acids. *Meteoritics & Planetary Science* **54**, 415–430 (2019). Doi: 10.1111/maps.13216

81. F. Robert, S. Epstein, The concentration and isotopic composition of hydrogen, carbon and nitrogen in carbonaceous meteorites. *Geochimica et Cosmochimica Acta*, **46**, 81–95 (1982). Doi: 10.1016/0016-7037(82)90293-9

82. D. P. Glavin, J. P. Dworkin, C. M. O'D. Alexander, J. C. Aponte, A. A. Baczynski, J. J. Barnes, et al. (62 authors). Abundant ammonia and nitrogen-rich soluble organic matter in samples from asteroid (101955) Bennu. *Nature Astronomy* **9**, 199–210 (2025). Doi: 10.1038/s41550-024-02472-9

83. M. Fries, J. Fries, Weather Radar Detection and Analysis of Bolides in the Day or Night. Advances in Astronomy **2025**, id.3041760, 10pp (2025). Doi: 10.1155/aa/3041760

Acknowledgments: Several NASA centers contributed to this work. We gratefully acknowledge the access to the Electron Beam Analysis Labs at NASA JSC. The Laboratory Directed Research and Development (LDRD) program at Sandia National Laboratories is a multimission laboratory managed and operated by National Technology and Engineering Solutions of Sandia, LLC., a wholly owned subsidiary of Honeywell International, Inc., for the U.S. Department of Energy's National Nuclear Security Administration under contract DE-NA-0003525 (EAS). Part of this work was performed under the auspices of the U.S. Department of Energy by Lawrence Livermore National Laboratory under Contract DE-AC52-07NA27344 with release number LLNL-JRNL-2006811.

Funding:

NASA grants 80NSSC18K0854 and 80NSSC22K1467 (PJ).

NASA Hayabusa2 Participating Scientist Program funding through the Johnson Space Flight Center (MEZ).

NASA grant 80NSSC22K1693 (KCW, KN, MWC).

NASA's Planetary Science Division Internal Scientist Funding Program through the Fundamental Laboratory Research (ISFM) work package at Goddard Space Flight Center and the Goddard Center for Astrobiology (DPG, JPD, HLM, AM).

NASA ISFM funding to the JSC Coordinated Analysis Work Package (JH, MEZ, LL).

NASA Planetary Science Enabling Facilities program 80NSSC23K0198 to RELAB, a multi-user facility (TH).

Japan Society for the Promotion of Science KAKENHI Grants JP21KK0062 (YT), JP23H00153 (NO, NOO), JP24K00750 (NOO), JP23H01286, and JP23K17700 (YK).

German Research Foundation (DFG)—Project-ID 364653263—TRR 235 (CRC 235) and Project-ID 521256690—TRR 392/1 2024 (CRC 392/1 B2) (PSK and ML).

The Royal Society International Exchanges Scheme- Standard Programme (IES\R3\223015) (QHSC)

The Science and Technology Facilities Council (STFC) Astronomy Small Award Research Grant (ST/Y002687/1) (QHSC, DB, JSW, MAS).

The Swiss National Science Foundation (SNF) grants # 200020_182649 and 200020_219860 (HB, DK).

Author contributions:

Conceptualization: PJ, MZ, MH,

Methodology: PJ, MZ, NOO, NO, YT, QHSC, JB, ZG, PSK

Investigation: PJ, MZ, NOO, TH, QHSC, DB, JSW, BM, GAB, JHR, YK, MS, SMT, JJ, PSK

Visualization: PJ

Funding acquisition: PJ, NOO, QHSC, MAS, YK

Project administration: PJ,

Supervision: PJ, MZ, QHSC, MAS

Writing – original draft: PJ, MZ

Writing – review & editing: all authors contributed

Writing – Supporting Materials and Methods: all authors contributed

Competing interests: Authors declare that they have no competing interests.

Data and materials availability:

Meteorite samples for research are available from the American Museum for Natural History upon request. All data are available in the main text or the supplementary materials.

Supplementary Materials

This PDF file includes:

Supplementary Materials and Methods

Figs. S-1 to S-28

Tables S-1 to S-15

Fig. 1. Impact and recovery of Hillsborough. (A) The daytime meteor with wake in a single frame from Northford, CT; **(B)** The impact site in Hillsborough; **(C)** View of the impact site from inside; **(D)** Meteorite fragment with fusion crust.

Fig. 2. C1 clasts in Hillsborough. (A) Back-scattered electron image with two C1 clasts circled. **(B)** Na X-ray map of the same area as (A), indicating Na enrichment of the C1 clasts relative to the bulk of Hillsborough.

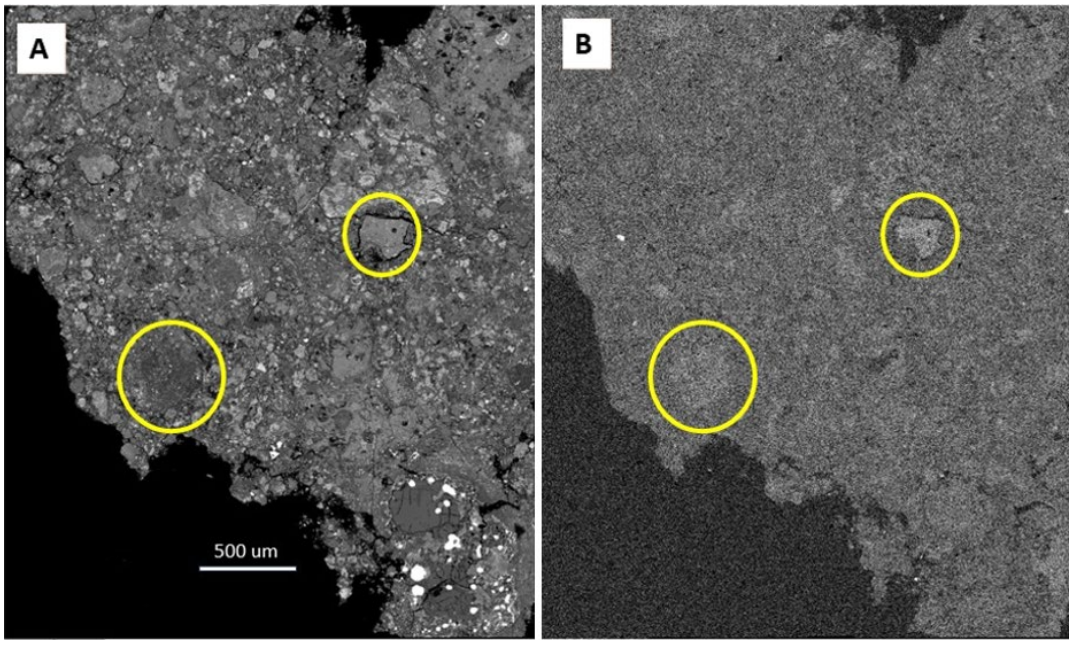

Fig. 3. Na enriched veins in C1 clasts shown in Fig 2. **(A)** C1 clast containing numerous magnetite (white), pyrrhotite (light grey) and dolomite grains (dark grey). **(B)** C1 clast with numerous dolomites marked "D", indicating the dolomite crystal where the FIB was cut (bottom, arrowed and outlined in yellow). **(C)** Bright field TEM image of the FIBed dolomite crystal. Numerous cracks are arrowed. **(D)** Na X-ray map of the same area as in (C).

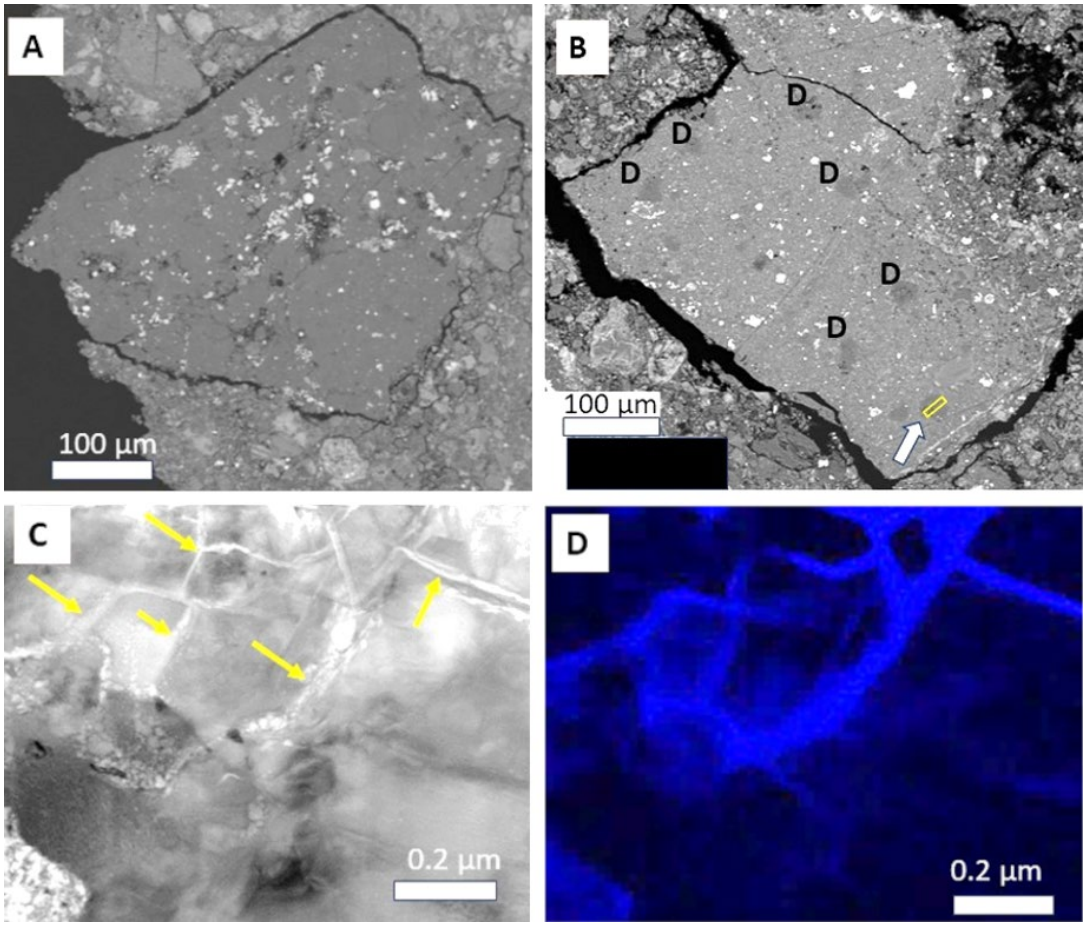

Fig. 4. Data visualization of the surface laser desorption analysis with LD(+)-FT-ICR mass spectrometry of CM1/2 Hillsborough compared to CM1/2 Kolang and CM2 Murchison showing all oxidized CHO, CHNO, CHOS and non-oxidized CH, CHN, CHS chemical families with **(A)** classical van Krevelen diagrams; **(B)** and **(C)** mass derived van Krevelen; **(D)** distribution of the chemical formula as a function of their abundance in oxygen; and **(E)** distribution of the formulas as a function of their abundance in nitrogen and sulfur. The bubble size is proportional to the intensity in the mass spectra, while the pie charts give the number of compounds.

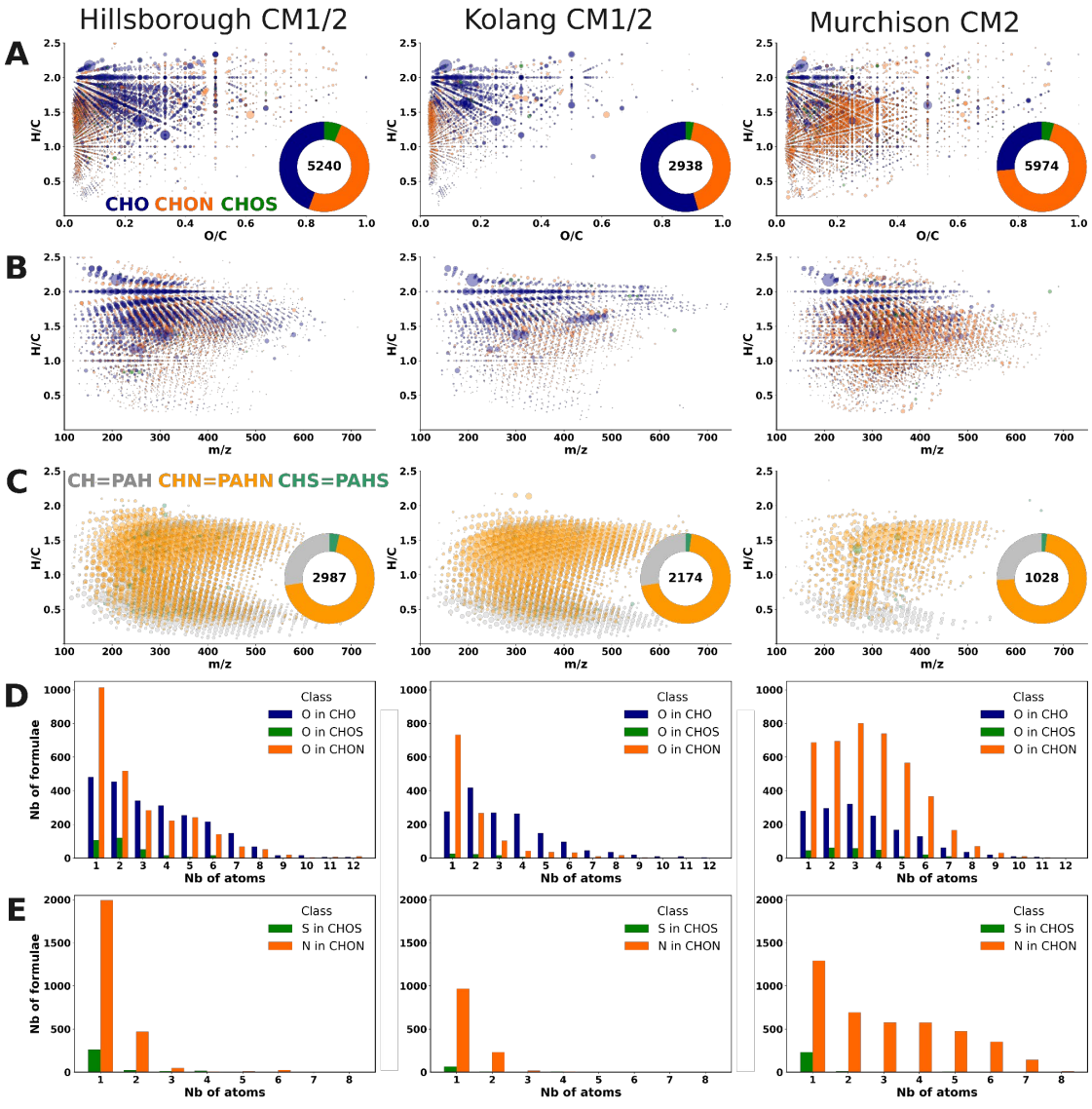

Appendix A. Supplementary Materials and Methods

Meteor trajectory and meteoroid orbit

By: Mike Hankey, Peter Jenniskens

Methods: Daytime Allsky7 camera video records from stations AMS149 and AMS15, with a convergence angle of 38.9º, were calibrated against star background images from the night prior using methods described in (*46*). A linear trajectory and velocity deceleration profile were calculated from a continuous record of the meteor between 44.4 and 34.9 km altitude (26 and 21 frames at 25 frames/second, respectively). In addition, video from a citizen scientist security camera in Wayne, NJ, was calibrated against a night-time star background image matched to near- and far-field foreground features as in (*47*). This data was used to evaluate the uncertainties in the Allsky7 measurements. Both the AMS149 and Wayne cameras captured an additional flare at ~28.2 km altitude.

Table S-1. Meteoroid trajectory and orbital elements (Equinox J2000). Results for Hillsborough are compared to published results for the two night-time CM2 carbonaceous chondrite falls Winchcombe and Maribo.

	Hillsborough (this work)	**Winchcombe** *(45)*	**Maribo** *(46)*
Date	2024-07-16	2021-02-28	2009-01-17
Time (UTC)	15:17:27.60	21:54:15.88	19:08:27.41
Solar longitude (º)	114.2392	340.2435	297.6885
Trajectory:			
First Height (km)	44.4 ± 0.5	90.623 ± 0.038	114.9 ± 0.2
First Latitude (ºN)	40.567 ± 0.003	51.87106 ± 29m	54.584 ± 0.003
First Longitude (ºE)	-74.188 ± 0.005	-3.10932 ± 17m	+13.719 ± 0.003
Last Height (km)	34.9 ± 0.5	27.554 ± 0.028	30.6 ± 0.3
Last Latitude (ºN)	40.530 ± 0.003	51.94011 ± 33m	54.711 ± 0.003
Last Longitude (ºE)	-74.390 ± 0.005	-2.09634 ± 11m	+11.592 ± 0.006
Radiant and speed:			
Apparent V_∞ (km/s)	14.4 ± 0.6	13.547 ± 0.008	28.3 ± 0.3
Apparent R.A. (º)	164.8 ± 0.3	-.-	123.5 ± 0.3
Apparent Dec. (º)	+28.5 ± 0.1	-.-	+21.76 ± 0.15
Azimuth from N (º)	256.0 ± 0.3	263.342 ± 0.046	95.9 ± 0.3
Elevation (º)	29.1 ± 0.2	41.919 ± 0.029	31.2 ± 0.2
Geocentric V (km/s)	8.6 ± 1.1	8.123 ± 0.013	25.8 ± 0.3
Geocentric R.A. (º)	178.6 ± 9.0	56.638 ± 0.017	125.0 ± 0.3
Geocentric Dec. (º)	+19.9 ± 7.2	+17.713 ± 0.069	+19.8 ± 0.2
Orbital elements:			
a (AU)	2.13 ± 0.33	2.5855 ± 0.0077	2.43 ± 0.12
e	0.533 ± 0.074	0.6183 ± 0.0011	0.805 ± 0.010
q (AU)	0.995 ± 0.009	0.986839 ± 0.000012	0.475 ± 0.005
i (º)	4.1 ± 2.1	0.460 ± 0.014	0.25 ± 0.16
ω (º)	159.8 ± 4.2	351.798 ± 0.018	279.4 ± 0.6
Node (º)	114.29 ± 0.07	160.1955 ± 0.0014	297.46 ± 0.15
Last Perihelion	2024-06-29	2021-02-22.446	2005-05-16.0

Petrography

By: Mike Zolensky, Jangmi Han, Loan Le, Marc Fries

Methods: Samples were imaged and analyzed in the E-beam laboratories of Astromaterials Research and Exploration Science (ARES) NASA JSC (Houston). A JEOL 7600F scanning electron microscope was used to collect images and X-ray spectra (EDS). Mineral compositional analyses were measured using a JEOL JXA 8530F electron microprobe (EPMA) at 15kV and 20nA. Natural minerals and alloys were used as standards. We made one ~100 nm thick section from a dolomite crystal from one of the C1 grains using a Quanta 3D FEG Dual Beam Focused Ion Beam instrument. We investigated the mineralogy, chemistry, and microstructures from the FIB slice using a JEOL 2500SE scanning TEM with a JEOL SDD EDX.

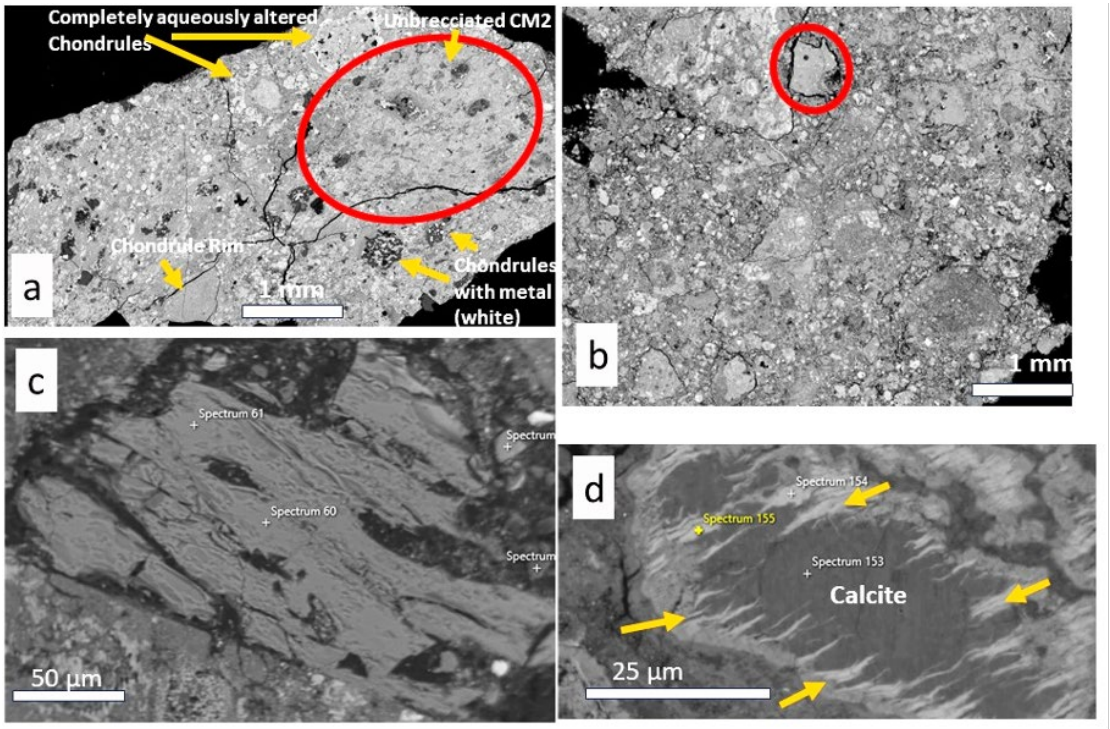

Fig. S-1. Backscattered electron images of Hillsborough. **(A)** Comminuted CM material with one of the larger pieces of unbroken CM2 lithology circled. One fine-grained chondrule rim, two completely aqueously altered chondrules, and two chondrules with remnant metal are also indicated. **(B)** A thoroughly-comminuted sample, containing one of the C1 clasts (circled). This same clast is shown in Figures 2 and 3. **(C)** Partially-dissolved olivine crystal. **(D)** Calcite crystal rimmed and partially penetrated by tochilinite flakes (arrowed).

CM Lithology

The interior of the stones are dark gray to black and sparsely decorated with light-colored grains. The meteorite is unusually finely brecciated for a CM. The largest

continuous fragments observed were 5 mm, and some investigated stones consist entirely of finely comminuted, sub-mm sized fragments (see Fig. S-1).

The stones were exceptionally difficult to polish owing to extreme friability. Tests revealed that some samples would rapidly disaggregate upon contact to water, alcohol and oil. Therefore, no fluids were used for cutting sample preparation, and so all polishing had to be performed dry. This behavior was similar to that we had previously observed for the Tarda chondrite. The result was that very poor, badly-scratched surfaces had to be used for EPMA, resulting in slightly reduced analytical accuracy.

SEM/EDS/EPMA observations and measurements revealed that the bulk matrix is dominated by serpentine, tochilinite, calcite, pyrrhotite, pentlandite, and, to a lesser degree, Fe-Ni metal. Rare matrix phases are Ca-phosphate, magnetite and chromite. Intergrowths of serpentine and tochilinite are common, as is usual for CMs. Fragments of olivine and lesser low-Ca pyroxene are abundant in the matrix, and these exhibit considerable etching by aqueous fluids (see Fig. S-1b). The range of serpentine compositions spanned the entire range observed by the analyses for all other CMs (Fig. S-1b). Metal is mostly confined to small grains within olivine crystals. Aggregates and intergrown (exsolved) crystals of pyrrhotite and pentlandite are abundant. One rather unusual pentlandite crystal was found to contain 11 atomic% Mn.

Sinuous Ca-Al-rich inclusions (CAIs) comprise approximately 2% of the examined samples. These consist of spinel with inclusions of perovskite and are rimmed by probable diopside (the latter being too fine-grained for accurate EPMA measurements). These particular CAIs are typical for CM chondrites.

Chondrules and chondrule pseudomorphs are abundant, and most are fragmented to varying degrees. Most chondrules exhibit thick fine-grained rims, frequently multilayered with respect to bulk FeO content. Chondrules range up to 1 mm in diameter, but the majority are less than 100 μm in diameter. Porphyritic chondrule types predominate. The chondrules and silicate fragments show a range of alteration to hydrous phases and many completely lack anhydrous silicates (Fig. S-1a). There is excellent pseudomorphism of serpentine, tochilinite and calcite after primary ferromagnesian minerals. Fine-grained clasts are abundant, and appear to actually be fine-grained chondrule rims viewed along a plane that does not intersect the underlying chondrule (Fig. S-1a).

Olivine shows a wide compositional range from Fa_2 to Fa_{33} (n=8), with CaO up to 0.42 wt%, Cr_2O_3 up to 0.44 wt%, NiO up to 0.084 wt%, and Al_2O_3 up to 0.20 wt%. As is typical for CMs, calcite is generally fairly pure but some examined crystals contained up to 1.5 wt% MgO and 2.5 wt% FeO. Chromites contain up to 11.5 wt% Al_2O_3 and 3.1 wt% TiO_2.

C1 lithology

A notable feature is the presence of a few small (<500μm), matrix-dominated clasts of C1 material. The bulk matrix in this lithology is still poorly characterized, but

contains up to 2 wt% Na_2O, which is very unusual. EPMA measurements of the matrix are consistent with its being serpentine (Fig. 2, main text), with a rather high Na content. This hypothesis requires confirmation. Scattered within the fine-grained matrix are crystals of dolomite and magnetite (plaquettes and framboids). The dolomites are rimmed by matrix enriched in Na (Fig. 2). To investigate the nature of this Na-rich phase we cut a focused ion beam (FIB) slice across one of the dolomites (Fig. 3). TEM observation revealed that the dolomite was a single continuous crystal, which was cut by numerous fractures (Fig. 3c). X-ray mapping revealed that the fractures are filled with a Na-rich, amorphous phase. It is likely that the phase was rendered amorphous by the electron and X-ray techniques.

Classification: CM1/2. The dominant lithology contains areas with chondrules almost completely replaced by hydrous silicates and intimately associated and mixed with chondrules and ferromagnesian mineral fragments partially replaced by serpentine, tochilinite and calcite (CM1/2), to areas more typical of CM2 meteorites (olivine and metal present). The bulk mineralogy is consistent with CM1 to CM2 meteorites.

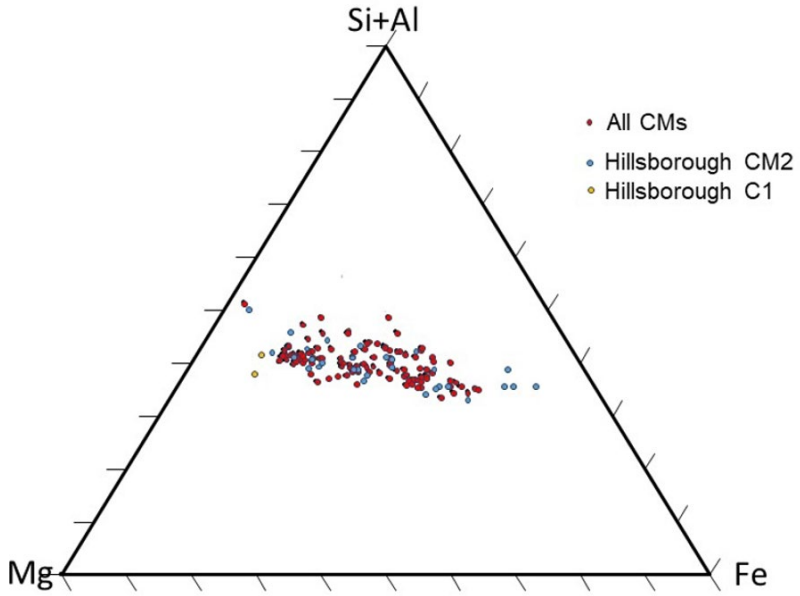

Fig. S-2. Atom percent plot of Hillsborough CM1/2 phyllosilicates (blue) and Hillsborough C1 clast (yellow) compared to serpentine from several CM2 chondrites (red) (unpublished data, M. Zolensky). It is interesting that the Hillsborough CM2 serpentine compositions span the entire range observed for other CM chondrites, while CM1 serpentine compositions plot outside this range.

X-ray Computed Tomography

By: Eva Riveros, Jon Friedrich, and Denton Ebel

Methods: A 0.9946 g fragment of Hillsborough was imaged at the American Museum of Natural History's Microscopy and Imaging Facility by Computed x-ray microtomography (μCT), using a ZEISS Xradia 630 Versa μCT system with current of 125 μA and potential of 80.0 kV (10.0 W power). Data were collected at a resolution of 8.0 μm/voxel edge. Using Blob3D (*49*), the total internal volume of the sample was calculated by digitally isolating the chondrite from the air surrounding the sample. The mass was measured using a calibrated analytical balance. The porosity was calculated by assuming the mean grain density of CM chondrites (2.92 g/cm3) determined by (*50*):

$$P = 1 - \rho bulk / \rho grain, \quad (1)$$

where $\rho bulk$ and $\rho grain$ are bulk and grain densities, respectively. ImageJ and the TrakEM2 application (*51*) were used to visually identify and digitally isolate unbrecciated CM clasts within the sample following the same methods used to isolate individual chondrules by (*52*). Blob3D was used to calculate clast volume and axial dimensions. A best-fit ellipsoid's principal axes was used to calculate the shape according to (*53*) using the shape categories of (*54*).

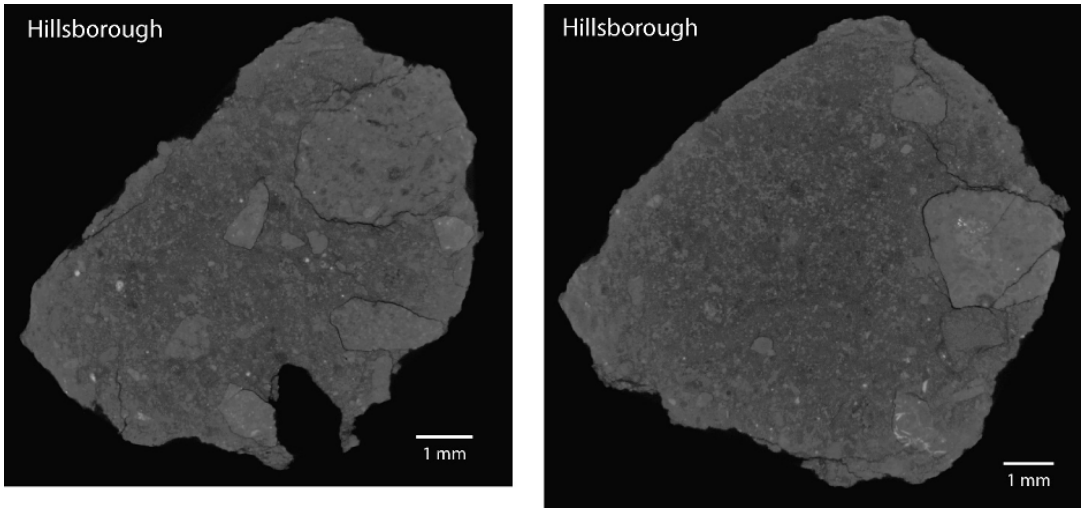

Fig. S-3. Two μCT "slices" of central portions of the same ~1g chip of the Hillsborough carbonaceous chondrite. Within these images, lighter greyscale values represent greater x-ray attenuation. The air around the sample and the low atomic weight material surrounding some clasts are represented by the darkest greyscale values while silicates are depicted by lighter greyscale values. Clasts of variable composition can be readily distinguished from others and from the surrounding heavily comminuted material. What are likely unbrecciated CM clasts are often surrounded by low average atomic weight material, probably air.

Results: A 0.9946 g sample of the Hillsborough CM chondrite was imaged. Digitally isolating the chondrite yields a volume of 0.525 cm3 and gives a resulting bulk

density of 1.89 g/cm^3. This bulk density is near the lower end of the full range (1.88 – 2.47 g/cm^3) for CM chondrite bulk density reported by (*50*). Assuming the mean CM grain density of 2.92 g/cm^3 (*50*), the corresponding porosity is 35.3%. This lies at the higher end of porosity range (15.0 – 36.7%) reported for CM chondrites by (*50*). The low bulk density and high porosity of Hillsborough are probably due to the substantial void space (cracks) surrounding some clasts in the sample (Fig. S-3) in addition to the substantial unresolvable microporosity that exists in volumes below the resolution (8.0 μm/voxel) of our CT image scans.

The ~10 mm diameter fragment of Hillsborough contains many obvious clasts of material that appear to be unbrecciated, likely representing the CM unbrecciated material seen in SEM images of Hillsborough thin sections (cf. Fig. S-3). These clasts are rimmed by low X-ray attenuation material and we interpret this as porosity (air) rather than another low-Z material such as a carbon-rich component. We have digitally isolated these clasts and a 3D representation of them is shown in Fig. S-4. They comprise only 7% of the total volume of the ~ 10 mm diameter Hillsborough sample. These mostly sub-equant spheroidal clasts (Fig. S-5) possess shapes like those of other melt free impact breccias such as those found in CI chondrites (*55*).

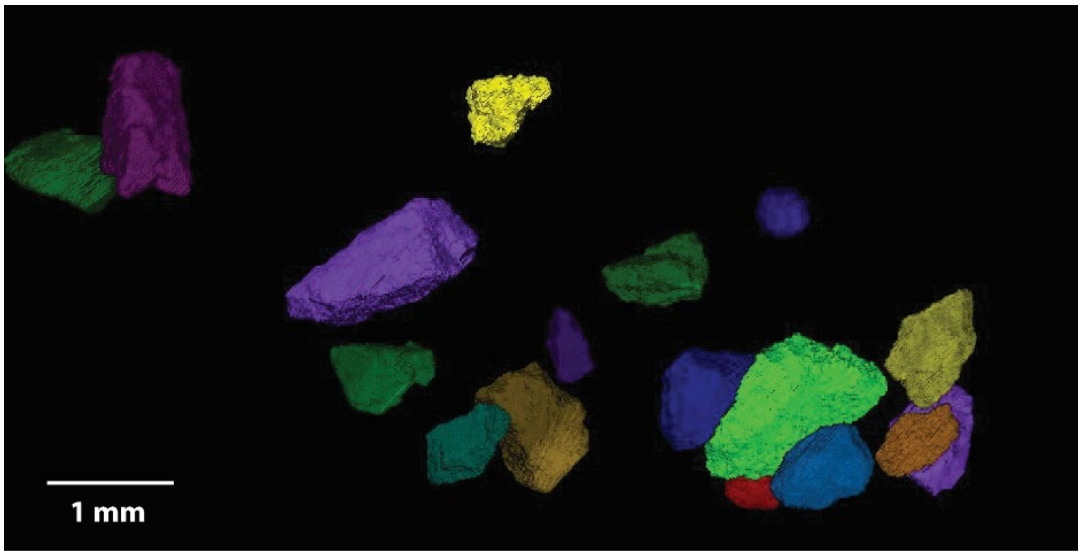

Fig. S-4. Digitally isolated clasts within the ~10 mm diameter Hillsborough chondrite subsample shown in Figure S-3. These clasts are likely unbrecciated CM chondrite material.

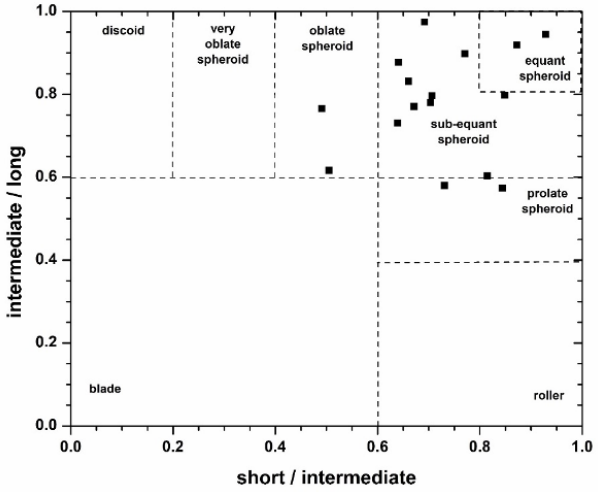

Fig. S-5. Zingg diagram (*53*) using axial ratios to examine unbrecciated chondrite clast shapes in Hillsborough using the terminology of (*54*). These shape data are based on best-fit ellipsoids constructed around each clast using Blob3D. The mostly sub-equant spheroidal clasts possess shapes like melt-free impact breccias on other solar system bodies.

FTIR analysis of individual grains

By: Y. Kebukawa

Methods: Fourier transform infrared micro-spectroscopy (micro-FTIR) measurements were conducted at Institute of Science Tokyo as explained in the methods described in (*56*). Grains were pressed between two diamond windows (3.5 mm diameter and 0.3 mm thick). After separation of the two diamond windows, usually the samples are evenly distributed on both windows. IR absorption spectra were collected from each diamond window with a micro-FTIR (JASCO FT/IR-6100+IRT-5200), equipped with a ceramic IR light source, a germanium-coated KBr beam splitter, a liquid-nitrogen cooled mercury-cadmium-telluride (MCT) detector, and ×16 Cassegrain mirrors. An Ar flow heating stage (Linkam 10036L) was used to eliminate adsorbed water.

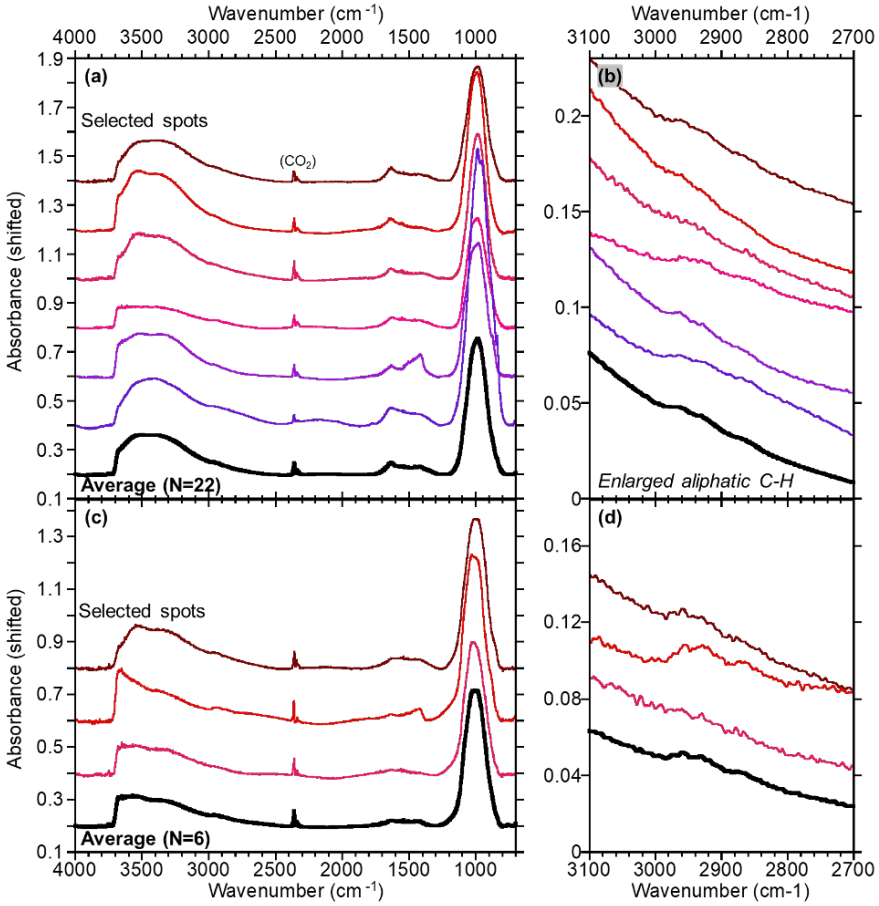

Fig. S-6. Infrared transmission spectra of the Hillsborough meteorite. **(A)** Some selected spectra obtained from 20 μm × 20 μm area and the average spectra (22 spots), and the enlarged aliphatic C-H spectra are shown in **(B)**. **(C)** Spectra (25 μm × 25 μm area) obtained by mild heating (60 °C) in an N_2 flow to remove terrestrial adsorbed water.

963 Results: The spectra show a large band at ~3400 cm^{-1} assigned to water
964 (adsorbed/interlayer) with a shoulder at 3675 cm^{-1} assigned to structural OH, a
965 strong SiO peak at ~1010 cm^{-1} consistent with phyllosilicates, a band at 1420 cm^{-1}
966 assigned to carbonates, a band at 1630 cm^{-1} assigned to aromatic carbon with
967 adsorbed water, and an aliphatic C-H triplet band at 2960, 2930, and 2860 cm^{-1}
968 assigned to asymmetric stretch of CH_3, asymmetric stretch of CH_2, and symmetric
969 stretch of CH_3+CH_2, respectively. The ~3400 cm^{-1} and 1630 cm^{-1} bands are
970 decreased by mild heating. The shape of the 3400 cm^{-1} band shows some variation
971 due to the heterogeneity of the OH-bearing minerals. There are some carbonate rich
972 spots.

973

Scanning transmission X-ray microscopy and C-XANES spectroscopy

By: Y. Kebukawa, Z. Gainsforth, M. Suzuki

Methods: Ultrathin sections (approximately 100 nm thick) were prepared using a focused ion beam (FIB) system (SMI3200, SII NanoTechnology Inc.), at Photon Factory, High-Energy Accelerator Research Organization (KEK). C and N *K*-edge X-ray absorption near-edge structure (XANES) analyses were performed with the scanning transmission X-ray microscope (STXM) at BL19A, Photon Factory, High-Energy Accelerator Research Organization (KEK) (*57*), with the similar methods shown in (*58*). Microspectral image stacks were acquired with 0.06 μm steps per pixel for 5 × 5 to 5 × 8 μm^2 areas. C-stacks were analyzed using an autoencoder neural network with in-house software in Python (*59*).

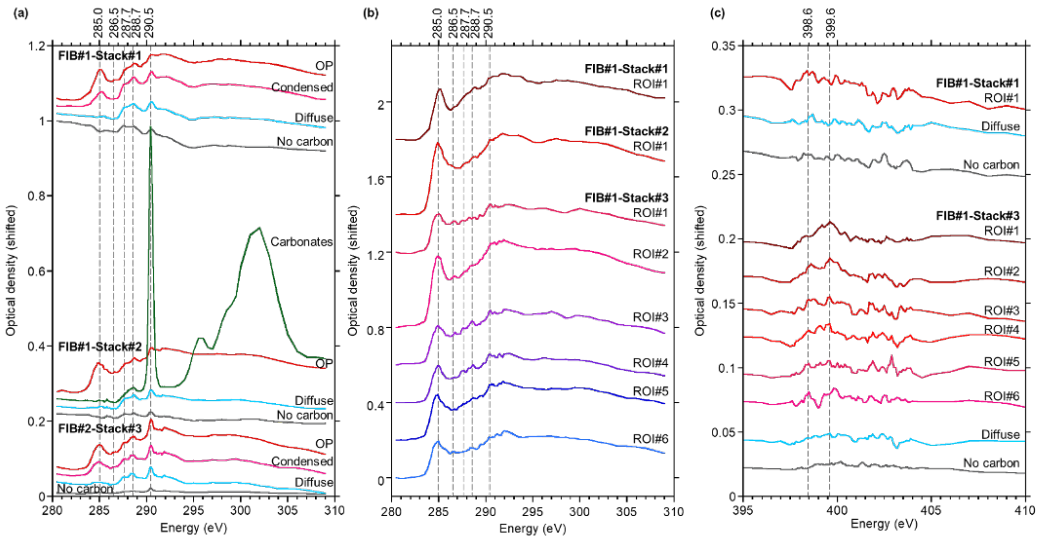

Fig. S-7. C-XANES spectra of the Hillsborough meteorite. **(A)** Average C-XANES spectra from each phase shown in phase images generated by the autoencoder. **(B)** C-XANES spectra from selected regions of interest (ROIs) on organic particles. ROI positions are indicated by numbers in Fig. S-8c-e. **(C)** N-XANES spectra from the ROIs, compared to N-XANES from diffuse and no-carbon regions. C-XANES peak assignments are: 285.0 eV aromatic C, 286.5 eV C=O, 287.7 eV aliphatic C, 288.7 eV C(=O)O, and 290.5 eV organic/inorganic carbonates. N-XANES peak assignments are: 398.6 eV pyridinic N, and 399.6 eV pyridinic N/nitriles.

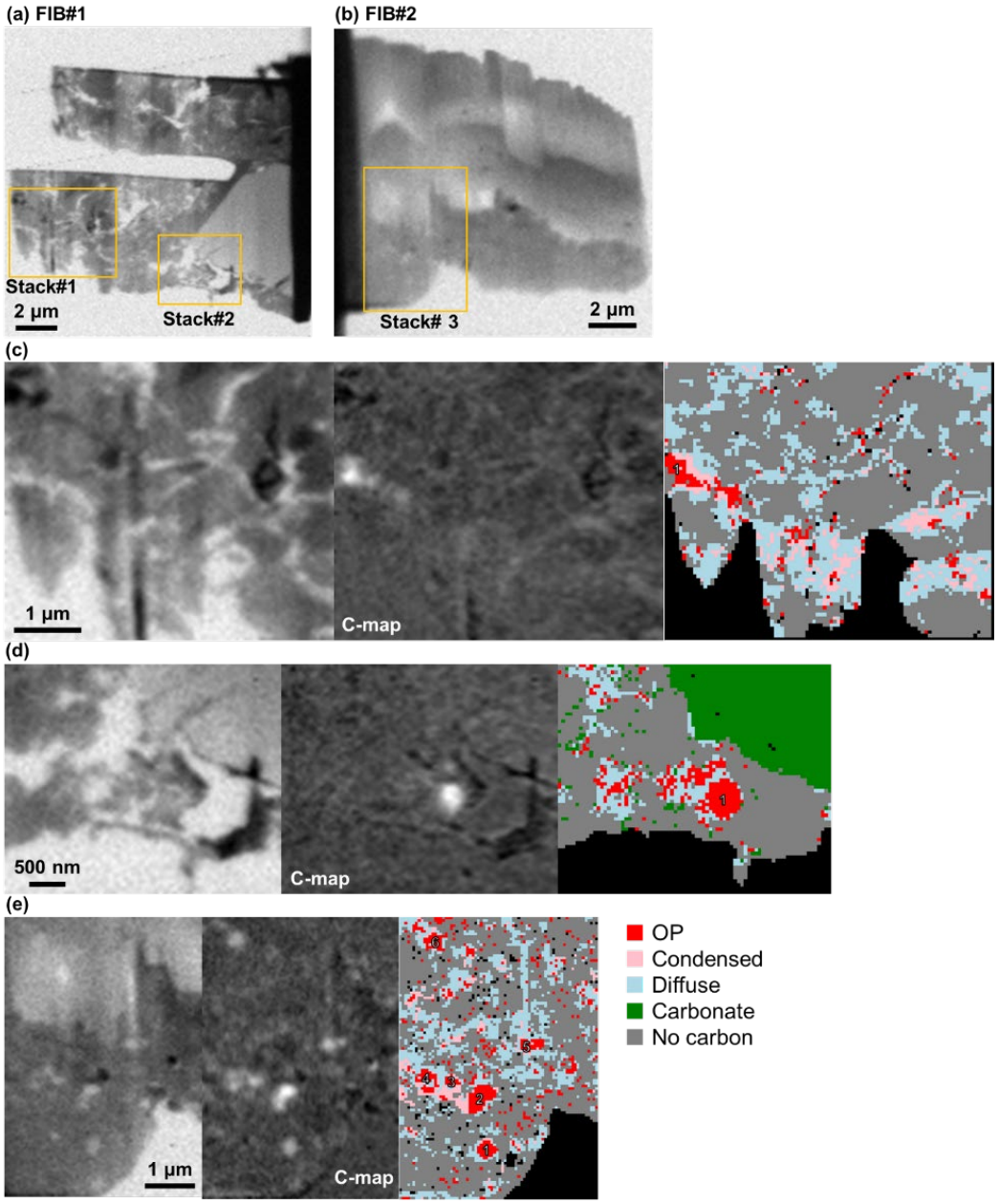

Fig. S-8. (A,B) Scanning transmission X-ray microscope (STXM) image at 280 eV of FIB lamellae from the Hillsborough meteorite. "Stack" images for carbon X-ray absorption near-edge structure (XANES) are obtained from areas indicated by rectangles. **(C-E)** (left panels) Enlarged STXM images at 280 eV, (middle panels) C-map obtained from two images at pre-edge (280 eV) and post-edge (292 eV), and (right panels) phase images generated from autoencoder machine learning of (c) Stack #1, (d) Stack#2, and (e) Stack#3. The average C-XANES spectrum from each phase is shown in Fig. S-7. Red: Organic Particles (OP), pink: condensed organics, light blue: diffuse organics, greed: carbonates, and gray: no/little organics.

Paleomagnetic and rock magnetic analysis

By: Sonia Tikoo-Schantz & Ji In Jung

Methods: A 0.149 g fragment was transported in a magnetically shielded case from Hillsborough to Stanford University and subjected to paleomagnetic and rock magnetic characterization. We conducted alternating field (AF) demagnetization of natural remanent magnetization (NRM). In addition, we measured anhysteretic remanent magnetization (ARM) (ac field = 100 mT and dc bias fields ranging from 0.05 mT to 0.8 mT) and isothermal remanent magnetization (IRM) acquisition (dc fields = 100 mT and 900 mT) (*60*). All experiments were conducted using a 2G Enterprises 755 superconducting rock magnetometer (sensitivity: 10^{-12} Am^2) housed within a ~300 nT ambient field magnetically shielded room.

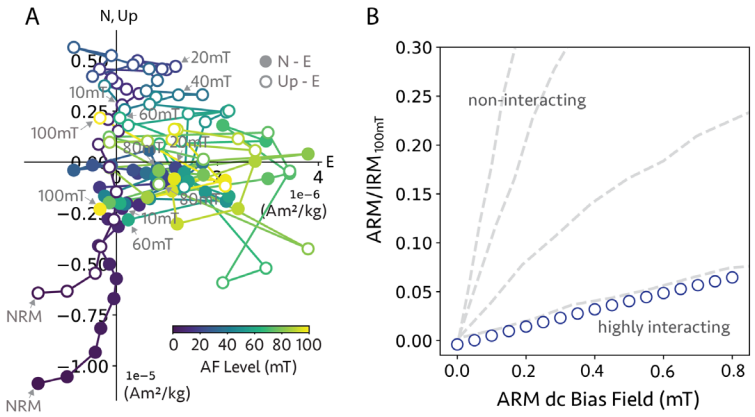

Fig. S-9. Magnetic results from the Hillsborough meteorite. **(A)** Vector-endpoint diagram showing AF demagnetization data. **(B)** ARM acquisition curve for the sample. From top to bottom, the gray dashed curves represent ARM acquisition curves for different reference materials: non-interacting single-domain magnetite, ultrasonic-treated magnetotactic bacteria, detergent-treated magnetotactic bacteria, and highly interacting chiton tooth magnetite (*61*).

Results: The NRM was 1.27×10^{-5} Am^2/kg. A low coercivity component was removed below applied fields of 10 mT, and the remanence was unstable at higher AF levels (Fig. S-9a). The absence of high coercivity remanence in the sample, coupled with a low NRM/sIRM ratio of 1.23×10^{-4} suggests that Hillsborough may have experienced aqueous alteration and formation of its dominant magnetic minerals, magnetite and pyrrhotite, in a paleofield with intensity <~400 nT, using the magnetite chemical remanent magnetization paleointensity calibration from (*62*). The low paleointensity could be due to aqueous alteration on the parent body post-dating the dissipation of the solar nebula field (*18*), or loss of primary magnetic mineral orientations during brecciation. The ARM to IRM ratio may be utilized to assess the degree of magnetostatic interactions within samples, with high and low ratios indicating weak and strong magnetostatic interactions, respectively (*61*). Our sample exhibits highly interacting behavior (Fig. S-9b), consistent with the observation of magnetite plaquettes and framboids and aggregates of pyrrhotite in electron microscopy.

Reflectance spectroscopy

By: Takahiro Hiroi

Methods: Chip and powder (ground and dry-sieved to <125 and 125-500 μm fractions) samples of Hillsborough meteorite were loaded onto black Teflon-coated dishes of 4 mm in diameter, and their reflectance spectra were measured at RELAB. Bidirectional visible and near-infrared (VNIR) reflectance spectra were measured at 30° incidence and 0° emergence angles over the wavelength range of 0.3-2.6 μm with Spectralon as the standard. The samples and standard were spun at a speed of 1.5 rotation per second. The field of view was about 2.8 mm. Biconical FTIR reflectance spectra were measured over the wavelength range of 0.8-100 μm with diffuse gold as the standard using a PIKE AutoDiff accessory attached to a Thermo Nexus 870 spectrometer. The FTIR spectra were scaled and connected to the VNIR spectra at 2.5 μm to improve their reflectance accuracy. The VNIR spectra were compared with other CM chondrite spectra, and the 3-μm hydration band spectra were fitted with a continuum and Gaussians to compare the 2.7-μm band position and shape with those of many other carbonaceous chondrites (*17, 63*).

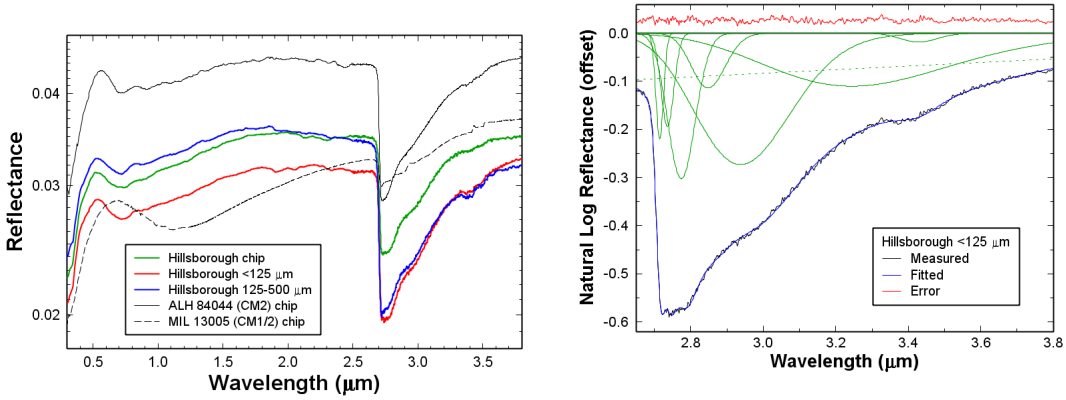

Fig. S-10 (A, left). VNIR-FTIR combined reflectance spectra of Hillsborough chip and powders along with those of other CM chondrite chips (*17, 63*). All the spectra of Hillsborough samples are highly consistent with one another and with typical CM2 chondrite spectra but dissimilar to the spectrum of this particular CM1/2 chondrite. **(B, right).** Gaussian fitting of the 3-μm hydration band of a Hillsborough spectrum shown as an example. A continuum background (linear to wavelength) is shown in a green broken line, and Gaussians (in wavenumber) are shown in green solid lines.

Results: As shown in Fig. S-10A, Hillsborough spectra are apparently consistent with those of typical CM2 chondrites. In addition, Gaussian fitting of the samples (Fig. S-10B) reveals that its 2.7-μm OH absorption band position and shape are consistent with those of CM1-2 chondrites. Therefore, Hillsborough meteorite is spectrally CM2 type.

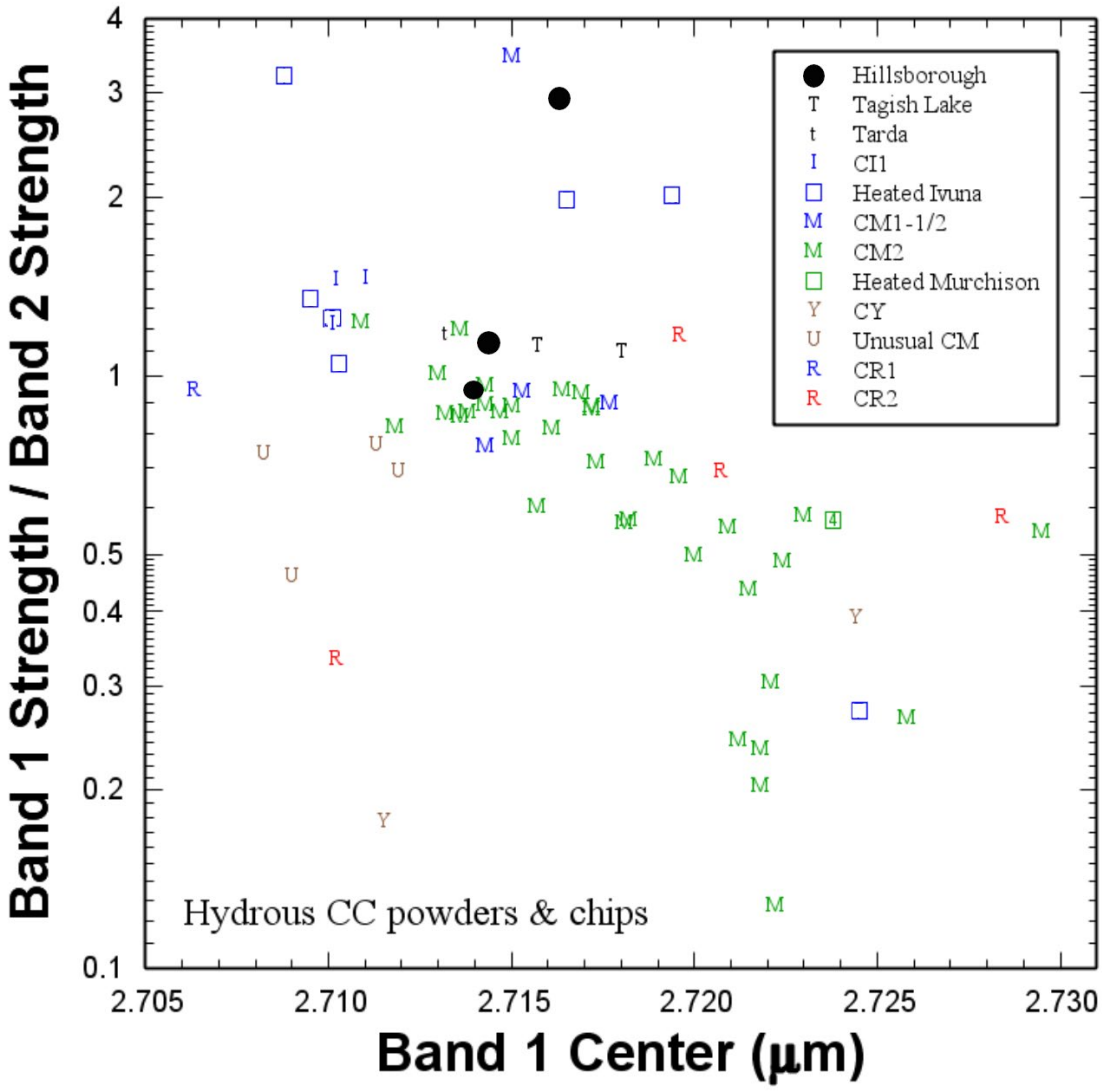

1066

1067 **Fig. S-11.** A plot of 2.7-µm band position and shape of the Hillsborough meteorite
1068 (•) in comparison with other carbonaceous chondrites (*17, 63*).

1069

Oxygen isotopes

By: Karen Ziegler

Methods: The oxygen isotopes of six fragments were analyzed at the University of New Mexico by laser fluorination. Sample weights for each measurement were between 3.8 and 7.4 mg. Each sample was compared 20 times to a standard.

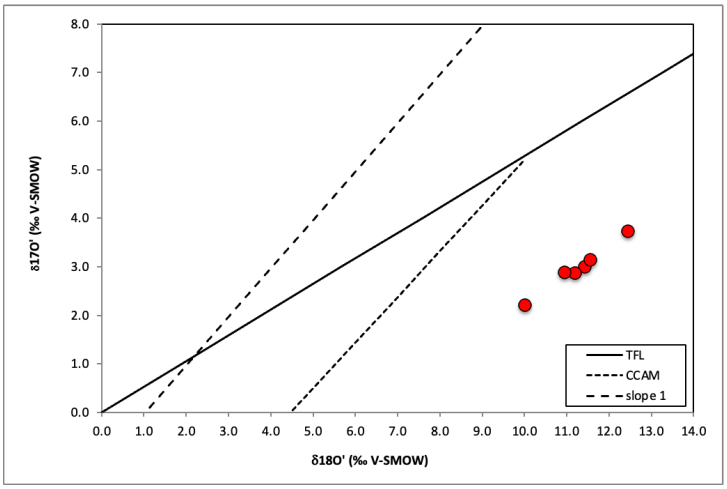

Fig. S-12. Oxygen isotope values for Hillsborough (red points) in a diagram with the Terrestrial Fraction Line (TFL), Carbonaceous Chondrite Anhydrous Mineral (CCAM) line, and a "slope 1" displaced from the CCAM line.

Results: The results (Table S-2, Fig. S-12) all lie within the CM carbonaceous chondrite field (*15*). The range was $\delta^{18}O$ = 10.010 to 12.453 ‰, $\delta^{17}O$ = 2.205 to 3.730 ‰, and $\Delta^{17}O$ = -3.081 to -2.845 ‰, respectively. The average values are $\delta^{18}O$ = 11.265 ‰, $\delta^{17}O$ = 2.973 ‰, and $\Delta^{17}O$ = -2.975 ‰ (linearized with Terrestrial Fractionation Line slope = 0.528).

Table S-2. Oxygen isotopes.

ID	Mass (mg)	Date	$\delta^{17}O$ (‰)	$\delta^{18}O$ (‰)	$\Delta^{17}O$ (‰)	n	$\Delta^{17}O$ (‰)
1	4.60	20-Aug-24	3.002	11.429	-3.032	20	-2.941
2	5.30	20-Aug-24	3.730	12.453	-2.845	20	-2.746
3	3.80	20-Aug-24	2.875	11.192	-3.035	20	-2.945
4	4.70	20-Aug-24	3.139	11.564	-2.967	20	-2.874
5	4.90	21-Aug-24	2.205	10.010	-3.081	20	-3.000
6	7.40	21-Aug-24	2.887	10.944	-2.892	20	-2.804

Elemental abundances and isotopes of C, N, and S

By: Nanako O. Ogawa, Yoshinori Takano, Naohiko Ohkouchi

Methods: In the Biogeochemistry Research Center, stable isotope ratio mass spectrometry (IRMS) was used to measure the stable isotope ratios and the relative abundances of C, N, and S (*64*). An ~10 mg of the Hillsborough sample was powdered and homogenized in an agate mortar and pestle prior to analysis. ~ 1 mg of the powdered sample was analyzed using a sensitivity-modified Thermo Finnigan Flash EA1112 Elemental Analyzer coupled to a Delta Plus XP isotope ratio mass spectrometer via a ConFlo III interface (nano-EA/IRMS) (*65*), to quantify carbon and nitrogen contents and their isotope values ($\delta^{13}C$, $\delta^{15}N$). Sulfur content and $\delta^{34}S$ values were analyzed using a separate nano-EA/IRMS system consisting of a modified Flash2000 Elemental Analyzer, a Shimadzu GC-2010 plus gas chromatograph, a ConFlo III interface, and a Delta Plus XP IRMS (*64*). For carbon and nitrogen analysis, 0.3–1 mg of sample was wrapped in a pre-cleaned, smooth-wall tin capsule and introduced into the EA (*66*), whereas for sulfur analysis, 0.02–0.1 mg of sample was wrapped in a tin foil capsule. For calibration of $\delta^{13}C$ and $\delta^{15}N$ values, five interlaboratory-calibrated amino acid standards (*67*) were analyzed alongside the samples. Three international silver sulfide standards were used for $\delta^{34}S$ calibration. Details of these standards are provided in Table S-3A, along with the analytical errors estimated by repeated analysis of BG-T ($\delta^{13}C$, $\delta^{15}N$) and IAEA-S-1 ($\delta^{34}S$).

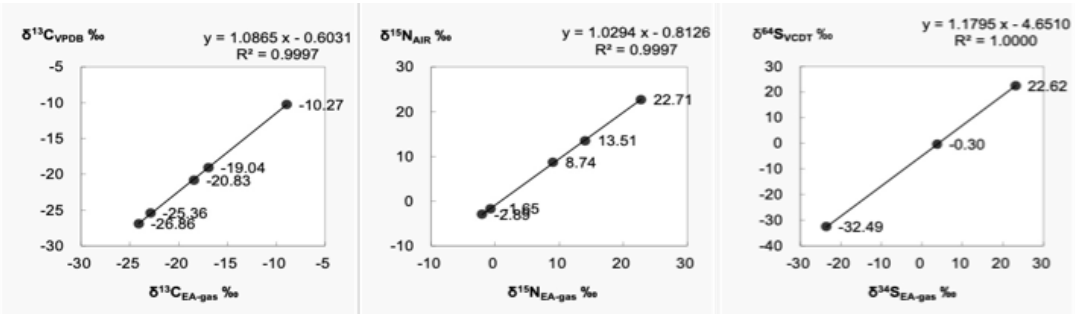

Fig. S-13. Calibration.

Table S-3A. C, N and S isotope standards.

ID	Material	$\delta^{13}C$ (‰ vs VPDB)	$\delta^{15}N$ (‰ vs Air)	$\delta^{34}S$ (‰ vs VCDT)	Reference
CERKU-01	DL-Alanine	-25.36 ± 0.08	-2.85 ± 0.04	-.-	(67)
CERKU-02	L-Alanine	-19.04 ± 0.04	22.71 ± 0.06	-.-	(67)
BG-T	L-Tyrosine	-20.83 ± 0.10	8.74 ± 0.09	-.-	(67)
BG-A	L-Alanine	-26.86 ± 0.04	-1.65 ± 0.06	-.-	(67)
BG-P	L-Proline	-10.27 ± 0.04	13.51 ± 0.02	-.-	(67)
IAEA-S-1	Silver Sulfide	-.-	-.-	-0.30 ± 0.03	IAEA
IAEA-S-2	Silver Sulfide	-.-	-.-	22.62 ± 0.08	IAEA
IAEA-S-3	Silver Sulfide	-.-	-.-	-32.49 ± 0.08	IAEA
Analytical error*	-.-	±0.19 (n=13)	±0.24 (n=12)	±0.74 (n=10)	

*Estimated by repeated analysis of BG-T ($\delta^{13}C$, $\delta^{15}N$) and IAEA-S-1 ($\delta^{34}S$)

Table S-3B. C, N and S isotopes and elemental abundances.

Run	Mass (mg)	C (wt.%)	N (wt.%)	S (wt.%)	$\delta^{13}C$ (‰ vs VPDB)	$\delta^{15}N$ (‰ vs Air)	$\delta^{34}S$ (‰ vs VCDT)
NC-1	0.300	1.70	0.070	-.-	-0.4	+27.8	-.-
NC-2	0.911	1.81	0.075	-.-	+0.1	+28.5	-.-
NC-3	0.954	1.76	0.075	-.-	+0.2	+30.0	-.-
NC-4	0.924	1.77	0.076	-.-	-0.5	+27.7	-.-
S-1	0.013	-.-	-.-	n.d.	-.-	-.-	-1.8
S-2	0.025	-.-	-.-	n.d.	-.-	-.-	-0.3
S-3	0.021	-.-	-.-	n.d.	-.-	-.-	-1.5
S-4	0.107	-.-	-.-	5.94	-.-	-.-	-0.3
S-5	0.109	-.-	-.-	6.09	-.-	-.-	-0.9
S-6	0.112	-.-	-.-	6.37	-.-	-.-	-1.0
Mean		1.76 ± 0.05	0.074 ± 0.030	6.13 ± 0.22	-0.2 ± 0.4	+28.5 ± 1.1	-1.0 ± 0.6

Table S-3B (cont.). C, N and S isotopes and elemental abundances.

Run	Mass Ratio C/N	Mass Ratio N/C	Mass Ratio S/C	Mass Ratio C/S	Date
NC-1	24.29	0.041	-.-	-.-	18-Nov-24
NC-2	24.13	0.041	-.-	-.-	18-Nov 24
NC-3	23.47	0.043	-.-	-.-	18-Nov 24
NC-4	23.29	0.043	-.-	-.-	18-Nov-24
S-1	-.-	-.-	-.-	-.-	29-Nov-24
S-2	-.-	-.-	-.-	-.-	29-Nov-24
S-3	-.-	-.-	-.-	-.-	29-Nov-24
S-4	-.-	-.-	-.-	-.-	29-Nov-24
S-5	-.-	-.-	-.-	-.-	29-Nov-24
S-6	-.-	-.-	-.-	-.-	29-Nov-24
Mean	**23.79 ± 0.49**	**0.042 ± 0.001**	**3.48 ± 0.15**	**0.29 ± 0.013**	

Bulk elemental abundances of H, C, N, and S

By: Queenie H. S. Chan, James Brakeley, Bianka Munday

Methods: ~900 mg of Hillsborough sample was powdered and homogenised in a ceramic mortar and pestle inside a laminar flow hood under HEPA-filtered positive pressure (equivalent to ISO Class 4–5). The powdered sample was stored in a N2 purged desiccator for 2 weeks to minimize the amount of absorbed atmospheric water that the samples may contain (mass loss was ~1.5 wt.%). ~11 mg of the powdered Hillsborough sample was analysed with an Elementar vario MICRO cube to quantify C,H,N,S contents. Samples were introduced directly from a sample carousel into the EA where they were combusted at 1150 °C in a combustion tube containing WO_3, and reduced at 850 °C in a reduction tube containing copper granules. The N_2, CO_2, H_2O and SO_2 gases were analysed by a thermal conductivity detector. 0.25–5 mg of sulphanilamide ($C_6H_8N_2O_2S$; C = 41.85 wt.%; H = 4.68 wt.%; N =16.27 wt.%; S = 18.62 wt.%), purchased from Elemental Microanalysis, was used as a calibration standard, which was used to normalize and correct the data at regular intervals (i.e., every 10 samples). Acetanilide (C_8H_9NO; C = 71.09 wt.%; H = 6.71 wt.%; N =10.36 wt.% purchased from Sigma-Aldrich), and several terrestrial soil samples with various CHNS abundances (C = 3.26–8.98 wt.%; Organic C = 0.24–7.04 wt.%; N =0–0.43 wt.%; S = 0.11–3.85 wt.%) were used as in house standards to monitor the accuracy and precision of the measured elemental compositions throughout the runs (i.e. 1 standard every 20 samples), and the absolute standard deviations for the CHNS analyses determined by a triplicate analysis of the reference standard were 0.03% for C, 0.051% for H, 0.04% for N and 0.278% for S. The C, N and S abundances typically vary by 0.04–0.2 wt.% from their reference values. Blanks (air) were run between every sample to reduce memory effect that may arise in the adsorption column of the EA. Each run takes about 10 minutes, and the entire batch of analyses was completed within a day.

Table S-4. Compilation of bulk elemental abundances.

	H (wt%)	N (wt%)	C (wt%)	S (wt%)	Ref.
Hillsborough (0.011g)	1.292 ± 0.018	0.100 ± 0.015	1.940 ± 0.035	3.076 ± 0.340	This study
Hillsborough (0.010g)	-.-	0.074 ± 0.030	1.76 ± 0.05	6.13 ± 0.22	Table S-3A
Hillsborough (0.055g)	-.-	-.-	-.-	3.5 ± 0.1	Table S-5
Murchison (CM2)	1.135 ± 0.057	0.104 ± 0.003	1.980 ± 0.030	3.40 ± 0.14	*(68,30)*
Orgueil (CI1)	1.564 ± 0.019	0.208	3.92	5.52 ± 0.13	*(68,3)*

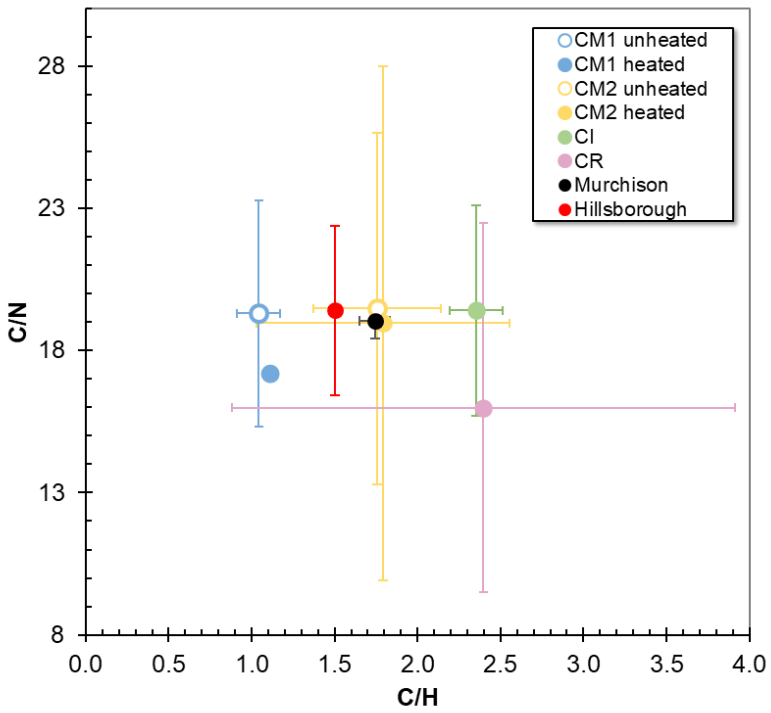

Fig. S-14. C/H versus C/N ratios of bulk Hillsborough (this study) compared to other carbonaceous chondrites (data from *68,3*).

Cosmogenic radionuclides.

By: Kees C. Welten, Kunihiko Nishiizumi, Marc W. Caffee

Methods: We dissolved two aliquots (of 5.10 and 50.04 mg) of the Hillsborough meteorite for cosmogenic radionuclide analysis. The samples were dissolved in a 3:1 mixture of HF/HNO_3 in the presence of Be (0.61-0.63 mg) and Cl (3.4-3.5 mg) carriers by heating the samples in Parr Teflon digestion bombs for 20-24 hrs. at 125-140 ºC. After cooling off the samples to room temperature we separated Cl as AgCl (for cosmogenic ^{36}Cl analysis) and took a small aliquot of the dissolved sample for chemical analysis by ICP-OES (Table S-5). Be and Al were separated using ion exchange chromatography and acetyl-acetone solvent extraction procedures described previously (e.g., *69*). The Be and Al fractions were purified, converted to BeO and Al_2O_3 and mixed with Nb powder before being loaded into a stainless-steel cathode. The $^{10}Be/Be$ and $^{26}Al/Al$ ratios were measured by accelerator mass spectrometry at Purdue University (*70*). Results of the two samples are shown in Table S-5; the ^{26}Al AMS measurement of the larger sample is in progress. Assuming expected ^{10}Be and ^{26}Al production rates in CM chondrites of ~22 and ~42 dpm/kg, respectively, for an object with a radius of ~20 cm the measured ^{10}Be and ^{26}Al concentrations in the Hillsborough CM chondrite indicate a 4π CRE age (as a small object in space) of 0.23 ± 0.02 Myr, overlapping with one of the main CRE age clusters of 0.2 Myr for CM chondrites (*18*). With this short CRE age, the ^{36}Cl concentration has reached only ~40% of the saturation value, so the measured ^{36}Cl concentration of ~9 dpm/kg corresponds to a ^{36}Cl production rate of ~22 dpm/kg. This value is much higher than the value of ~8 dpm/kg expected from spallation reactions on K, Ca, Fe and Ni, indicating that the Hillsborough meteorite contains a significant contribution of neutron-capture produced ^{36}Cl, which is consistent with observations in many other CM chondrites.

Table S-5. Concentrations of major elements (measured by ICP-OES) and of cosmogenic ^{10}Be, ^{26}Al and ^{36}Cl (measured by AMS) in two aliquots (5.10 mg and 50.04 mg) of Hillsborough CM chondrite.

Element	**5.10 mg**	**50.04 mg**
Mg (%)	11.4	11.5
Al (%)	1.09	1.13
P (%)	0.11	0.12
S (%)	3.4	3.6
K (ppm)	566	480
Ca (%)	1.67	1.26
Ti (ppm)	618	584
Mn (%)	0.18	0.17
Fe (%)	20.7	20.6
Co (ppm)	587	562
Ni (%)	1.25	1.22
Nuclide		
^{10}Be [dpm/kg]	2.58 ± 0.05	2.53 ± 0.04
^{26}Al [dpm/kg]	8.36 ± 0.23	-
^{36}Cl [dpm/kg]	10.4 ± 0.5	8.77 ± 0.16

Noble gases

By: Henner Busemann, Daniela Krietsch, Colin Maden

Methods: We measured all noble gas isotopes of He to Xe in a sample of 18.247 ± 0.015 mg. The gases were released by melting the sample at ~1700 °C in one step in a Mo crucible. A re-extraction at slightly higher temperature demonstrated the completeness of the extraction in the main step (the re-extraction contained <0.2% of the totally released ^{4}He, ^{20}Ne, ^{36}Ar, ^{84}Kr and ^{132}Xe, respectively). Blank corrections amounted to ≤0.5% of the measured concentrations for all isotopes, except for ^{40}Ar (12%). Details of gas cleaning, separation, instrumentation and component decomposition are given in (*19, 71, 72*).

Results: The light noble gases are dominated by a large contribution of solar wind (SW). The concentrations of ^{4}He and, particularly, ^{20}Ne are among the highest observed in CM chondrites (cf. *19*, and references given therein). This implies a comparatively long exposure of some of the examined Hillsborough material in the upper regolith layers of its parent body - or an unusual high fraction of SW-bearing grains in our sample. This is also reflected in the ^{3}He/^{4}He and ^{20}Ne/^{22}Ne ratios (Table S-6a) that almost reach the ratios measured in pure SW as, e.g., returned by the Genesis mission (*20*). Hillsborough is, thus, a regolith breccia, consistent with its comminuted character.

A comparatively long presence of the examined material at the surface of the parent asteroid also implies that some near-surface "pre-exposure" of the material on the parent body, in addition to the exposure to cosmic rays during its transfer through space (so-called "complex exposure history") cannot be excluded. This could include both exposure to galactic cosmic rays (GCRs, detectable in the upper few m within a regolith) and solar cosmic rays (SCRs, within the upper few cm). Due to the abundant SW presence, the $(^{21}Ne/^{22}Ne)_{cos}$ ratio cannot be used as a shielding indicator nor to detect possible SCR-derived Ne_{cos}.

Using the pre-atmospheric mass of Hillsborough of 53±6 kg, the density of 1.89±0.01 g/cm^3 (both this work), and assuming a spherical shape, its pre-atmospheric radius would have been 18.1-19.6 cm. Next to the bulk chemistry taken from this work (Tables S-3, S-4, S-5) and for Si and O from (*73*), the radius is one of the two geometric shielding parameters used in the (*74*) model to calculate potential cosmogenic noble gas production rates. To include a potential non-spherical shape, we chose pre-atmospheric radii of 10, 20 and 25 cm as input. We furthermore restricted possible shielding depths of our sample to 78 % of these radii, i.e. 8, 16 and 20 cm. The probability that our sample originates from the other, inner 22 % of the sphere is less than 1 % of the total volume (*75*). However, this did not change the determination of the production rate range given below.

Combining all information (radius, depth, chemistry), the production rate P_{21} for $^{21}Ne_{cos}$ is in the range 0.1199 and 0.2256 cm^3 STP ^{21}Ne / (g × Ma). The resulting nominal 4π (i.e., in space) total GCR exposure age would be 2.2 to 5.7 Ma. As

discussed, additional exposure on the parent body cannot be excluded. If this pre-exposure occurred in the past (i.e., > 10 half lives of ^{10}Be and ^{26}Al before ejection), it will not be monitored by these radionuclides anymore, while the noble gases were accumulated during both irradiation periods. The transfer time in space will then be given by the radionuclides.

The ^{36}Ar, ^{84}Kr, and ^{132}Xe concentrations as well as the ^{36}Ar/^{132}Xe and ^{84}Kr/^{132}Xe ratios are in the typical range observed in moderately to strongly aqueously altered CM chondrites that have lost most of their "Ar-rich" noble gas component that is susceptible to aqueous alteration (*19*), which agrees with Hillsborough's classification as CM1/2 chondrite. The Xe isotopic composition can be explained by Q-Xe with a minor addition of ~2 % of Xe-HL (based on ^{132}Xe), some excess ^{129}Xe from the decay of short lived ^{129}I and probably some SW-Xe only visible in ^{124,126}Xe. Similarly, Kr is isotopically similar to Q-Kr with a minor addition of SW-Kr.

Table S-6A. Helium and Ne concentrations (in 10^{-8} cm^3 STP/g) and isotopic ratios.

Sample	^{4}He	^{3}He/^{4}He x 10^{4}	^{20}Ne	^{21}Ne$_{cosm}$	^{20}Ne/^{22}Ne	^{21}Ne/^{22}Ne
Hillsborough	104430	4.074	1579	0.58	13.40	0.03695
	± 700	± 0.034	± 40	± 0.10	± 0.33	± 0.00009

Table S-6B. Argon concentrations (in 10^{-8} cm^3 STP/g) and isotopic ratios.

Sample	^{36}Ar	^{36}Ar/^{38}Ar	^{40}Ar/^{36}Ar
Hillsborough	124.6	5.188	7.22
	± 2.1	± 0.018	± 0.15

Table S-6C. Krypton concentrations (in 10^{-10} cm^3 STP/g) and isotopic ratios.

Sample	^{84}Kr	^{78}Kr/^{84}Kr	^{80}Kr/^{84}Kr	^{82}Kr/^{84}Kr	^{83}Kr/^{84}Kr	^{86}Kr/^{84}Kr
		^{84}Kr = 100				
Hillsborough	83.96	0.603	3.933	19.96	20.02	30.76
	± 0.69	± 0.009	± 0.021	± 0.08	± 0.08	± 0.12

Table S-6D. Xenon concentrations (in 10^{-10} cm^3 STP/g) and isotopic ratios.

Sample	^{132}Xe	^{124}Xe/^{132}Xe	^{126}Xe/^{132}Xe	^{128}Xe/^{132}Xe	^{129}Xe/^{132}Xe	^{130}Xe/^{132}Xe	^{131}Xe/^{132}Xe	^{134}Xe/^{132}Xe	^{136}Xe/^{132}Xe
		^{132}Xe = 100							
Hillsborough	98.48	0.4707	0.4111	8.273	107.23	16.062	82.08	38.00	32.08
	±0.51	±0.0056	±0.0035	±0.047	±0.43	±0.061	±0.28	±0.15	±0.13

Titanium isotopes

By: Greg Brennecka and Jan H. Render

Methods: Titanium was purified using a two-stage ion-exchange chromatography procedure following the methods outlined in (*73*). After dissolution, the sample solution was converted into 2 mL 12M HNO_3 and loaded onto DGA resin cartridges in combination with a vacuum box from Eichrom®. After loading, most elements were eluted with 12mL 12M HNO_3 before Ti was collected with 12 mL 6M HNO_3. The cut containing Ti was then converted into 2 mL 0.4M HCl – 1M HF and was further purified using 2 mL precleaned and preconditioned Biorad AG-1X8 (100 to 200 mesh) anion exchange resin in Biorad polyprep columns. Remaining Ca, V, and other impurities were eluted with an additional 6 mL 0.4M HCl – 1M HF before Ti was collected with 8 mL 6M HCl. The Ti cuts were dried down and converted into 2% HNO_3 – 0.005M HF for MC-ICPMS measurements. Yields of this entire procedure were >90% and procedural blanks are typically ~2ng, which is negligible compared to ~7µg of Ti that was processed for Hillsborough. To assess the accuracy of our methods, we also processed USGS rock standard BCR-2 alongside Hillsborough, for which $\varepsilon^{46}Ti = -0.02 \pm 0.08$, $\varepsilon^{48}Ti = 0.01 \pm 0.03$, $\varepsilon^{50}Ti = -0.06 \pm 0.10$ was measured, values that are consistent with previously reported data for this standard (e.g., *73*).

Isotopic measurements of Ti were performed at LLNL using a ThermoScientific Neoma MC-ICPMS in combination with a Cetac Aridus II desolvating introduction system and a ~50 µL/min Savillex PFA nebulizer. Since certain isotope masses of Ti are affected by isobaric interferences from polyatomic species (e.g., $^{36}Ar^{14}N$), the isotope measurements were performed in medium resolution mode on the flat low-mass shoulder plateaus of the peak to resolve and avoid these interferences. Using a Jet and X cone setup, this setup yielded ~35 V on ^{48}Ti with 250 ng/g solutions. Atomic masses 43 to 53 were acquired with a single cup configuration, including all Ti isotopes, as well ^{43}Ca, ^{44}Ca, ^{51}V, ^{52}Cr, ^{53}Cr to monitor and correct isobaric interferences from ^{46}Ca, ^{48}Ca, ^{50}V, and ^{50}Cr. All signals were collected with Faraday cups connected to 10^{11} Ohm amplifiers. Measurements consisted of 50 cycles of 8 seconds integration time. To account for instrumental mass fractionation, samples were bracketed with the OL-Ti reference standard. Isotope data are reported in the epsilon notation, as relative deviations in parts per ten thousand from the OL-Ti bracketing standard:

$$\varepsilon^{i}Ti = \left(\frac{^{i}Ti/^{47}Ti}{^{i}Ti/^{47}Ti} - 1\right) \times 10{,}000 \quad (2)$$

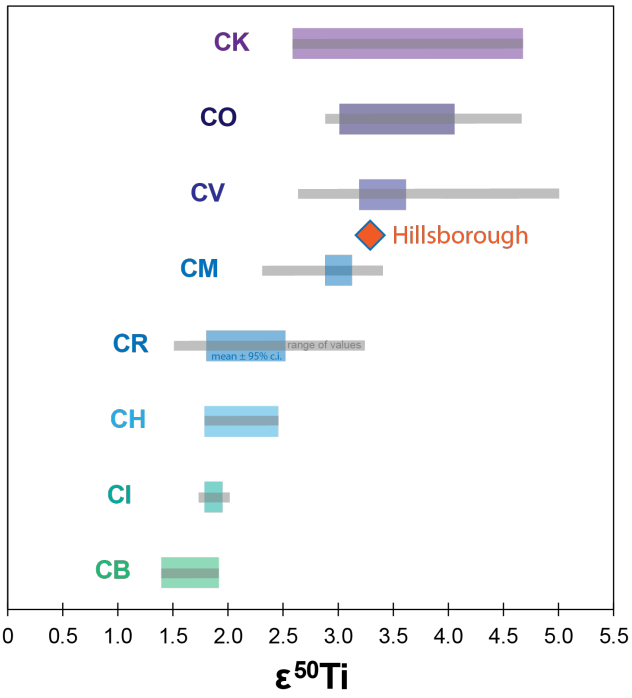

Fig. S-15. Titanium isotopic composition of Hillsborough in relation to those of carbonaceous chondrite types. Literature data shown was compiled in (*16*), where the colored boxes represent the average with a 95% confidence interval, and the gray bars represent the range of data in each meteorite group. Where sample sizes are small (e.g., CK, CH, CB), the most conservative uncertainties are shown. Chemical separation and measurement methods follow (*73*) with the modification of 8 s integrations as opposed to 4 s integrations.

Table S-7. Titanium isotopes for Hillsborough.

	ε^{46}Ti	ε^{48}Ti	ε^{50}Ti
Hillsborough.1	0.60	0.00	3.21
Hillsborough.2	0.50	-0.06	3.29
Hillsborough.3	0.63	0.06	3.40
Hillsborough.4	0.55	-0.07	3.38
Hillsborough.5	0.64	-0.04	3.16
Hillsborough.6	0.59	0.00	3.33
AVG	0.59	-0.02	3.30
2SD	*±0.11*	*±0.10*	*±0.19*
2SE	*±0.04*	*±0.04*	*±0.08*

Methanol-soluble and insoluble organic compounds

By: Stefan Ruchti, Philippe Schmitt-Kopplin, Jasmine Hertzog, Vincent Carré

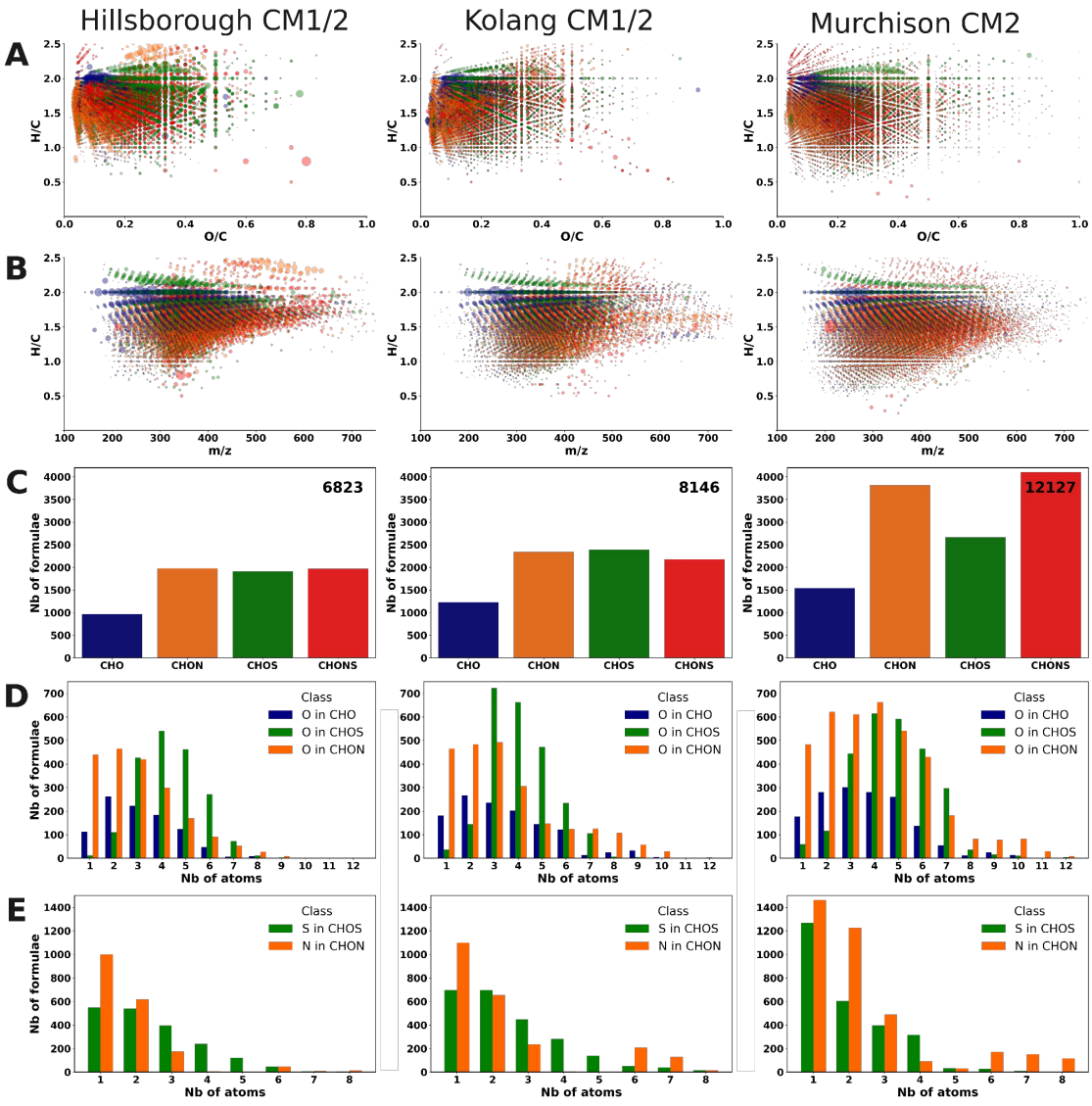

Fig. S-16. Data evaluation of the ESI(-) FT-ICR MS spectra of Hillsborough CM1/2 compared to Kolang CM1/2 and Murchison CM2 showing all CHO, CHNO, CHOS, and CHNOS chemical families with **(A)** classical van Krevelen diagrams **(B)** mass derived van Krevelen, **(C)** distributions of the chemical formula abundances of the various chemical families, **(D)** distribution of the formulas as a function of their abundance in oxygen and **(E)** distribution of the formulas a function of their abundance in nitrogen and sulfur. The bubble size in (A) and (B) is proportional to peak intensity of the mass spectrum and the color legend is reflected in (C).

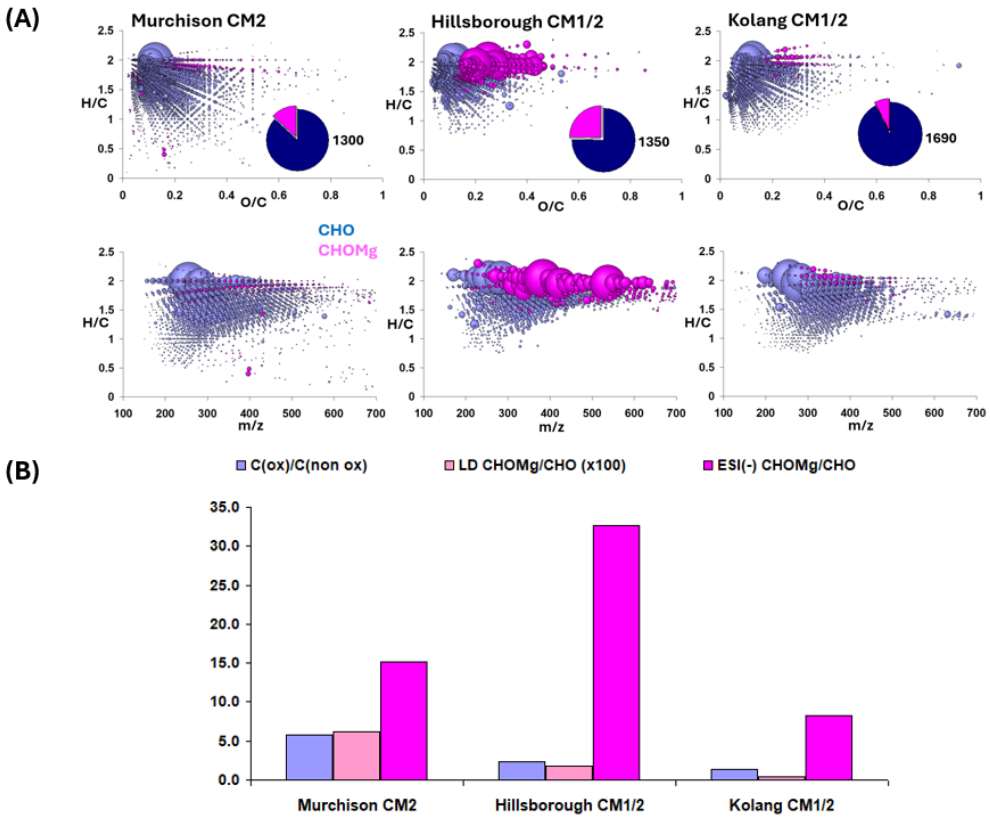

Fig. S-17. (A) Data evaluation from the ESI(-)-FT-ICR MS spectra of Hillsborough CM1/2 compared to Kolang CM1/2 and Murchison CM2 showing all CHO and CHOMg (*76*) chemical families with the classical van Krevelen diagrams and the mass-derived van Krevelen. The bubble size is proportional to peak intensity of the mass spectrum. **(B)** Ratio of oxygenated to non-oxygenated species from LDI(+)-FT-ICR MS in line with the CHOMg/CHO abundance ratios of the three meteorites from LDI(+)-FT-ICR MS and ESI(-)-FT-ICR MS.

Methods: For laser desorption ionization (LDI) FT-ICR MS in positive mode the raw meteorite samples were deposited on a stainless-steel target. A 355-nm wavelength laser with a spot diameter of 50 µm and 2000 Hz frequency was used. Ions generated by 100 laser shots were stored in a hexapole for 0.05 seconds before being transferred into the ICR cell. Laser power was adjusted for each sample to detect MS signals while limiting fragmentation and recombination phenomena. Ion source as well as instrument parameters were optimized via software *ftmsControl* (V2.3.0, Bruker Daltonics, Bremen, Germany). Prior to acquisition the mass spectrometer was externally calibrated, and the ICR detection cell was shimmed and gated using red phosphorus deposited on the MALDI plate. Mass spectra resulted from accumulation of 200 scans over a *m*/*z* range of 107.5 – 1500 and with a 8 megaword time-domain. At *m*/*z* 400, a mass resolution of 600 000 was achieved.

Electrospray ionization in negative mode (ESI (-) FT-ICR MS) was performed with soluble organic matter methanol extract in a standardized way as described in (*77*).

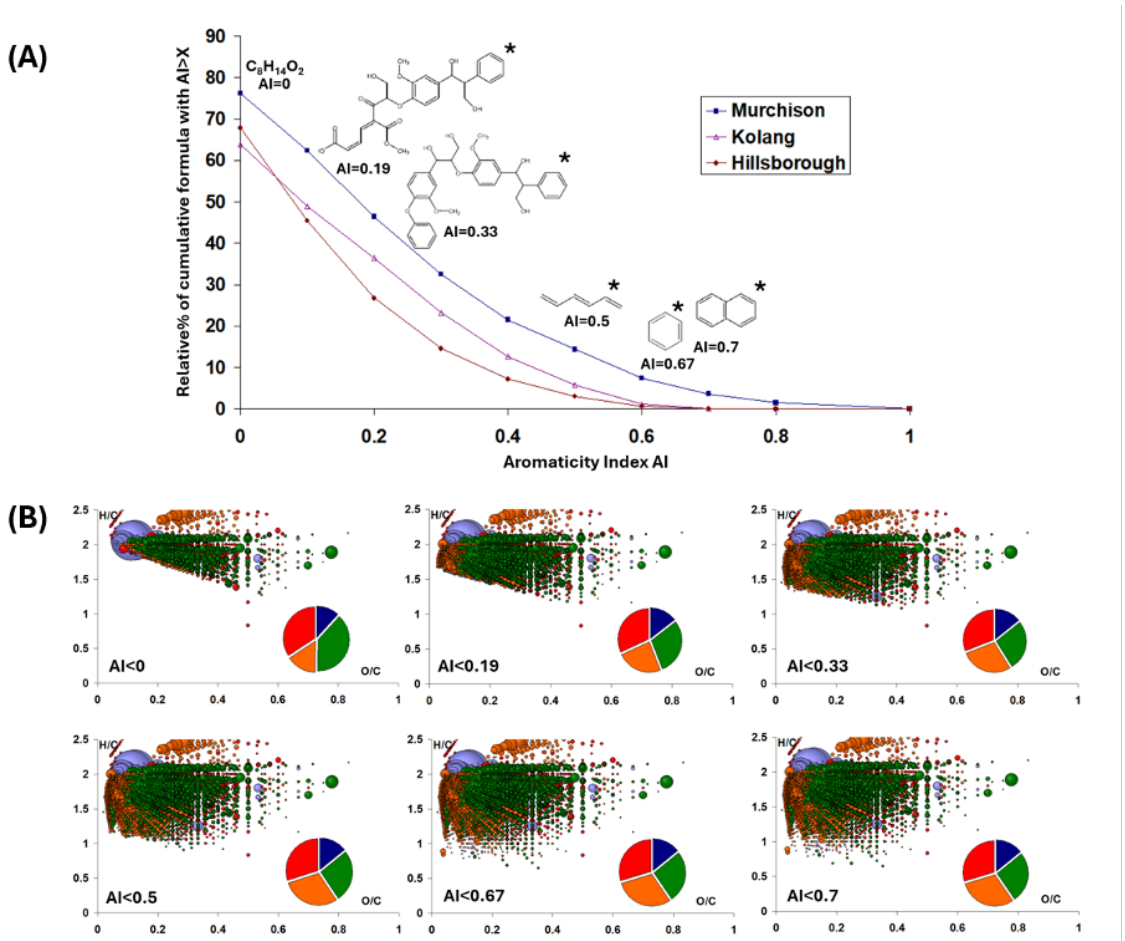

S-18. (A) Aromaticity index (AI) represented as a relative percent of cumulative AI (AI>x). AI was calculated for each annotated chemical formula following the equation: AI = (1+C-O-S-0.5H)/(C-O-S-N-P), where the letters specify the index of an element in the molecular sum formula (*36*). Example chemical structures are shown. **(B)** Visualization of the various regions in the van Krevelen of Hillsborough, corresponding to AI lower than selected values (AI<X; values were selected from the examples in (A)). Pie charts show the count of features assigned to chemical families as in previous figures (Blue: CHO, Orange: CHON, Green: CHOS, Red: CHONS).

Amino acids

By: Hannah L. McLain, Daniel P. Glavin, Jason P. Dworkin

Methods: Standards and reagents. All glassware, ceramics, and sample handling tools were rinsed with Milli-Q ultrapure water (18.2 MΩ·cm, < 3 ppb total organic carbon), wrapped in aluminum foil, and heater in a furnace at 500 °C in air overnight. Most of the chemicals and reagents were purchased from Sigma-Aldrich. A stock amino acid solution was prepared by mixing individual amino acid standards (97-99 % purity) in Milli-Q ultrapure water. All chiral amino acid standards were purchased as racemic mixtures (where the D amino acid concentration is equal to the L amino acid concentration) except for the D-threonine (Sigma-Aldrich), L-threonine (Sigma-Aldrich), D-isovaline (Acros Organics), and L-isovaline (Acros Organics) which were prepared as racemic mixtures by mixing the appropriate masses of each standard in Milli-Q ultrapure water to the standard mixture. Acid vapor hydrolysis used Tamapure-AA-10-HCL 20 % (metallic impurity < 10 pg/mL). Cation-exchange resin (AG50W-X8, 100-200 mesh, hydrogen from, BIO-RAD) was used for the removal of salts and interfering ions from the samples. During the desalting protocol, 1.5 N HCl, 2 M NaOH, and 2 M NH_4OH were used. The 2 M NaOH was prepared by dissolving 32 g of NaOH pellets (Sigma-Aldrich) in 400 mL Milli-Q ultrapure water, the 1.5 N HCl was prepared from diluting the Tamapure HCl, the 2 M NH_4OH was prepared in vacuo using Milli-Q ultrapure water and ammonia gas (Air Products).

Sample extraction. The Hillsborough meteorite (81.9 mg), Murchison meteorite (82.3 mg), and fused silica FS-120 (109.8 mg), and procedural blank samples were flame-sealed in glass ampoules in 1 mL of Milli-Q ultrapure water and then heated at 100 °C for 24 h. After heating, the ampoules were opened and centrifuged at 3000 rpm for three minutes, the water supernatants were then transferred from the ampoules by pipetting into pre-weighed amber glass vials. Another 1 mL of Milli-Q ultrapure water was added to each glass ampoule, the ampoules were re-centrifuged, and the supernatant was transferred to the sample amber glass vials (this process was repeated one final time to maximize the recovery of the water extracts). After extraction, 45 % of the supernatant was dried down under vacuum and subsequently subjected to 6 M HCl vapor hydrolysis at 150 °C for 3 h. The HCl acid-hydrolyzed and 45 % of the non-acid vaporized supernatant were desalted using AG50W-X*, 100-200 mesh, hydrogen form, BIO-RAD cation exchange resin. Both the vapor hydrolyzed (45 %) and non-vapor hydrolyzed (45 %) supernatant sample sets were eluted from the cation exchange desalting columns using 7 mL of 2 M NH_4OH. After desalting, the eluent was dried under vacuum and brought up in 100 µL of Milli-Q ultrapure water. From this reconstituted sample, 20 µL was dried down with 20 µL of sodium borate buffer (pH = 9). After dry down, the samples were brought up in 20 µL of Milli-Q ultrapure water and 5 µL of 0.1 M OPA/NAC derivatization agent and allowed to react for 15 minutes at room temperature before quenching with 75 µL of 0.1 M hydrazine.

Table S-8. Blank-corrected abundances (nmol/g) of identified two- to six-carbon amino acids in the non-hydrolyzed (free) and 6M HCl acid-hydrolyzed (total) hot-water extracts of the Hillsborough and Murchison meteorites measured by LC-FD/Q-ToF-MS.

	Hillsborough (CM1/2)		Murchison (CM2)	
	Free (nmol g^{-1})	Total (nmol g^{-1})	Free (nmol g^{-1})	Total (nmol g^{-1})
Acidic amino acids				
D-Aspartic acid	0.08 ± 0.01	0.360 ± 0.007	0.37 ± 0.01	1.50 ± 0.06
L-Aspartic acid	0.14 ± 0.01	1.60 ± 0.01	0.58 ± 0.01	5.28 ± 0.20
D-Glutamic acid	0.080 ± 0.006	0.40 ± 0.04	0.32 ± 0.02	2.17 ± 0.04
L-Glutamic acid	0.11 ± 0.01	2.45 ± 0.02	0.53 ± 0.01	10.24 ± 0.11
Hydroxy amino acids				
D-Serine	0.020 ± 0.001	0.160 ± 0.009	0.140 ± 0.005	0.310 ± 0.003
L-Serine	0.16 ± 0.01	3.22 ± 0.10	0.39 ± 0.02	7.54 ± 0.13
C2 amino acid				
Glycine	0.57 ± 0.03	23.25 ± 1.37	3.01 ± 0.10	38.58 ± 0.16
C3 amino acids				
β-Alanine	0.11 ± 0.01	0.56 ± 0.02	2.39 ± 0.10	7.11 ± 0.13
D-Alanine	0.30 ± 0.01	1.08 ± 0.03	1.46 ± 0.05	3.70 ± 0.07
L-Alanine	0.32 ± 0.01	5.09 ± 0.22	1.41 ± 0.04	7.21 ± 0.20
C4 amino acids				
D,L-α-Amino-*n*-butyric acid	0.18 ± 0.01	0.31 ± 0.02	1.07 ± 0.03	1.55 ± 0.02
D-β-Amino-*n*-butyric acid	0.10 ± 0.01	0.15 ± 0.04	1.35 ± 0.05	2.47 ± 0.06
L-β-Amino-*n*-butyric acid	0.06 ± 0.06	0.22 ± 0.05	1.69 ± 0.13	1.91 ± 0.42
γ-Amino-*n*-butyric acid	0.18 ± 0.01	1.40 ± 0.01	1.51 ± 0.05	5.01 ± 0.19
α-Aminoisobutyric acid	0.31 ± 0.01	1.86 ± 0.06	2.60 ± 0.11	12.40 ± 0.42
C5 amino acids				
D-Valine	0.08 ± 0.01	0.08 ± 0.01	0.28 ± 0.01	0.500 ± 0.004
L-Valine	0.11 ± 0.02	1.22 ± 0.05	0.20 ± 0.01	4.64 ± 0.07
D,L-Isovaline	0.47 ± 0.04	0.91 ± 0.12	4.67 ± 0.15	9.23 ± 0.12
C6 amino acid				
ε-Amino-*n*-caproic acid	1.97 ± 0.11	22.50 ± 1.10	1.82 ± 0.30	1.06 ± 0.01
Sum C2-C6 amino acids	**4**	**66**	**23**	**118**

LC-FD/ToF-MS analyses. Amino acid abundances, distribution, and enantiomeric ratios were determined by LC-FD/ToF-MS. The amino acids in the NH_4OH eluates were derivatized with OPA/NAC for 15 minutes at room temperature followed by their separation and analysis using a Waters ACQUITY UPLC and Waters Xevo G2-XS Q-ToF-MS operating in positive ion mode. C2 to C6 amino acids were chromatographically resolved using a Waters BEH C18 column (2.1 × 50 mm, 1.7 μm bead) and a Waters BEH phenyl column (2.1 × 150 mm, 1.7 μm bead) in series. Both columns were maintained at 30.0°C. The mobile phase conditions for amino acid separations were as follows: flow rate, 150 μL/min; gradient, time in minutes (%B): 0 (0), 35 (55), 45 (100). C5 amino acid isomers and enantiomers were chromatographically separated using the same chromatography conditions as for the C2 to C6 amino acids but required the implementation of a different gradient. The gradient used for C5 amino acid isomers and enantiomers was structured via time in minutes (%B): 0 (15), 25 (20), 25.06 (35), 44.5 (40), 45 (100).

During the Xevo G2-XS analysis, a dual electrospray ionization (ESI) system was used for the purpose of implementing lock mass corrections. The primary ESI source was operated using the following parameters: capillary voltage, 3.0 kV; sampling cone voltage, 40 V; source temperature, 120°C; desolvation gas (N2) temperature, 350°C; cone gas (N_2) flow, 50 L h^{-1}, desolvation gas flow rate, 750 L h^{-1}. Due to the possibility that minor variations in the mass-to-charge (*m*/*z*) scale may occur while executing experimental runs after instrument calibration is performed, a reference ESI source was implemented to supply an independent leucine enkephalin standard signal. The reference ESI source was operated using a sample infusion rate of 20 µL min^{-1}, a sample fill volume of 250 µL, a lockspray infusion rate of 10 µL min^{-1}, a capillary voltage of 3.0 kV, a reference cone voltage of 30 V, and a collision energy of 6.0 V. The ToF analyzer was operated in "Sensitivity mode," which used a reflectron to provide a full width at half maximum resolution of <22,000 based on the [M+H]+ of leucine enkephalin, *m*/*z* 556.2771.

The amino acid abundances (Table S-8) and their enantiomeric ratios (Table S-9) in the meteorite extracts and controls were determined by comparison of the peak areas generated from the sample and control UV fluorescence chromatograms (LC-FD, λ_{ex} = 340 nm, λ_{em} = 450 nm) of their OPA/NAC derivatives to the corresponding peak areas of amino acid standards run under the same chromatographic conditions (Figure S-19) and included peak identification confirmation by accurate mass using a match tolerance of 10 ppm (Table S-10).

Table S-9. Summary of the D/L ratios and corresponding L-enantiomeric excesses (%Lee = % L - % D) of protein amino acids measured in the Hillsborough and Murchison hot-water extracts. The enantiomeric ratios and Lee values were based on the average of three measurements of each amino acid of the non-hydrolyzed (free) and 6 M HCl-hydrolyzed (total) hot-water extracts after OPA/NAC derivatization and liquid chromatography with UV fluorescence and mass spectrometry detection. The errors shown were calculated by standard error propagation of the uncertainties given for the individual amino acid abundances in Table S-8.

	Hillsborough (CM1/2)				Murchison (CM2)			
	Free		Total		Free		Total	
Amino Acid	D/L	Lee (%)	D/L	Lee (%)	D/L	Lee (%)	D/L	Lee (%)
Aspartic Acid	0.57 ± 0.08	27 ± 5	0.23 ± 0.01	63 ± 1	0.64 ± 0.02	22 ± 1	0.28 ± 0.02	56 ± 2
Glutamic Acid	0.73 ± 0.09	16 ± 5	0.16 ± 0.02	72 ± 2	0.60 ± 0.04	25 ± 3	0.21 ± 0.01	65 ± 1
Serine	0.13 ± 0.01	78 ± 1	0.050 ± 0.003	91 ± 1	0.36 ± 0.02	47 ± 2	0.041 ± 0.001	92 ± 1
Alanine	0.94 ± 0.04	3.2 ± 2.2	0.21 ± 0.01	65 ± 1	1.04 ± 0.05	-1.7 ± 2.3	0.51 ± 0.02	32 ± 1
Valine	0.73 ± 0.16	16 ± 9	0.07 ± 0.01	88 ± 1	1.4 ± 0.1	-17 ± 4	0.11 ± 0.01	81 ± 1

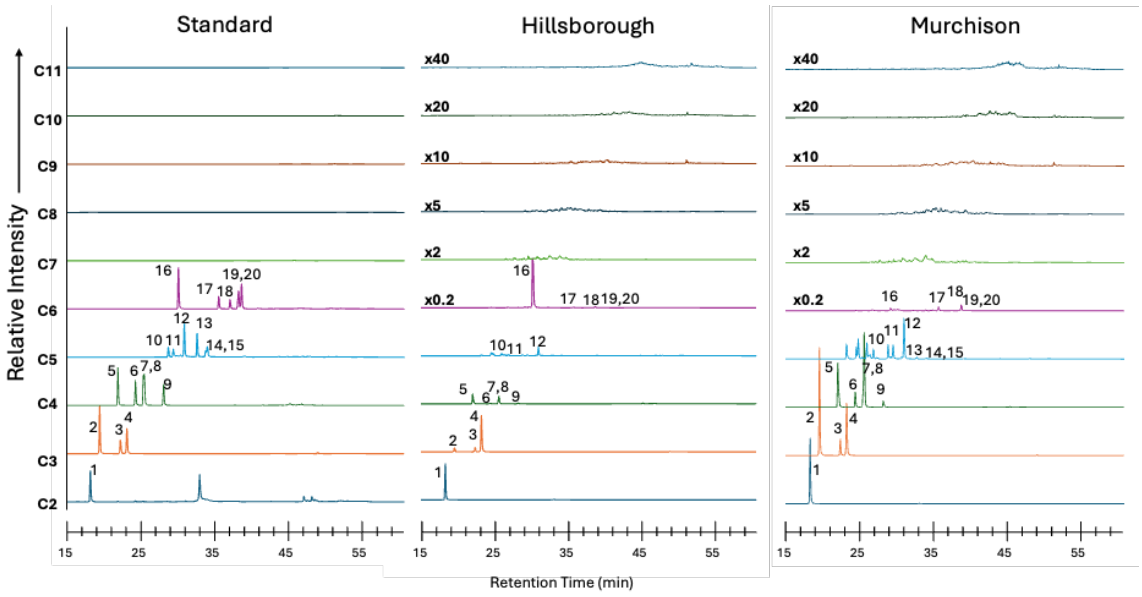

Fig. S-19. LC-ToF-MS chromatograms showing the elution of the C2 to C11 amino acids (H_2N-$(CH_2)_n$-COOH) in the acid-hydrolyzed, hot-water extracts of procedural blank, Hillsborough, and Murchison meteorites, respectively. The 15- to 60-min regions of the LC-ToF single-ion mass chromatograms corresponding to the *o*-phthaldialdehyde/*N*-acetyl-L-cysteine (OPA/NAC) derivatives of C2 to C11 aliphatic primary amino acids in positive ion mode via heated electrospray ionization and a 5 ppm mass accuracy with corresponding *m/z* values as follows: **C2**: *m/z* = 337.08527; **C3**: *m/z* = 351.10092; **C4**: *m/z* = 365.11657; **C5**: *m/z* = 379.13222; **C6**: *m/z* = 393.14787; **C7**: *m/z* = 407.16352; **C8**: *m/z* = 421.17917; **C9**: *m/z* = 435.19482; **C10**: *m/z* = 449.21047; and **C11**: *m/z* = 463.22612. Similar single-ion chromatograms were obtained for the non-hydrolyzed water extracts. Peaks were identified by comparisons of their retention times and exact monoisotopic masses with those in the amino acid standard analyzed on the same day, and are designated by peak number as follows: (1) glycine, (2) β-alanine, (3) D-alanine, (4) L-alanine, (5) γ-aminobutyric acid, (6) D-β-amino-*n*-butyric acid, (7) L-β-amino-*n*-butyric acid, (8) a-aminoisobutyric acid, (9) D,L-a-aminobutyric acid, (10) D-isovaline, (11) L-isovaline, (12) L-valine, (13) D-valine, (14) D-norvaline, (15) L-norvaline, (16) ε-amino-*n*-caproic acid, (17) L-isoleucine, (18) D-isoleucine, (19) D-leucine, and (20) L-leucine.

Table S-10. Detection metrics observed for selected C2 to C6 amino acids using the LC-FD/ToF-MS analytical technique. As a result of derivatization with OPA/NAC, 261 Da is added to the measured mass of each amino acid. Mass error was calculated using the following equation:

	Chemical Formula [M+H]+	SIC RT (min)	FLR RT (min)	Theoretical m/z	Experimental m/z	Mass Error (ppm)
Acidic amino acids						
D-aspartic acid	$C_{17}H_{19}N_2O_7S$	4.63	4.48	395.0913	395.0916	0.76
L-aspartic acid	$C_{17}H_{19}N_2O_7S$	4.98	4.85	395.0913	395.0922	2.28
D-glutamic acid	$C_{18}H_{21}N_2O_7S$	7.23	7.10	409.1069	409.1067	-0.49
L-glutamic acid	$C_{18}H_{21}N_2O_7S$	6.93	6.78	409.1069	409.1073	0.98
Hydroxy amino acids						
D-serine	$C_{16}H_{19}N_2O_6S$	12.53	12.40	367.0964	367.0961	-0.82
L-serine	$C_{16}H_{19}N_2O_6S$	12.98	12.82	367.0964	367.0969	1.36
C2 amino acid						
Glycine	$C_{15}H_{17}N_2O_5S$	18.12	17.98	337.0858	337.0855	-0.89
C3 amino acids						
β-alanine	$C_{16}H_{19}N_2O_5S$	19.37	19.40	351.1015	351.1020	1.42
D-alanine	$C_{16}H_{19}N_2O_5S$	22.14	22.00	351.1015	351.1018	0.85
L-alanine	$C_{16}H_{19}N_2O_5S$	23.01	22.87	351.1015	351.1014	-0.28
C4 amino acids						
D,L-α-amino-*n*-butyric acid	$C_{17}H_{21}N_2O_5S$	27.91	27.75	365.1171	365.1179	2.19
ɣ-amino-*n*-butyric acid	$C_{17}H_{21}N_2O_5S$	21.88	21.67	365.1171	365.1190	5.20
α-aminoisobutyric acid	$C_{17}H_{21}N_2O_5S$	25.32	25.20	365.1171	365.1177	1.64
C5 amino acids						
D-valine	$C_{18}H_{23}N_2O_5S$	32.38	32.22	379.1328	379.1310	-4.75
L-valine	$C_{18}H_{23}N_2O_5S$	30.67	30.52	379.1328	379.1312	-4.22
D-isovaline	$C_{18}H_{23}N_2O_5S$	28.55	28.38	379.1328	379.1322	-1.58
L-isovaline	$C_{18}H_{23}N_2O_5S$	29.21	29.05	379.1328	379.1320	-2.11
C6 amino acid						
ε-amino-*n*-caproic acid	$C_{19}H_{25}N_2O_5S$	29.90	29.75	393.1484	393.1491	1.78

Carboxylic acids

By: Jose Aponte and Denise Buckner

Methods: Standards and reagents. All glassware and sample handling tools were rinsed with Milli-Q ultrapure water (18.2 MΩ·cm, < 3 ppb total organic carbon), wrapped in aluminum foil, and combusted in a furnace at 500 °C in air overnight. Solvents, standards, and reagents were purchased from Sigma-Aldrich, Fischer Scientific, and Alfa Aesar, and used without purification, except 6 M hydrochloric acid (HCl), which was double-distilled. Chemicals include semiconductor grade sodium hydroxide (NaOH), HPLC grade dichloromethane (DCM), and *n*-propanol (99%). A stock solution of 23 carboxylic acids was prepared by mixing individual standards (97- 99% purity) in Milli-Q ultrapure water. 2 M NaOH was prepared by dissolving 32 g of semiconductor grade NaOH pellets in 400 mL Milli-Q ultrapure water. Functionalized aminopropyl silica gel (SiliCycle, SiliaBondȮ, 40–63 µm particle size) was cleaned using methanol and DCM rinses and dried under vacuum.

A 45% portion of each non-vapor hydrolyzed hot water extract (prepared as a companion for amino acid analyses) was allocated for carboxylic acid analysis (36.5 mg of Hillsborough and 37.0 mg of Murchison). The extracts were made basic with the addition of 20 µL 2 M NaOH, dried under reduced pressure, and derivatized with an *n*-propanol esterification protocol, modified from previously described methods (*27*). Dried residues were suspended in 20 µL of 6 M HCl, 30 µL of *n*-propanol, and 200 µL of DCM, then heated at 100 °C for 16 h in sealed PFTE-lined screw cap vials on a heating block; this reaction converts carboxylic acids into their respective *n*-propyl esters. Derivatized extracts were cooled to room temperature, passed through aminopropyl silica gel (5 mm length × 5 mm I.D.), and the filtrate used for analysis.

Carboxylic acid concentrations and compound-specific ^{13}C isotopes in samples and procedural blanks were quantified with gas chromatography coupled to mass spectrometry and isotope ratio mass spectrometry (GC-MS/IRMS) with a custom setup that enables simultaneous measurements of molecular structures and their compound-specific stable isotopes from a single injection. The GC-MS/IRMS consists of a Thermo Trace GC Ultra, whose output is split: approximately 10% is directed to a Thermo DSQ II triple-quadrupole MS through a transfer line heated to 320 °C, and 90% to a Thermo MAT 253+ IRMS oxidation reactor through a Thermo GC-C III interface via a 250 µm deactivated silica column (Restek). Carboxylic acid abundances were quantified from peak areas generated using the average of three separate GC-MS measurements on the same sample, then blank-subtracted. Isotopes were quantified using $^{13}C/^{12}C$ (‰) ratios from the average of three separate IRMS measurements per sample.

The GC was equipped with two Rxi-5ms (30 m length × 0.25 mm I.D. × 0.50 µm film thickness, Restek) and one PoraBOND Q PT column (25 m length × 0.25 mm I.D. × 3.00 µm film thickness, two particle traps, Agilent), joined in series by SilTite µ-union connectors (Restek). Analyses used triplicate injections of derivatized carboxylic acids in aliquots of 3 µL through an injector heated at 270 °C in splitless mode. The oven program began with a temperature of 50 °C held for 1 min, ramped

to 300 °C at 5 °C/min, and held at a final temperature of 300 °C for 15 minutes. Ultrahigh purity grade helium (5.0 grade) carrier gas was delivered at a constant flow of 2.0 mL/min.

The MS used full scan mode over m/z from 30 to 600, the filament was turned on 16 minutes after injection, and the ionization source was heated at 250 °C in electron impact (EI) mode at 70 eV. Using Thermo Xcalibur software, carboxylic acid derivatives were identified and quantified by comparison to a mix of 23 carboxylic acid reference standards taken through the derivatization procedure and application of calibration curves, as described elsewhere (*78*).

Analytes sent to the IRMS were converted to CO_2 in a ceramic oxidation reactor containing a copper (II) oxide/platinum/nickel wire (Thermo) heated to 940 °C. Isotopic values were evaluated using high-purity CO_2 reference gas ($\delta^{13}C$ = -43.35‰ VPDB, SD = 0.08‰) that was pre-calibrated against commercial reference CO_2, with ten pulses introduced into the IRMS at the beginning of each run and five more at the end. IRMS data was analyzed using Thermo Isodat 2.5 software. The derivatized mix of 23 reference carboxylic acids used for quantification of GC-MS data was also analyzed by IRMS, and the same underivatized standards were analyzed on a Costech ECS 4010 combustion elemental analyzer (EA) connected to the IRMS to correct for carbons added during derivatization. To calculate the $\delta^{13}C$ value of each derivatized carboxylic acid, a correction was applied with Eq. 3 (*79*):

$$\delta^{13}C_{\text{sample CA}} = [((n_{MCA} + n_d)/n_{CA}) \times (\delta^{13}C_{\text{deriv. sample CA}} - \delta^{13}C_{\text{deriv. std CA}})] + \delta^{13}C_{\text{underivatized std CA}} \quad (3)$$

where n_{CA} is the number of carbon atoms in the underivatized carboxylic acid (CA), and n_d is the number of carbons added by the *n*-propanol. The $\delta^{13}C$ value for the carbon added through esterification is determined for each individual carboxylic acid, accounting for kinetic isotope effects during derivatization. The precision of the calculated value depends on the precision of the three measurements (i.e., derivatized sample, derivatized standard, underivatized standard) and is calculated using Eq. 4 (*79*):

$$\delta^2_{\text{sample MCA}} = \delta^2_{\text{underivatized std}} + [\delta^2_{\text{derivatized std}} \times ((n_{MCA} + n_d)/n_{MCA})^2] + [\delta^2_{\text{derivatized sample}} \times ((n_{MCA} + n_d)/n_{MCA})^2] \quad (4)$$

Results: Figure S-22 illustrates the selected ion chromatogram (summed *m/z* = 42 + 43 + 57 + 71 + 85 + 99 + 101 + 105 + 115) from GC-MS analyses of a procedural blank, the Hillsborough meteorite, the Murchison meteorite, and a mixture of carboxylic acid standards. The summed *m/z* values were selected for the carboxylic acids of interest. 13 carboxylic acids were detected in both Hillsborough and corresponding Murchison samples, including a suite of straight chain monocarboxylic acids C_1-$C_{6:0}$, three branched carboxylic acids with 4 to 5 carbons, benzoic acid, and three dicarboxylic acids with 2 to 5 carbons (Table S-12). Total carboxylic acids (Table S-13) were 1.78x more abundant in Murchison than Hillsborough, and both meteorites display molecular distributions and abundances consistent with CM chondrites (*78,80*). For both meteorites, acetic acid was the most

abundant CA, formic acid was the second most abundant, and abundances of longer-chained MCAs decreased in concentration with increasing molecular weight. In Hillsborough, isobutyric acid was 2.41x more abundant than butyric acid, but branched C_5 CAs were lower in concentration compared to pentanoic acid. In Murchison, both C_4 and C_5 straight-chain CAs predominated over branched counterparts. Dicarboxylic acids comprised a small fraction of Hillsborough total CAs (4.6%) but made up a larger percentage in Murchison (12.4%), primarily due to a high amount of oxalic acid (Figure S-20).

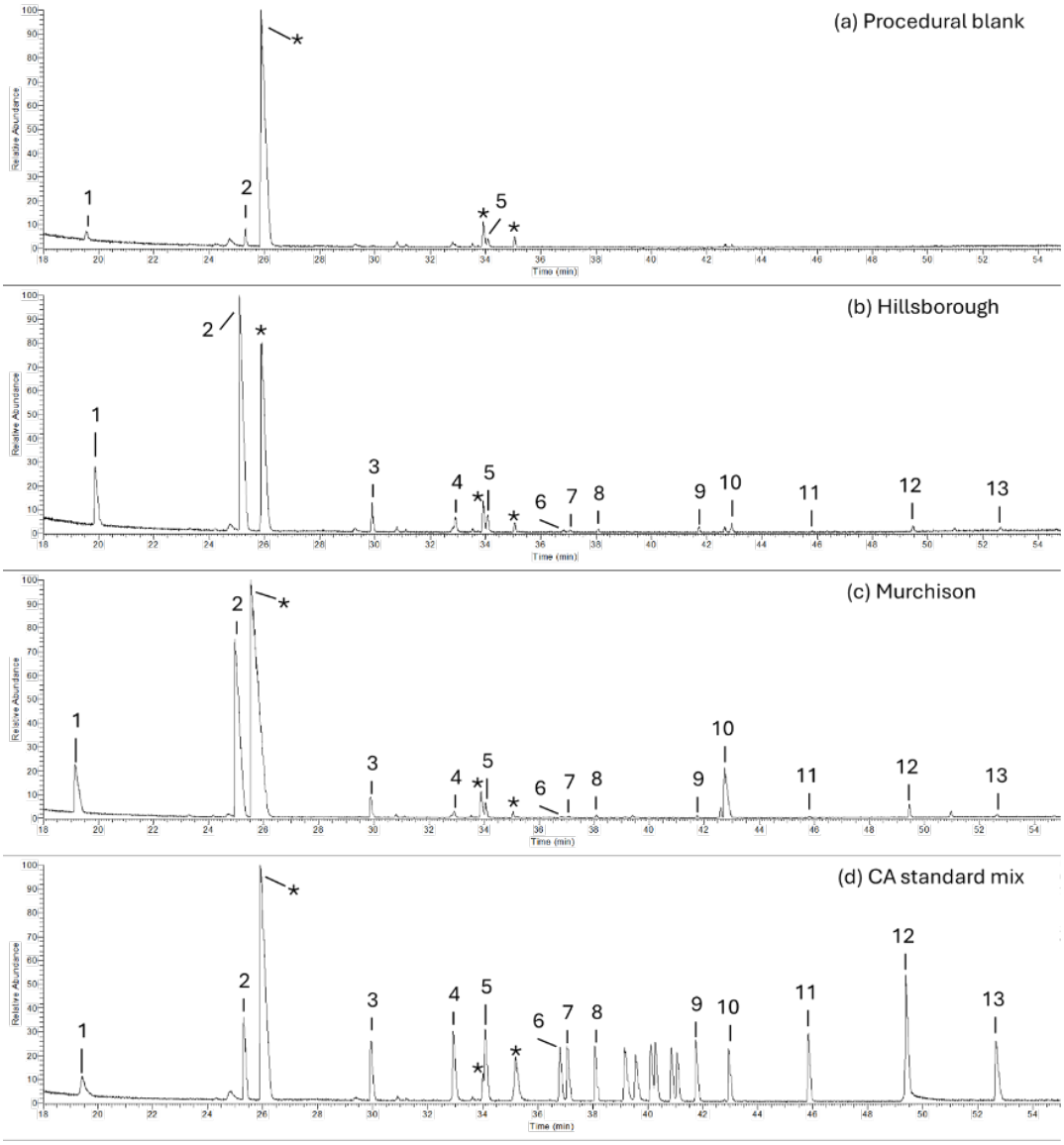

Figure S-20. Chromatograms from GC-MS analyses of carboxylic acids in hot water extracts from (a) procedural blank, (b) Hillsborough, (c) Murchison, and (d) a mix of carboxylic acid (CA) standards. Chromatograms displayed represent summed *m/z* values selected for the carboxylic acids of interest (*m/z* = 42 + 43 + 57 + 71 + 85 + 99 + 101 + 105 + 115). All extracts were derivatized with an *n*-propanol esterification protocol prior to analysis. Compounds include (1) formic, (2) acetic,

(3) propanoic, (4) isobutyric, (5) butyric, (6) 2-methylbutyric, (7) isopentanoic, (8) pentanoic, (9) hexanoic, (10) oxalic, (11) benzoic, (12) succinic, and (13) glutaric acids. * indicates *n*-propanol and *n*-propanol derivatization byproducts, and unlabeled peaks in panel (d) correspond to CA standards in the 23-standard mix that were not detected in any of the meteorite samples.

Table S-11. Carboxylic acid abundances, in nmol g^{-1}, detected in hot water extracts from the Hillsborough and Murchison meteorites. Extracts were derivatized with *n*-propanol and analyzed with gas chromatography-mass spectrometry (GC-MS). Individual carboxylic values and standard deviations are blank-subtracted and based on the average of triplicate analyses of the same sample. Total carboxylic abundances represent the summed average values of individual compounds, and error was calculated by standard error propagation of the uncertainties for individual carboxylic acid abundances.

Carboxylic Acid	Hillsborough	Murchison
Formic	3,486 ± 409	6,419 ± 460
Acetic	5,774 ± 755	8,508 ± 498
Propanoic	271 ± 50	325 ± 20
Isobutyric	131 ± 19	53 ± 5
Butyric	54 ± 17	102 ± 12
2-Methylbutyric	14 ± 2	16 ± 1
Isopentanoic	10 ± 2	15 ± 1
Pentanoic	7 ± 3	17 ± 9
Hexanoic	132 ± 16	79 ± 2
Oxalic	111 ± 18	2,081 ± 105
Benzoic	10 ±1	17 ± 1
Succinic	16 ± 3	78 ± 6
Glutaric	18 ± 1	22 ± 1
Total abundance	**9,919 ± 1,567**	**17,658 ± 1,351**

Table S-12. Compound-specific $\delta^{13}C$ values (‰ VPDB) of carboxylic acids detected in hot water extracts from the Hillsborough and Murchison meteorites. Extracts were derivatized with *n*-propanol and analyzed with isotope ratio mass spectrometry (IRMS). Values and standard deviations for individual $\delta^{13}C$ values were calculated from N = 3 of the same sample.

Carboxylic Acid	Hillsborough	Murchison
Formic	+25.7 ± 12.3	+21.7 ± 7.5
Acetic	-19.1 ± 7.6	-13.9 ± 7.7
Propanoic	n.d.	+6.7 ± 4.7
Oxalic	+7.4 ± 9.7	+44.9 ± 9.8

Table 2 shows the $\delta^{13}C$ values for carboxylic acids that were detectable with IRMS, which includes formic, acetic, and oxalic acids for Hillsborough, and formic, acetic, propanoic, and oxalic acids for Murchison. Carboxylic acid $\delta^{13}C$ values varied across each sample, ranging from -19.1 to +25.7‰ in Hillsborough and -13.9 to +44.9‰ in Murchison values. Formic acid was enriched and displayed similar values for both Hillsborough and Murchison (+25.7 and +21.7‰), acetic acid was depleted for both meteorites (-19.1 and -13.9‰), and oxalic acid displayed positive $\delta^{13}C$ values in both meteorites but is relatively less enriched in Hillsborough (+7.4) compared to Murchison (+44.9).

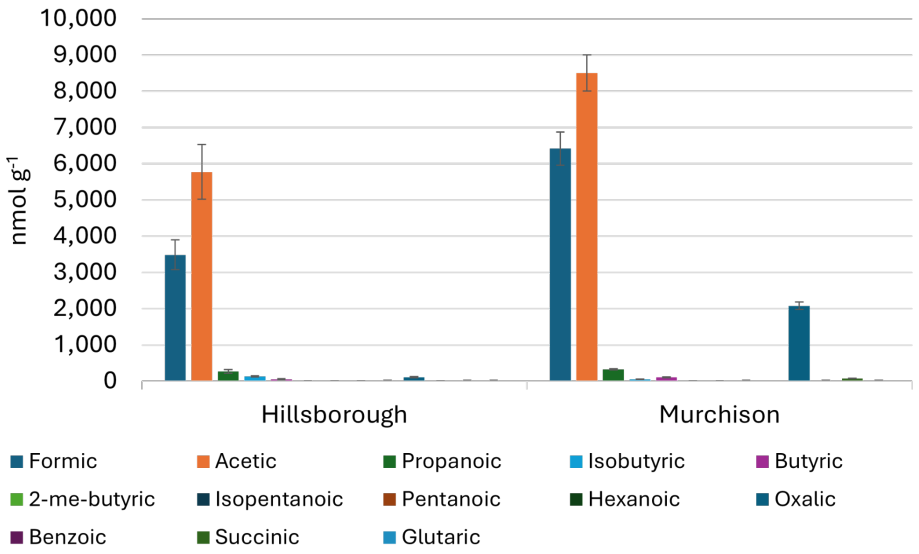

Fig. S-21. Abundances of individual carboxylic acids (nmol g^{-1}) detected in hot water extracts from the Hillsborough and Murchison meteorites. Abundances are blank-subtracted, and error bars represent the standard deviation calculated from triplicate measurements of the same sample. Extracts were derivatized with *n*-propanol. (a) displays all carboxylic acids, and (b) displays lower-abundance compounds only (formic, acetic, and oxalic acids excluded). Compounds include straight-chain and branched monocarboxylic acids (MCAs) from C_1- $C_{6:0}$, benzoic acid, and dicarboxylic acids (DCAs). Straight-chain MCAs: formic (C_1), acetic ($C_{2:0}$), propanoic ($C_{3:0}$), butyric ($C_{4:0}$), pentanoic ($C_{5:0}$), and hexanoic ($C_{6:0}$) acids. Branched MCAs: isobutyric (C_4), 2-methylbutyric (C_5), and isopentanoic (C_5). DCAs: oxalic (C_2), succinic (C_4), and glutaric (C_5) acids.

Compound-specific stable ^{13}C isotopes (Table S-13) indicate that carboxylic acids in Hillsborough are indigenous, and values similar to Murchison suggest similar isotopic reservoirs in the respective parent bodies or the pre-accretionary cloud. Extraterrestrial carboxylic acids tend to display positive $\delta^{13}C$ values, while CAs in the terrestrial biosphere are generally more ^{13}C-depleted. Formic and oxalic acids in Hillsborough and Murchison were enriched (+25.7 to +44.9‰), consistent with an extraterrestrial origin, while the relatively depleted acetic acid values (-19.1 and -13.9‰) could point to terrestrial contamination (*77,78*). While oxalic acid displays positive isotopic values in both meteorites, oxalic acid in Hillsborough is less enriched than Murchison. Variability in oxalic acid values for the two meteorites could reflect differences in isotopic reservoirs between the two parent bodies or alternatively may indicate contributions from terrestrial contamination for Murchison. Overall, the molecular abundances, distributions, and isotopic signatures for carboxylic acids in Hillsborough (Figure S-21) point to an extraterrestrial origin and display good agreement with Murchison and other CM1/2 and CM2 chondrites (*81,82*).

Pyrolysis-gas chromatography-triple quadrupole-mass spectrometry
By: Angel Mojarro

Methods: Hillsborough, fused silica control, and co-analyzed Murchison samples were prepared by loading ~1 mg of fines into quartz pyroprobe tubes (CDS Analytical, Catalog: 6201-3004) inside a HEPA filtered laminar flow bench. All glassware used to handle samples and pyrolysis tubes were previously combusted at 550°C for ~16 h in air.

Pyrolysis experiments were conducted on a CDS Analytical 6200 pyroprobe configured for manual loading and flash (10°C ms-1) heating ramps under a continuous flow (35 mL min^{-1}) of ultra-high purity (>99.9 %) helium. Samples were heated in the pyrolysis furnace from 50 to 600°C (pyroprobe actual ~610°C) and held for 20 s to thermally degrade insoluble organic matter (IOM) and extract the stable hydrocarbon fraction. The pyroprobe housing and valves were held at 300°C and volatiles were transferred via a heated transfer line (300°C) directly into a Thermo Scientific TRACE 1600 gas chromatograph (GC) coupled to an Thermo Scientific 9610 triple quadrupole mass spectrometer (TSQ) system. The inlet temperature was held at 300°C and operated with a 10:1 split.

The GC was fitted with an Rtx-5MS capillary column (30 m × 0.25 mm × 0.25 μm) with 5 m Integra-Guard column, He carrier flow at 1.5 mL min-1, and MS transfer line set to 300°C. The GC oven was programmed with the following method: 40°C hold for 5 min, followed by a 3.5°C min-1 ramp to 300°C, then a final isothermal hold at 300°C for 8.5 min (~88 min total). The MS source was held at 300°C and was operated in electron impact (EI) mode at 70 eV and simultaneous fullscan (m/z 50–500) and multiple reaction monitoring (MRM). Py-GC-QqQ-MS operated in MRM mode works by using specific precursor-product reactions in which Q1 scans for a specific precursor ion, filtered ions enter a collision cell (q), and Q3 scans for its diagnostic production. MRM transitions targeted IOM-derived hydrocarbons and S, N, and O-containing compounds informed by prior pyrolysis experiments on CM, CR, and CI carbonaceous chondrites. Pyrolysis blanks preceded all standard pyrolysis experiments to control the cleanliness of the analytical set-up and prevent potential cross-contamination. Results were analyzed using Chromeleon 7.3.1 software. Compound identification was conducted via comparison with retention time, three MRM transitions of standards, mass fragmentation patterns of standards, and comparison to previously characterized analog materials (i.e carbonaceous chondrites and coal standards).

Pyrolysis of Hillsborough and Murchison to ~600°C released an identical suite of compounds primarily comprised aromatic hydrocarbons, polycyclic aromatic hydrocarbons (PAHs), and organosulfur compounds along with alkylated species (e.g., alkylbenzenes, alkylnaphthalenes, alkylthiophenes). Aromatic compounds included benzene, naphthalene, phenanthrene, anthracene, fluoranthene, pyrene, C1 – C5 alkylbenzenes, and C1 – C5 alkylnaphthalenes, C1 – C4 alkylphenanthrenes, and C1 – C2 alkylpyrenes (Table 1). Organosulfur compounds included thiophene, benzothiophene, thienothiophenes, benzothiazole, bithiophene, dibenzothiophene, C1 - C3 alkylthiophenes, and C1 alkylbenzothiophenes. Nitrogen-containing compounds included pyridine, aniline, benzonitrile, quinoline, indole, and carbazole while oxygen-containing compounds were benzaldehyde, phenol, benzofuran, dibenzofuran, and fluorenone (Figure S-22).

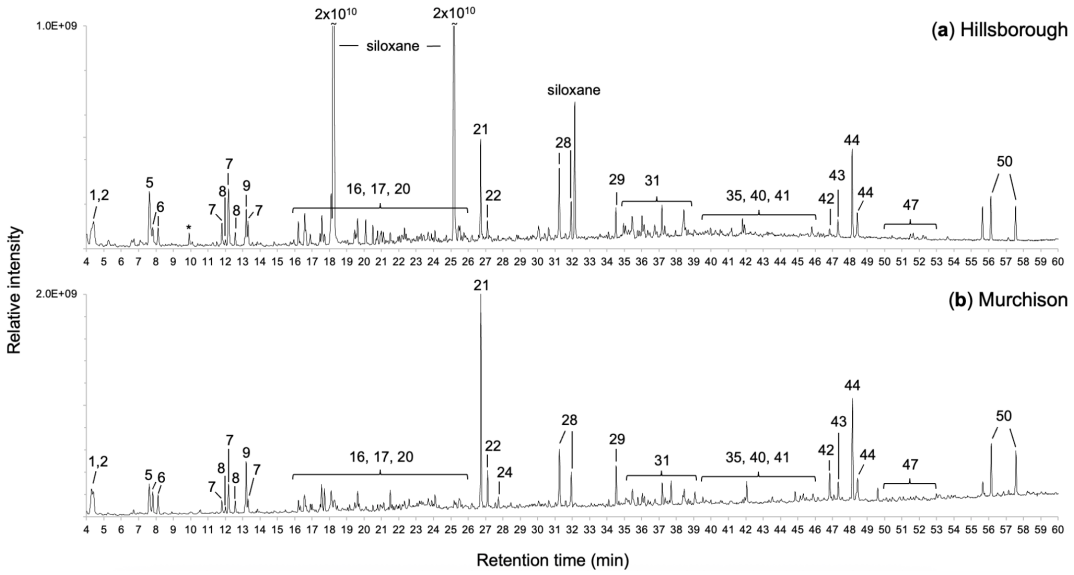

Fig. S-22. Total ion chromatograms (TIC) after flash pyrolysis to 600 °C of the (a) Hillsborough and (b) Murchison meteorites. Analytes were identified by diagnostic mass transitions and retention time. Peaks observable in the TIC are as follows: (1) benzene, (2) thiophene, (5) toluene, (6) C1-alkylthiophenes, (7) C2-alkylbenzenes, (8) C2-alkylthiophenes, (9) styrene, (16) C3-alkylbenzenes, (17) C3-alkylthiophenes, (20) C4-alkylbenzenes, (21) naphthalene, (22) benzothiophene, (28) C1-alkylnaphthalenes, (29) biphenyl, (31) C2-alkylnaphthalenes, (35) C3-alkylnaphthalenes, (40) C4-alkylnaphthalene, (41) C5-alkylnaphthalene, (42) fluorenone, (43) dibenzothiophene, (44) phenanthrene & anthracene, (47) C1-alkylphenanthrenes, (50) fluoranthene & pyrene.

Table S-13. Table with identified analytes, retention times, and mass transitions for Fused Silica (FS), Murchison (MS), and Hillsborough (HB).

#	Analyte	Time (min)	Precursor m/z	Product m/z	FS	MU	HB
1	Benzene	4.3 ± 1	78.1	52.1	-	+	+
			78.1	63.1	-	+	+
			78.1	77.1	-	+	+
2	Thiophene	4.4 ± 1	84.1	45	-	+	+
			84.1	58	-	+	+
			84.1	69	-	+	+
3	Dimethyl disulfide	6.7 ± 1	94	61	-	+	+
			94	64	-	+	+
			94	79	-	+	+
4	Pyridine	6.8 ± 1.5	52.1	26.1	-	+	+
			79.1	52.1	-	+	+
			79.1	77.1	-	n.d.	n.d.
5	Toluene	7.6 ± 1	91.1	39.1	-	+	+
			91.1	65.1	-	+	+
			92.1	91.1	-	+	+
6	C_1-Alkylthiophenes	8 ± 1.5	97.1	45	-	+	+
			97.1	53.1	-	+	+
			97.1	69	-	+	+
7	C_2-Alkylbenzenes	12.5 ± 3	91.1	65.1	-	+	+
			105.1	77.1	-	+	+
			106.1	91.1	-	+	+
8	C_2-Alkylthiophenes	13 ± 3	111.1	77.1	-	+	+
			112.1	97	-	+	+
			112.1	111	-	+	+
9	Styrene	13.2 ± 1	78.1	52.1	-	+	+
			104.1	78.1	-	+	+
			104.1	103.1	-	+	+
10	Benzaldehyde	16.5 ± 1	77.1	51.1	-	+	+
			105.1	77.1	-	+	+
			106.1	105.1	-	+	+
11	Dimethyl trisulfide	17 ± 1	79	64	-	+	+
			126	79	-	+	+
			126	111.1	-	+	+
12	Aniline	17.4 ± 1	93.1	65.1	-	+	+
			93.1	66.1	-	+	+
			93.1	92.1	-	+	+
13	Phenol	17.6 ± 1	66.1	65.1	-	+	+
			94.1	39.1	-	+	+
			94.1	66.1	-	+	+
14	Benzonitrile	17.7 ± 1	76.1	50	-	+	+
			103.1	50	-	+	+
			103.1	76.1	-	+	+
15	Benzofuran	18.3 ± 1	90.1	63.1	-	+	+
			90.1	89.1	-	+	+
			118.1	117.1	-	+	+
16	C_3-Alkylbenzenes	18.5 ± 6	105.1	77.1	-	+	+
			105.1	103.1	-	+	+
			120.2	105.1	-	+	+

#	Analyte	Time (min)	Precursor m/z	Product m/z	FS	MU	HB
17	C_3-Alkylthiophenes	19 ± 8	125.1	97.1	-	+	+
			126.1	111	-	+	+
			126.1	125.1	-	+	+
18	Indane	19.6 ± 1	115.1	89.1	-	+	+
			117.1	115.1	-	+	+
			118.1	117.1	-	+	+
19	Indene	20.5 ± 1	115.1	89	-	+	+
			115.1	114.2	-	+	+
			116.1	115.1	-	+	+
20	C_4-Alkylbenzenes	23 ± 8	119.1	77.1	-	+	+
			119.1	91.1	-	+	+
			134.2	119.1	-	+	+
21	Naphthalene	26.8 ± 1	128.1	78.1	-	+	+
			128.1	102.1	-	+	+
			128.1	127.1	-	+	+
22	Benzo[c]thiophene	27.1 ± 1	134.1	89.1	-	+	+
			134.1	90.1	-	+	+
			134.1	108	-	+	+
23	Benzothiazole	28.5 ± 1	108	69	-	+	+
			135	91	-	+	+
			135	108	-	+	+
24	Thieno[n,n]thiophenes	28.5 ± 2	96.1	70	-	+	+
			96.1	95	-	+	+
			140	96	-	+	+
25	Quinoline	29 ± 1	129.1	102.1	-	+	+
			129.1	128.1	-	+	+
			102.1	102.1	-	+	+
26	Indole	31.2 ± 1.5	89	63	-	+	+
			90	89.1	-	+	+
			117	89.1	-	+	+
27	C_1-Alkylbenzo[b]thiophenes	31.5 ± 2	147.1	77.1	-	+	+
			147.1	103.1	-	+	+
			148.1	147	-	+	+
28	C_1-Alkylnaphthalenes	31.6 ± 1.5	141.1	115.1	-	+	+
			142.1	115.1	-	+	+
			142.1	141.1	-	+	+
29	Biphenyl	34.5 ± 1	76.1	63.1	-	+	+
			154.1	152.1	-	+	+
			154.1	153.1	-	+	+
30	Bithiophene	36 ± 3	121	77	-	+	+
			166	121	-	+	+
			166	134	-	+	+
31	C_2-Alkylnaphthalenes	36.1 ± 4	141.1	115.1	-	+	+
			156.1	115.1	-	+	+
			156.1	141.1	-	+	+
32	Acenaphthylene	37.2 ± 1	76.1	63.1	-	+	+
			152.1	126.1	-	+	+
			152.1	151.1	-	+	+
33	Acenaphthene	38.5 ± 1	153.1	152.1	-	+	+
			154.1	153.1	-	+	+

#	Analyte	Time (min)	Precursor m/z	Product m/z	FS	MU	HB
34	Dibenzofuran	39.5 ± 1	139.1	113	-	+	+
			168.1	139	-	+	+
			169.1	140	-	+	+
35	C_3-Alkylnaphthalenes	40.5 ± 5.5	155.2	128.1	-	+	+
			155.2	153.1	-	+	+
			170.2	155.1	-	+	+
36	Phenalene	41.2 ± 1.5	165.1	115	-	+	+
			165.1	139	-	+	+
			166.1	165.1	-	+	+
37	Fluorene	41.8 ± 1.5	165.1	95.1	-	+	+
			165.1	109.1	-	+	+
			166.1	165.1	-	+	+
39	Benzophenone	43.4 ± 1	105	77.1	-	+	+
			182.1	105	-	+	+
			182.1	181.1	-	+	+
40	C_4-Alkylnaphthalene	44 ± 6	169.1	153.1	-	+	+
			184.1	154.1	-	+	+
			184.1	169.1	-	+	+
41	C_5-Alkylnaphthalene	46 ± 7.5	183.1	153.1	-	-	-
			183.1	168.1	-	-	-
			198.1	183.2	-	-	-
42	Fluorenone	46.8 ± 1	152.1	126	-	+	+
			152.1	151.1	-	+	+
			180.1	152.1	-	+	+
43	Dibenzothiophene	47.3 ± 2	139.1	113	-	+	+
			184.1	139.1	-	+	+
			184.1	152.1	-	+	+
44	Phenanthrene + Anthracene	48.3 ± 2.5	178.1	152.1	-	+	+
			178.1	176.1	-	+	+
			178.1	177.1	-	+	+
46	Carbazole	49.8 ± 1	167.1	139.1	-	+	+
			167.1	140.1	-	+	+
			167.1	166.1	-	+	+
47	C_1-Alkylphenanthrenes	52 ± 4	191.1	165.1	-	+	+
			192.1	165.1	-	+	+
			192.1	191.1	-	+	+
48	Phenylnaphtalene	53.7 ± 1.5	204.1	189.1	-	+	+
			204.1	202.1	-	+	+
			204.1	203.1	-	+	+
49	C_2-Alkylphenanthrenes	55.2 ± 4	206.1	190.1	-	+	+
			206.1	191.1	-	+	+
			206.1	205.1	-	+	+
50	Fluoranthene + Pyrene	56.8 ± 2.5	202.1	200.1	-	+	+
			202.1	201.1	-	+	+
			101.1	100.1	-	+	+
51	C_3-Alkylphenanthrenes	58.5 ± 6	220.1	189.1	-	+	+
			220.1	190.1	-	+	+
			220.1	219.1	-	+	+
52	C_1-Alkylpyrenes/fluoranthenes	60 ± 3	216.1	215.1	-	+	+
			216.1	189.1	-	+	+
			216.1	214.1	-	+	+

#	Analyte	Time (min)	Precursor m/z	Product m/z	FS	MU	HB
53	C_2-Alkylpyrenes	60 ± 4	215.1	213.1	-	+	+
			230.1	215.1	-	+	+
			230.1	229.1	-	+	+
54	C_4-Alkylphenanthrenes	61 ± 5	219.1	189.1	-	-	-
			219.1	204.1	-	-	-
			234.1	219.1	-	-	-
55	C_3-Alkylpyrenes	65 ± 6	244.1	215.1	-	-	-
			244.1	228.1	-	-	-
			244.1	229.1	-	-	-
56	Terphenyl series	65 ± 5	230.1	215.1	-	+	+
			230.1	228	-	+	+
			230.1	229.1	-	+	+
57	Triphenylene/Chrysene /Naphthacene	65.1 ± 3	228.1	202.1	-	+	+
			228.1	226.1	-	+	+
			228.1	227.1	-	+	+

Fig. S-23. Polycyclic aromatic hydrocarbons (PAHs) and siloxane contaminants measured in the Hillsborough meteorite by pyrolysis gas chromatography mass spectrometry (PyGC-MS).

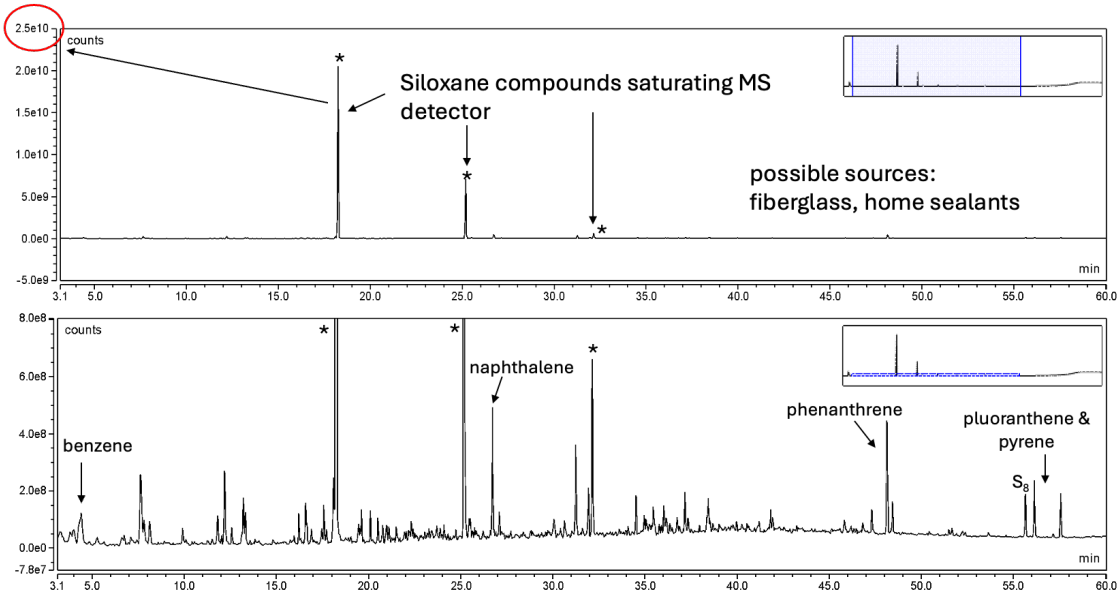

Fig. S-24. Comparison of the distributions of hydrocarbons measured in the Hillsborough and Murchison meteorites by PyGC-MS.

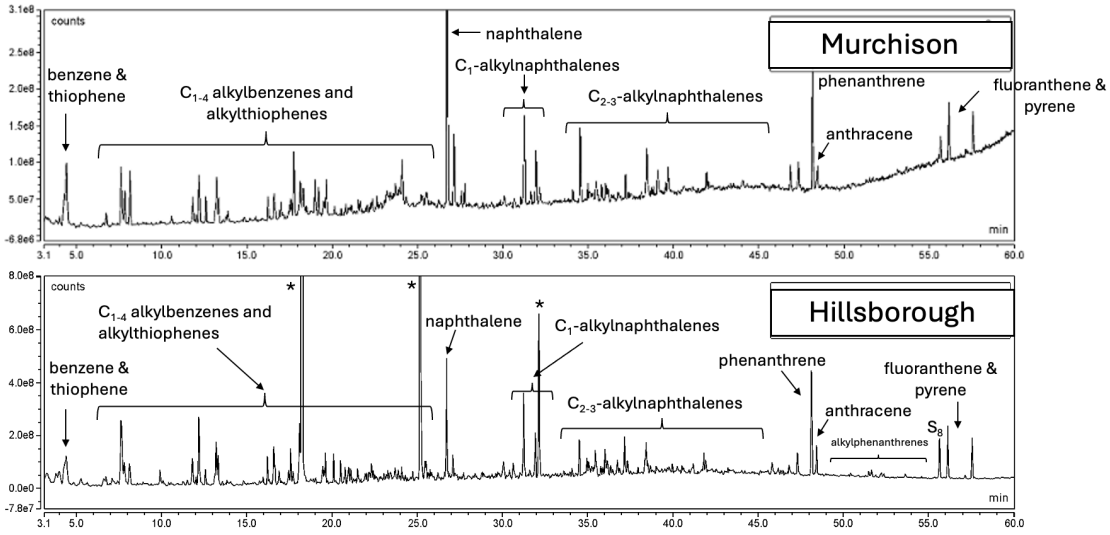

Fig. S-25. Comparison of the distributions of hydrocarbons measured in the Winchcombe and Hillsborough meteorites by PyGC-MS.

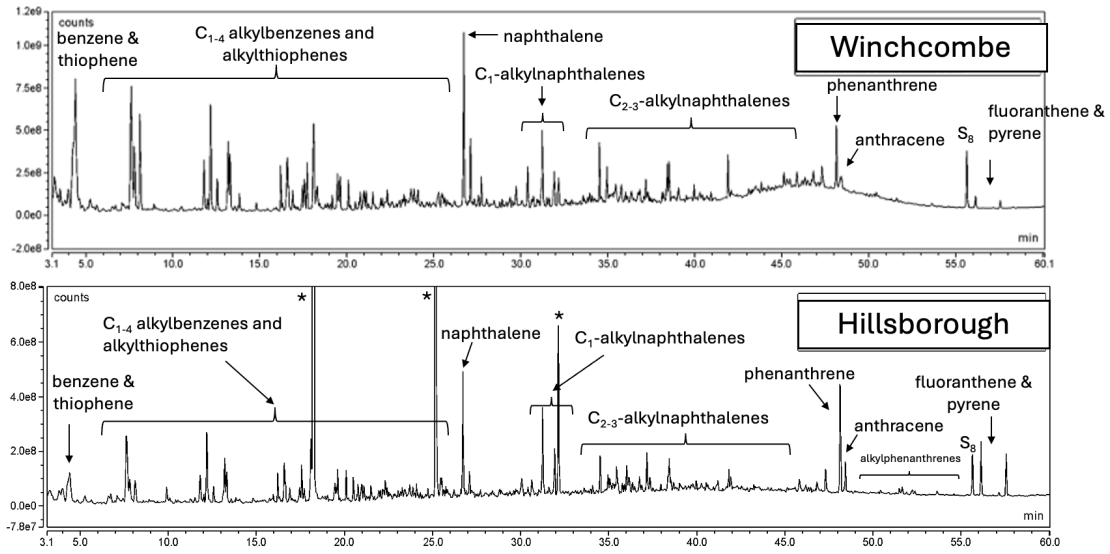

Amino acid content by GC-MS analysis

By: Queenie H. S. Chan, Diptimayee Behera, Jonathan S. Watson, Mark A. Sephton

Methods: A fragment of the Hillsborough meteorite (903.7 mg) and a fragment of the Murchison meteorite (368.8 mg) was separately wrapped in sterile aluminum foil, sent to Royal Holloway University of London, UK, and stored in a N2 purged desiccator prior to soluble organic matter extraction procedure. The fragments were powdered and homogenized in separate ceramic mortar and pestle inside a laminar flow hood under HEPA-filtered positive pressure (equivalent to ISO Class 4–5). 10.8 mg from the powdered Hillsborough sample was analyzed for elemental abundances, and 757.1 mg went through a soluble organic extraction process described below. Environmental samples (total mass = 204.5 mg; including fiberglass insulation, rug floor dirt, carpet) collected from where the meteorite fragment fell was analyzed to assess terrestrial contamination from the local environment. An empty ampoule the procedural blank of GCMS analysis. An amino acid standard mixture was made by combining individual standard solutions (10-3 M) prepared from dissolution of standard amino acid crystals in ultrapure water. The amino acid standards mixture, procedural blank (empty, sterile ampoule), and environmental sample were subjected to the same experimental procedures as the meteorite sample.

All tools, glassware, and ceramics were sterilized by baking at 500 °C in air for 24 hours. Millipore ultrapure water (18.2 MΩ cm, ≤ 3 ppb total organic carbon) was used for all laboratory work performed in this study. The amino acid 3-amino-3-methyl butanoic acid and 3-amino-2,2-dimethylpropanoic acid were provided by Astrobiology Analytical Laboratory at Goddard Space Flight Center, NASA. All other amino acid standard crystals/powder were purchased from Acros Organics, Sigma-Aldrich, and Fluka. Hydrochloric acid (HCl) (37 %), ammonium hydroxide (NH_4OH) (28–30 wt.%), isopropanol (IPA) (99.5 %), and trifluoroacetic anhydride (TFAA) (≥99.0 %) were purchased from Sigma-Aldrich. Acetyl chloride (99+ %) and pyrene (98%) were from Acros Organics. Prepacked columns, analytical grade 50W-X8, hydrogen form (100–200 mesh) were acquired from Bio-Rad. Sodium hydroxide (NaOH) pellets and dichloromethane (DCM) (99.8+ %) were bought from Fisher Scientific.

The Hillsborough meteorite stone was observed under an optical microscope inside a Bassaire laminar flow hood under HEPA-filtered positive pressure (equivalent to ISO Class 4–5) and found to be free of fusion crust. The sample was powdered in a ceramic mortar and pestle inside a laminar flow hood. The sample was homogenized and split into four equal portions of approximately 200 mg each, which were transferred to individual glass ampoules for hot-water extraction. 1 mL of Millipore ultrapure water was added to

each sample. The ampoules were then flame-sealed and heated to 100 ºC for 24 hours in a heating block. After cooling to room temperature, the ampoules were snapped open, and centrifuged for 5 minutes. 10% of the water supernatant was preserved frozen (−80 ºC) for carboxylic acid analysis, and 45% was transferred to small test tubes (12 × 75 mm) individually, dried under vacuum, flame-sealed in larger test tube (20 × 150 mm) containing 1 ml of 6 N HCl, and then subjected to acid vapor hydrolysis for 3 hours at 150 ºC to determine the total (free + bound) amino acid content. The remaining water supernatant (the non-hydrolyzed fraction) was transferred to separate small test tubes. The residual meteorite powders were washed twice with 1 mL ultrapure water and the supernatant was transferred, combined, and dried under vacuum. After the hydrolysis procedure, the test tubes were rinsed with ultrapure water, and then cracked open. The small test tubes were removed and dried under vacuum.

Cation exchange was performed on prepacked columns. The columns were prepared according to the following procedures. After removing the caps and snapping off the seals on the Luer tips, the columns were filled to the top with water (~10 mL) plus one bed volume (~2 mL). Once the volume of water was just above the resin bed, 3 bed volume (~6 mL) of 2M NaOH was added to desorb any contaminating amino acids. The columns were then washed by filling to the top with water twice (20 mL) until the eluting solution has a neutral pH to remove residual NaOH. Three bed volume (~6 mL) of 1.5 M HCl was added to re-acidify the columns. The columns were again washed with two bed volumes of water (20 mL) to remove excess HCl until neutral pH.

Both hydrolyzed and non-hydrolyzed samples were then brought up in 3 × 1 mL of ultrapure water and desalted on the cation exchange resin. Different fractions of the same sample were re-combined by desalting in the same column. Purified amino acids were eluted by adding 2 × 3.5 mL fractions of 2M NH_4OH, and the eluates were collected in small test tubes, which were then evaporated to dryness by vacuum centrifugation.

Prior to GC-MS analysis, amino acids were derivatized by esterification with IPA and acylation with TFAA. The samples were resuspended in 2 × 50 µL of ultrapure water in inserts within GC vials. 100 µL of acetyl chloride:IPA mixture (30:70 v/v) was added to each of the samples. The vials were tightly capped and the samples were heated in a heating block set at 110 °C for 1 hour. The samples were then cooled in an ice bath and dried under a gentle stream of dry N_2. After the samples were brought to room temperature, 100 µL of DCM and 50 µL of TFAA were added to the dried sample. The vials were capped tightly again and heated to 100 °C for 10 minutes. The

samples were then cooled to room temperature and the excess reagent was removed under a slow stream of N2. Prior to injection the derivatized samples were dissolved in 30 μL of DCM and 5 μL of pyrene in DCM (200 μg/mL) as an internal standard. The derivatized samples were then immediately analyzed by GC-MS.

Amino acids in the hot water extracts were analyzed by an Agilent Technologies 7890A series GC coupled to an Agilent Technologies 5975C mass selective detector (MSD). The separations of the D, L-amino acid enantiomers were achieved using a CP-Chirasil-L Val GC Column (25 m × 0.25 mm ID × 0.12 μm; Agilent Technologies). For D,L-isovaline enantiomers separation a 6890N series GC coupled to a 5973 MSD (both Agilent Technologies) and a CP-Chirasil-Dex CB GC Column (25 m × 0.25 mm ID × 0.25 μm; Agilent Technologies) were used.

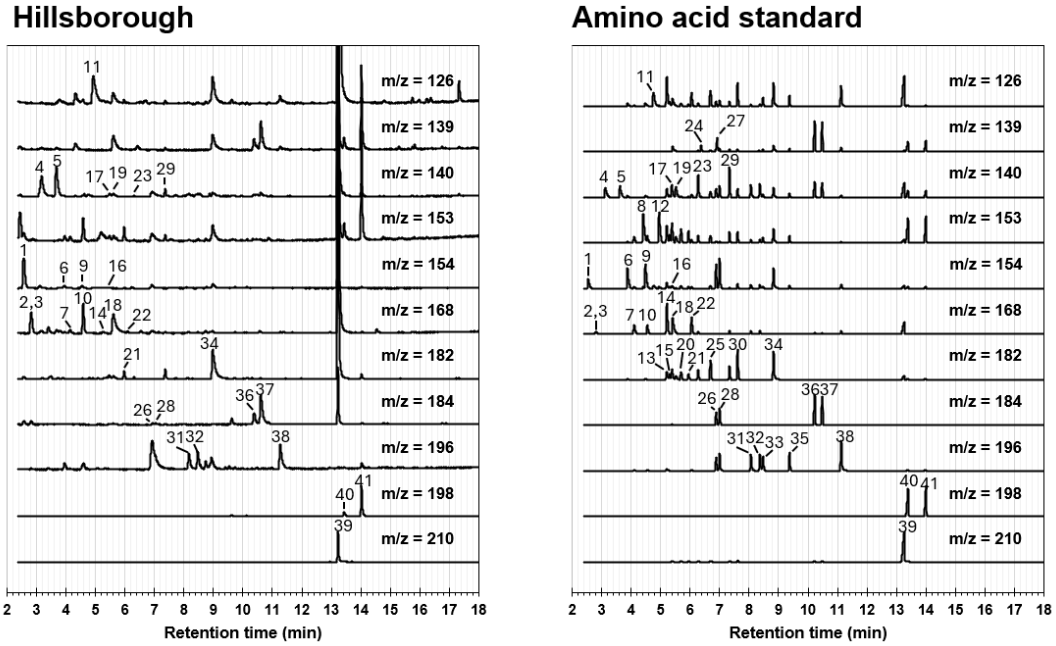

Fig. S-26. The 2–18 min regions of the GC-MS chromatograms. Single ion GC-MS traces (m/z 126, 139, 140, 153, 154, 168, 182, 184, 196, 198, and 210) of the derivatized (N-TFA, O-isopropyl) 6 N HCl-hydrolyzed hot-water extracts of the Hillsborough meteorite and the mixed amino acid standard. The peaks were identified by comparing the retention time and mass fragmentation pattern to those in the amino acid standard run on the same day. D- and L-isovaline enantiomers could not be separated under the chromatographic conditions (Peaks #2 and #3) but their separation was achieved on a different column (CP-Chirasil-Dex CB GC Column). The amino acids are designated by peak number as follows: (1) α-aminoisobutyric acid, (2) D-isovaline, (3) L-isovaline, (4) D-alanine, (5) L-alanine, (6) D-α-amino-n-butyric acid, (7) D-valine, (8) D-threonine, (9) L-α-amino-n-butyric acid, (10) L-valine, (11) Glycine, (12) L-threonine, (13) D-β-aminoisobutyric acid, (14) D-norvaline, (15) L-β-aminoisobutyric acid, (16) D-isoleucine, (17) D-β-amino-n-butyric acidb, (18) β-alanine, (19) L-β-amino-n-butyric acidb, (20) L-alloisoleucine, (21) L-isoleucine, (22) L-norvaline, (23) D-leucine, (24) D-serine, (25) D-norleucine,

(26) R-3-aminopentanoic acid, (27) L-serine, (28) S-3-aminopentanoic acid, (29) L-leucine, (30) L-norleucine, (31) D-4-amino-pentanoic acid, (32) L-4-amino-pentanoic acid, (33) D-2-aminoheptanoic acid, (34) γ-amino-n-butyric acid, (35) L-2-aminoheptanoic acid, (36) D-aspartic acid, (37) L-aspartic acid, (38) 5-aminopentanoic acid, (39) ε-amino-n-caproic acid, (40) D-glutamic acid, and (41) L-glutamic acid.

Table S-14. Blank-corrected abundances (nmol/g) of identified two- to six-carbon amino acids in the non-hydrolyzed (free) and 6M HCl acid-hydrolyzed (total) hot-water extracts of the Hillsborough and Murchison meteorites measured by GC-MS.

	Hillsborough (CM1/2)		Murchison (CM2)	
	Free (nmol g^{-1})	Total (nmol g^{-1})	Free (nmol g^{-1})	Total (nmol g^{-1})
Acidic amino acids				
D-Aspartic acid	0.02 ± 0.01	3.71 ± 3.23	0.99 ± 0.35	1.84 ± 0.72
L-Aspartic acid	0.03 ± 0.00	11.52 ± 10.07	5.07 ± 1.84	6.71 ± 2.95
D-Glutamic acid	n.f.	6.54 ± 2.85	0.50 ± 0.20	3.07 ± 1.10
L-Glutamic acid	n.f.	38.63 ± 14.42	1.92 ± 0.72	17.31 ± 4.39
Hydroxy amino acids				
D-Serine	n.f.	n.f.	1.60 ± 1.08	0.88 ± 0.41
L-Serine	n.f.	n.f.	2.18 ± 1.69	n.f.
C2 amino acid				
Glycine	3.28 ± 0.85	101.03 ± 34.42	24.40 ± 3.90	20.23 ± 10.94
C3 amino acids				
β-Alanine	0.90 ± 0.21	34.34 ± 13.06	7.89 ± 1.90	9.42 ± 4.67
D-Alanine	1.55 ± 0.35	62.93 ± 26.20	10.89 ± 2.38	15.47 ± 9.05
L-Alanine	1.42 ± 0.35	68.46 ± 24.43	11.30 ± 1.59	16.97 ± 11.47
C4 amino acids				
D,L- α -Amino-*n*-butyric acid	0.06 ± 0.01	23.34 ± 7.77	2.74 ± 0.71	5.38 ± 2.57
D-β-Amino-*n*-butyric acid	0.10 ± 0.06	7.17 ± 3.29	1.03 ± 0.57	1.10 ± 0.71
L-β-Amino-*n*-butyric acid	0.09 ± 0.10	8.58 ± 3.95	0.85 ± 0.51	1.65 ± 0.89
γ-Amino-*n*-butyric acid	0.03 ± 0.04	26.05 ± 10.89	3.29 ± 1.14	11.28 ± 4.77
α-Aminoisobutyric acid	3.25 ± 0.58	78.62 ± 31.71	38.83 ± 6.86	18.39 ± 11.83
C5 amino acids				
D-Valine	n.f.	9.66 ± 4.63	0.36 ± 0.35	1.72 ± 1.05
L-Valine	n.f.	61.69 ± 22.33	5.63 ± 0.60	15.68 ± 9.55
D,L-Isovaline	4.25 ± 0.74	82.70 ± 40.24	51.87 ± 8.15	19.77 ± 12.89
C6 amino acid				
ε-Amino-*n*-caproic acid	n.f.	207.96 ± 100.04	31.61 ± 8.58	141.77 ± 37.32
Sum C2-C6 amino acids	**14.98**	**624.97**	**171.34**	**166.87**

Table S-15. The D/L ratios and corresponding L−enantiomeric excesses (% Lee = % L − % D) of amino acids measured in the Hillsborough and Murchison hot−water extracts. The errors shown were calculated by standard error propagation of the uncertainties given for the individual amino acid abundances.

	Hillsborough (CM1/2)				Murchison (CM2)			
	Free		Total		Free		Total	
Amino Acid	**D/L**	**Lee (%)**	**D/L**	**Lee (%)**	**D/L**	**Lee (%)**	**D/L**	**Lee (%)**
Aspartic Acid	0.71 ± 0.31	17.2 ± 15.2	0.32 ± 1.23	51.3 ± 45.5	0.19 ± 0.51	67.4 ± 13.8	0.28 ± 0.59	56.9 ± 19.8
Glutamic Acid	n.r.	n.r.	0.17 ± 0.57	71.0 ± 14.2	0.26 ± 0.55	58.8 ± 18.1	0.18 ± 0.44	69.9 ± 11.2
Serine	n.r.	n.r.	n.r.	n.r.	n.r.	15.2 ± 50.2	n.r.	n.r.
Alanine	1.09 ± 0.34	-4.1 ± 16.8	0.92 ± 0.55	4.2 ± 27.4	0.96 ± 0.26	1.8 ± 13.0	0.91 ± 0.89	4.6 ± 44.6
Valine	n.r.	n.r.	0.08 ± 0.33	72.9 ± 14.1	0.06 ± 0.33	87.9 ± 3.7	0.11 ± 0.86	80.3 ± 15.3

Isovaline	0.96 ± 0.25	2.2 ± 12.3	1.02 ± 0.69	-0.9 ± 34.4	0.86 ± 0.22	7.3 ± 11.1	1.02 ± 0.92	-1.2 ± 46.1

Helium was used as carrier gas and the column flow rate was set at 1.1 mL/min and injection (1 μL) was in split mode (10:1) at 220 °C. The source and quadrupole temperatures were maintained at 230 °C and 150 °C respectively, the MSD transfer line was heated to 180 °C. Standard autotunes with perfluorotributylamine (PFTBA) and air/water checks were made on a daily basis. The oven program was set at an initial temperature of 90 °C and held for 2 minutes, then increased by 5 °C/min to 200 °C and held for 6 min. GC-MS methods and oven program were the same for both instruments used. Total ion current chromatograms were acquired and analyzed with Agilent Technologies MSD ChemStation (6890-5973) or MassHunter (7890-5975) software. Amino acids present in the meteorite samples were identified by comparison of the retention time and mass fragmentation pattern with a known amino acid standard mixture, and quantification was made by chromatographic data collected in the selected ion monitoring (SIM) mode. Identification was added by retention time locking of GC method and creation of a custom library from standards which include retention time and retention indices for the amino acids.

Doppler weather radar reflections from falling meteorites
By: Marc D. Fries

Methods: The Hillsborough meteorite fall was recorded by weather radars in the National Oceanic and Atmospheric Administration (NOAA)'s NEXRAD network, as well as Terminal Doppler Weather Radar (TDWR) radars operated by the Federal Aviation Administration (FAA). NEXRAD utilizes WSR-88D radars operating in the S band (10.6 cm wavelength) while TDWR radars operate in the C band (5.3 cm wavelength).

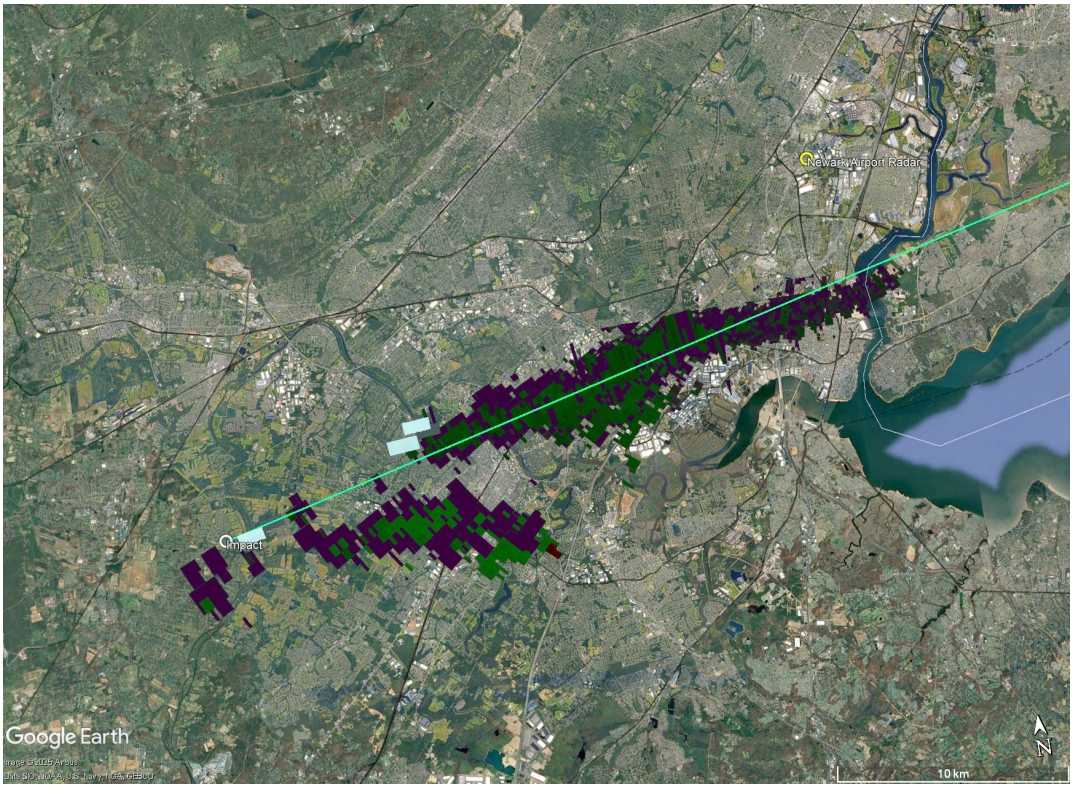

Fig. S-27. Combined ground-projected radar reflections from the Hillsborough meteorite fall. In light blue are the three NEXRAD-detected reflections, in dark colors those generated by the nearby TEWR (Newark Airport TDWR) radar, the location of which is identified at upper right. The green line is the ground-projected path of the fireball. The first radar signature to appear was that at far left and additional signatures appeared drifting ENE over a period of 14 minutes 58 seconds afterward, when smaller meteorites fell to lower altitudes under the influence of prevailing winds.

Results: Falling material was first detected by the TEWR radar in the TDWR network which serves the Newark Liberty National Airport. The TEWR radar lies only 5-40 km laterally from the fall as measured from the nearest and farthest radar signatures (Fig. S-27). The first radar detection occurred at 15:18:52.0 UTC and an altitude of 13.339 km above mean sea level (AMSL). This is 84 s after the fireball terminus. TEWR recorded falling meteorites in an impressive 25 radar sweeps, with the last

one recorded at 15:33:50.0 UTC and 6.4 km AMSL. The total elapsed time of detection is 14 minutes 58 seconds.

NEXRAD detections were sparse, with only a trio of pixels appearing in data from the KDIX (Fort Dix, NJ) radar (Fig. S-27). One is close to the fall location.

According to the Jörmungandr dark flight model (*83*) and using radiosonde (or "weather balloon") data from Upton, NY collected at 1200 UTC on 16 July 2024, the last material detected on radar is approximately 0.5 mm in diameter (~0.1 g) assuming spheres with density of 1.89 g/cc. The first material seen corresponds to meteorites of approximately 10 g in mass.

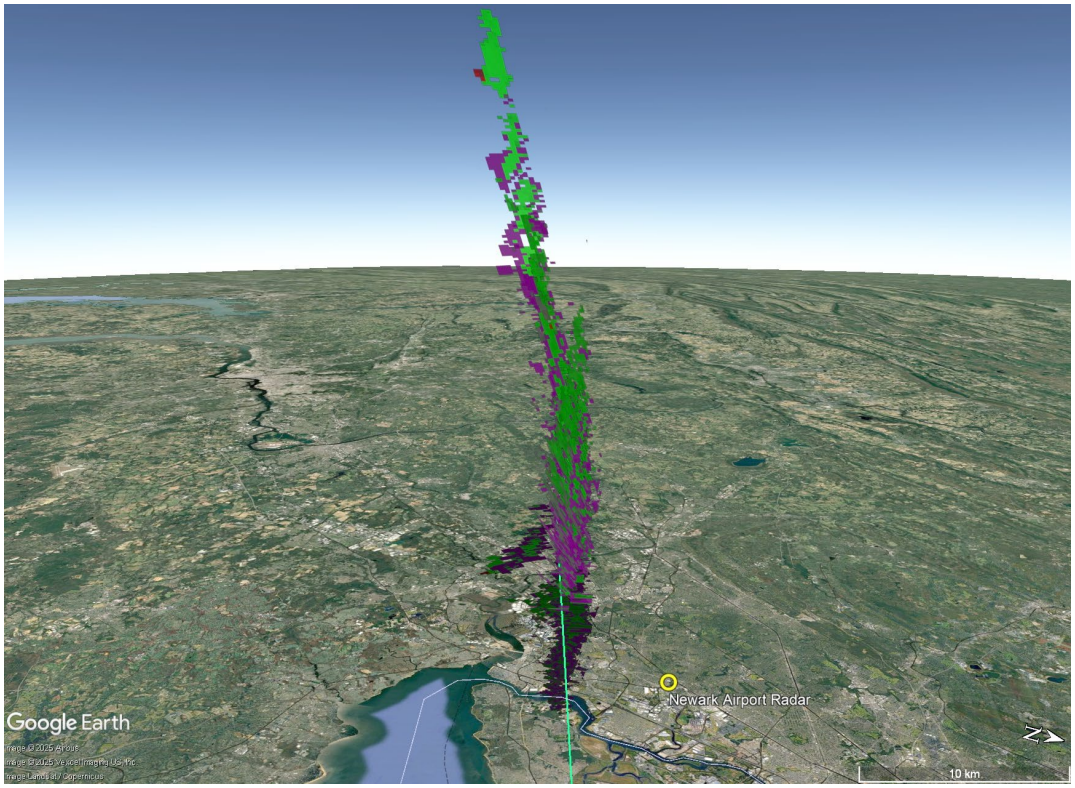

Fig. S-28. The same data as that in Fig. S-27 but viewed from an approximate 45 degree elevation along the direction of flight of the bolide. The highest altitude of a radar signature measures 13,339 m above mean sea level (AMSL) at the signature centroid and the lowest occurs at 6,470 m ASML.